Design and Investigation of High Speed and High Power InGaAs/InP One-Sided Junction Photodiodes

Jie Xu

A Thesis
In the Department
of
Electrical and Computer Engineering

Presented in Partial Fulfillment of the Requirements

For the Degree of

Doctor of Philosophy (Electrical and Computer Engineering) at

Concordia University

Montréal, Québec, Canada

May 2020

CONCORDIA UNIVERSITY

School of Graduate Studies

This is to certify that the thesis prepared

By: Jie Xu

Entitled: Design and investigation of high speed and high power InGaAs/InP one-sided junction photodiodes

and submitted in partial fulfillment of the requirements for the degree of

Doctor of Philosophy (Electrical and Computer Engineering)

complies with the regulations of the University and meets the accepted standards with respect to originality and quality.

Signed by the final examining committee:

_____ Chair
Dr. Muthukumaran Packirisamy

_____ External Examiner
Dr. Martin Rochette

_____ External to Program
Dr. Pablo Bianucci

_____ Examiner
Dr. Abdel R. Sebak

_____ Examiner
Dr. Glenn Cowan

_____ Supervisor
Dr. John Xiupu Zhang

_____ Supervisor
Dr. Ahmed A. Kishk

Approved by: _____

Dr. Wei-Ping Zhu, Graduate Program Director

July 22, 2020   _____

Dr. Mourad Debbabi, Dean, Faculty of Engineering and Computer Science

ABSTRACT

Design and Investigation of High Speed and High Power InGaAs/InP One-Sided Junction Photodiodes

Jie Xu, Ph.D.
Concordia University, 2020

Photodiodes convert optical signals into electrical signals and are widely used in optical fiber communication systems, photonics generation of millimeter-wave (MMW) and terahertz (THz) wave signals, radio-over-fiber wireless communication systems, etc. In these applications, photodiodes play a key role. Nowadays, the well known uni-travelling carrier photodiodes (UTC-PDs) have been widely used in the aforementioned applications since its first invention in 1997. Over the past two decades, the performance of UTC-PD and its derivatives has been improved continuously. However, the epitaxial layer structures become more and more complex.

To simplify the structure and improve the performance of photodiodes, a high-speed one-sided junction photodiode (OSJ-PD) with low junction capacitance is proposed for the first time. The OSJ-PD is proposed based on the structure of the InGaAs Shottky barrier photodiode (SB-PD) and UTC-PD. It has been demonstrated that the OSJ-PD has the characteristics of the simple epitaxial layer structure, high speed, high output power, and low junction capacitance. The OSJ-PD with 300 nm absorption layer thickness has achieved a bandwidth of 64 GHz (without considering the external circuit) and a photocurrent density of 2.4×10^5 A/cm^2 under a 10 V bias voltage.

A modified InGaAs/InP one-sided junction photodiode (MOSJ-PD) is further presented for the first time. The MOSJ-PD is proposed from OSJ-PD by inserting a cliff

layer into the absorption layer. Compared with the modified uni-travelling carrier photodiode (MUTC-PD), the MOSJ-PD has the advantages of simpler epitaxial layer structure and lower junction capacitance. In MOSJ-PD, the space charge effect at high light intensity is further suppressed. Thus, both 3-dB bandwidth and output current are improved simultaneously.

Based on the newly proposed OSJ-PD structure, an evanescently coupled one-sided junction waveguide photodiode (EC-OSJ-WGPD) is proposed and investigated numerically. The EC-OSJ-WGPD has a simple structure, while the characteristics of high speed and high output power are maintained. The designed EC-OSJ-WGPD with an absorption layer thickness of 350 nm achieves a bandwidth of 44.5 GHz (without considering the external circuit) and a responsivity of 0.98 A/W.

A unique equivalent circuit model (Circuit Model B), which combines the Technology Computer-Aided Design (TCAD) and microwave circuit simulation, is adopted to analyze the frequency response of InGaAs/InP photodiode. This methodology demonstrates high accuracy in the frequency response analysis. The OSJ-PD and MOSJ-PD with a diameter of 5 μm achieve bandwidths of 119 and 120 GHz, which are 5.3% and 6.2% higher than the well known MUTC-PD. The EC-OSJ-WGPD achieves a bandwidth of 65.5 GHz.

ACKNOWLEDGMENTS

First of all, I sincerely appreciate Prof. Ahmed Kishk for his guidance, support, advice, and encouragement during my PhD study. I cannot finish my PhD study without his help.

Secondly, I sincerely appreciate Prof. Xiupu Zhang for giving me a chance to study photonics. I also thank him for his support and help for my PhD study.

Thirdly, I thank Prof. Sebak, Prof. Cowan, Prof. Bianucci, and Prof. Rochette, for their efforts in reviewing my thesis and making invaluable suggestions to improve my thesis. I also thank Prof. Kabir for teaching me the course "Solid State Devices."

Finally, I would like to thank all competent staff and faculty in our department. They are the foundation of a just and prosperous society.

Table of Contents

List of Figures

List of Tables

List of Abbreviations

AlN	Aluminium nitride
APD	Avalanche photodiode
CPW	Coplanar waveguide
EC-OSJ-WGPD	Evanescently coupled one-sided junction waveguide photodiode
EDFA	Erbium-Doped Fiber Amplifier
EHPs	Electron and hole pairs
InGaAs	Indium Gallium Arsnide
InP	Indium Phosphide
MBE	Molecular beam epitaxy
MMW	Millimeter-wave
MOCVD	Metal-organic Chemical Vapor Deposition
MoF	Millimeter wave-over-fibre
MOSJ-PD	Modified one-sided junction photodiode
MSM-PD	Metal-semiconductor-metal photodiode
MUTC-PD	Modified uni-traveling carrier photodiode
NBUTC-PD	Near-ballistic uni-traveling carrier photodiode
OSJ-PD	One-sided junction photodiode
PIC	Photonic integrated circuit
PIN-PD	PIN photodiode
RC	Resistance-capacitance
SB-PD	Schottky barrier photodiode

TCAD	Technology Computer-Aided Design
THz	Terahertz
TTR-PD	Triple transition region photodiode
UTC-PD	Uni-travelling carrier photodiode

List of Symbols

α	Photon absorption coefficient
Δ_0	Split-off valence bandgap at 300 K
ε	Permittivity
ε_0	Permittivity of free space
ε_r	Relative permittivity
ε_{req}	Equivalent relative permittivity
ε_∞	High-frequency permittivity
η	Quantum efficiency
Ψ	Electrostatic potential
μ_n	Electron mobility
μ_p	Hole mobility
ν	Frequency
ρ	Space charge density
τ_{RC}	Resistance-capacitance charging time
τ_{tr}	Carrier transit time
f_{3dB}	3-dB bandwidth
h	Planck's constant
k	Wavenumber
q	Elementary charge
C_j	Junction capacitance
C_p	Parasitic capacitance

D_n	Electron diffusion coefficient
D_p	Hole diffusion coefficient
E	Energy (eV)
E/O	Electrical-to-optical
G_n	Electron generation rate
G_p	Hole generation rate
I_d	Dark current
I_{ph}	Photo-induced current
J_d	Diffusion current
J_{dr}	Drift current
$\vec{J}_n$	Electron current density
$\vec{J}_p$	Hole current density
O/E	Optical-to-electrical
P_{inc}	Incident optical power
R	Responsivity
R_l	Load resistance
R_n	Electron recombination rate
R_p	Hole recombination rate
R_s	Series resistance

Chapter 1 Introduction

1.1 Introduction

High-speed and high-power photodiodes are critical components for optical fiber communication systems [1], photonics generation of millimeter-wave (MMW) and terahertz (THz) wave [2-7], and radio-over-fiber wireless communication systems [7-11]. The specific applications include analog photonics links [12], photodiode emitters (photodiodes integrated with antennas) [13-17], high speed measurements [18], THz spectroscopy [3,5], wireless communications [8,9,19], and imaging [20].

The function of photodiodes is to convert an optical signal (digital or analog) into an electrical signal (photocurrent). Thanks to the development of Erbium-Doped Fiber Amplifier (EDFA), the optical amplifier can achieve a high gain of over 30 dB with a large bandwidth of over 1 THz. Optical to electrical converter must be capable of generating broadband and high power electrical signals to improve the overall system performance. Photodiodes absorb incident photons and generate electron and hole pairs (EHPs). Photogenerated EHPs are separated by the internal electric field and then collected by the external circuit. Photodiodes with high output power can eliminate the need for bulky and expensive electrical post-amplifiers [21].

In the absence of incident light, photodiodes still have an output current I_d (dark current). The photo-induced current (I_{ph}) is usually determined by the incident optical power (P_{inc}) and can be expressed as $I_{ph}=R{\cdot}P_{inc}$, where R is the responsivity (unit: A/W).

1.2 Applications of the high speed and high power photodiodes
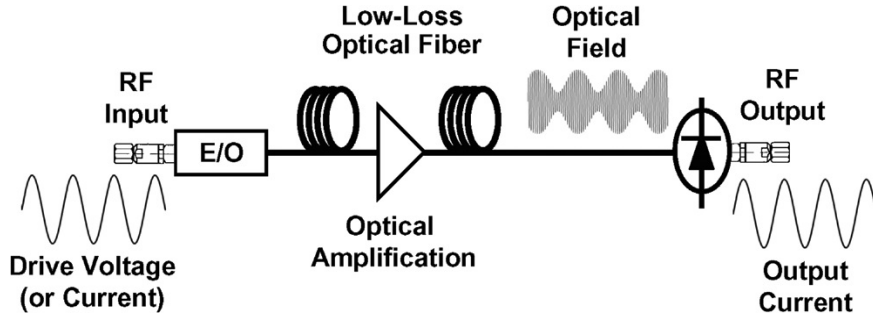
Figure 1-1 Schematic diagram of a long-haul analog photonic system [12].
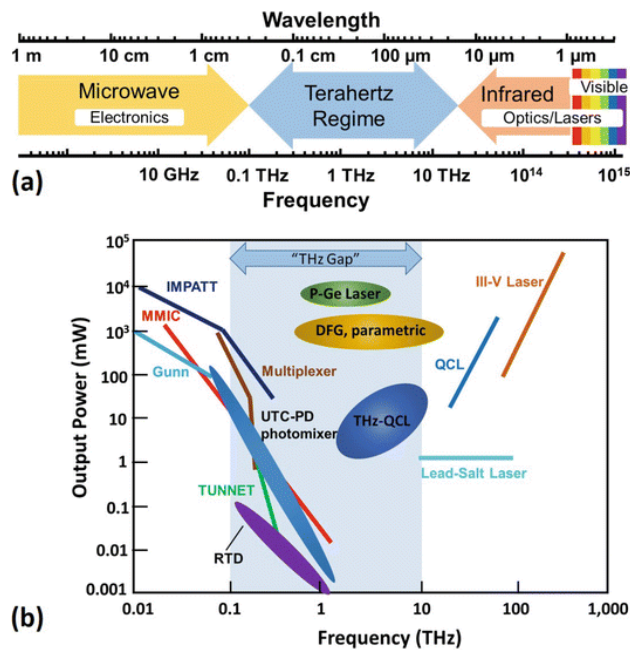
Figure 1-2 (a) Frequency range of THz region and (b) various THz signal sources [4].

The applications of high speed and high power photodiodes are so broad that we cannot introduce all of them here. The typical applications in optical fiber communication, THz signal generation, and wireless communication are briefly introduced. The block diagram of a long-haul analog photonic system [12] is shown in Figure 1-1. An analog electrical signal is modulated onto an optical carrier in the electrical-to-optical (E/O) converter and transmitted in an optical fiber that may include optical amplification. The

optical fiber has advantages, including low-loss transmission with typically 0.2 dB/km attenuation and lightweight. Recovery of the transmitted optical signal employs a photodiode, which should have broad bandwidth and high output power.
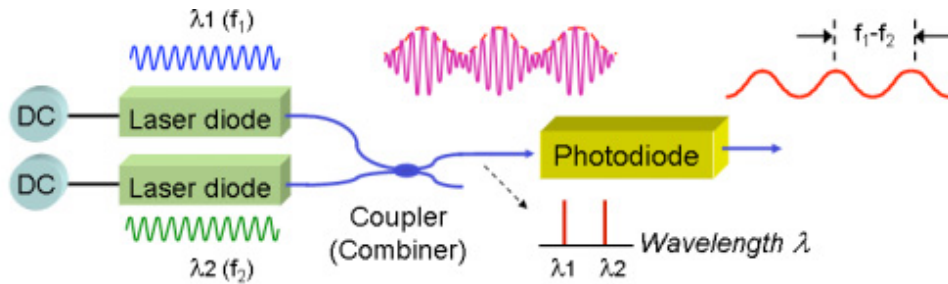
Figure 1-3 Block diagram of the MMW/THz-wave generator using optical heterodyne technique [10].
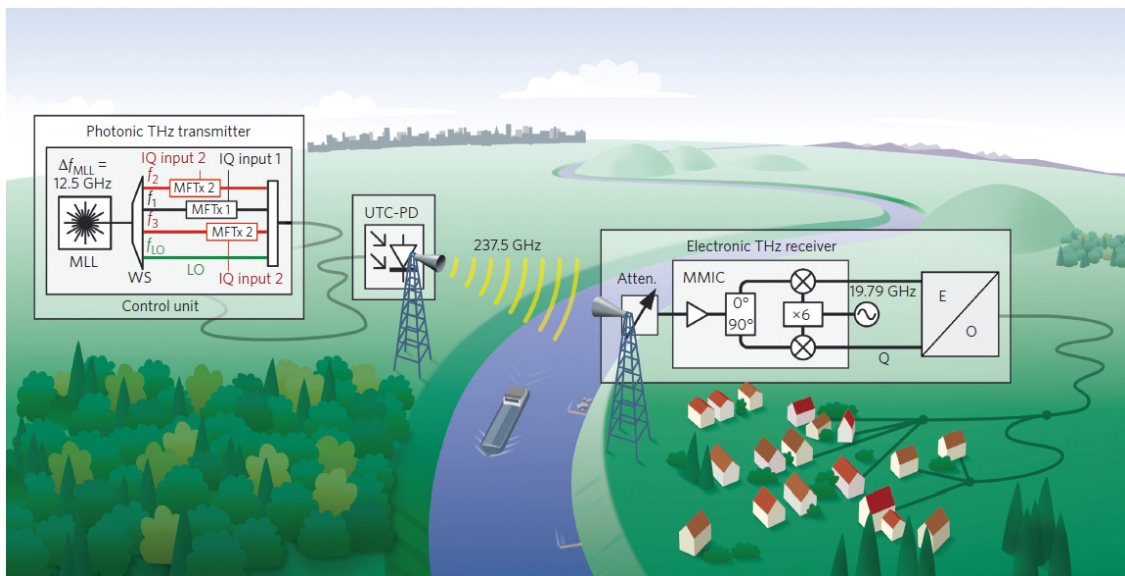
Figure 1-4 Prospective application scenario for a long-range, high-capacity wireless communication link at terahertz frequencies [9].

Figure 1-2 shows the frequency range of the THz regime and summarizes various approaches for THz signal generation. The THz regime is referred to as the frequency gap between microwave and infrared light, which is typically between 100 GHz and 30 THz [4]. The THz electromagnetic spectrum is less utilized mainly because of the lack of signal

source and detector [21]. As shown in Figure 1-3, uni-travelling carrier photodiode (UTC-PD) employs heterodyne of two optical signals with different wavelengths to generate THz signal. And UTC-PD is an excellent candidate for THz signal source. The output powers of UTC-PD at 100 GHz and 1 THz are around 20 mW and 10 μW [4].

Due to the high carrier frequency of the THz wave signal, it can provide a high data rate for wireless communication systems. A single input and single output wireless communication system operating at 237.5 GHz is shown in Figure 1-4. The UTC-PD output is radiated over a beam-focusing antenna. The experimental results show a data rate of 100 Gbit/s over a distance of 20 m. It's expected to pave the road for wireless communication systems with a data rate of Tbit/s over a distance of ≥1 km [9].

1.3 Motivation

In the aforementioned applications and systems, high speed (bandwidth) and high output power (photocurrent) are two essential requirements for the photodiodes. Nowadays, the UTC-PD and its variants have become the workhorses in the aforementioned systems, and exhibit very high bandwidth and high output power. Aimed at further improving the performance and providing attractive alternative photodiode structures, this Thesis proposes and investigates two fundamental photodiode structures, namely, the InGaAs/InP one-sided junction photodiode and the modified InGaAs/InP one-sided junction photodiode.

Moreover, aimed at providing a reliable and accurate analysis methodology, the frequency response of a photodiode is analyzed from the perspective of the microwave circuit. Compared to the conventional analysis methodology, which only considers the

influence of the carrier transit time and resistance-capacitance (RC) charging time, this unique methodology also includes the influence of the external microwave circuit. It has been demonstrated that the external microwave circuit has a significant influence on the photodiode's frequency response. Thus, not only the photodiode itself but also the external microwave circuit should be considered during the design and fabrication of the photodiode.

1.4 Thesis overview

This chapter briefly introduces the basics and applications of the high speed, high power photodiodes, and the structure of the thesis.

In chapter 2, the basic principles of InGaAs/InP photodiodes are presented.

In chapter 3, the underlying basic knowledge (equations and physical models) of the physics-based device simulation software (Silvaco Atlas) is briefly discussed. The material properties of InGaAs, InP, and InGaAsP are given. Also, the optoelectronic simulator (Luminous) is introduced.

In chapter 4, a high-speed InGaAs/InP one-sided junction photodiode (OSJ-PD) with low junction capacitance is designed and analyzed for the first time. The newly designed OSJ-PD has a simple structure while maintaining the characteristics of high speed and high power.

In chapter 5, a modified InGaAs/InP one-sided junction photodiode (MOSJ-PD) is presented for the first time. The MOSJ-PD is proposed from the OSJ-PD by inserting a cliff layer into the absorption layer. In MOSJ-PD, the space charge effect at high light

intensity can be suppressed. Thus, both 3-dB bandwidth and output current can be improved simultaneously.

In chapter 6, an evanescently coupled one-sided junction waveguide photodiode (EC-OSJ-WGPD) is proposed and investigated numerically. Comprehensive analyses of the EC-OSJ-WGPD, including photogeneration rate, internal optical power distribution, energy band diagram, internal electric field, photocurrent, and 3-dB bandwidth, are presented.

In chapter 7, the equivalent circuit model of InGaAs/InP photodiodes is investigated. The equivalent circuit model, which includes the tuning effect of the external circuit, demonstrates high accuracy in the frequency response analysis of InGaAs/InP photodiodes. The frequency responses of OSJ-PD, MOSJ-PD, and EC-OSJ-WGPD are analyzed using the equivalent circuit model (Circuit Model B).

In chapter 8, a summary and future work are discussed.

Chapter 2 Fundamentals of InGaAs/InP Photodiodes

This chapter briefly introduces the basic principles of the semiconductor photodetectors, with emphasis on the InGaAs/InP materials-based photodiodes. The basic knowledge introduced in this chapter can facilitate the understanding of the following chapters in the design and analysis of the InGaAs/InP photodiodes.

2.1 Types of semiconductor photodetectors

Many semiconductor-based photodetector structures have been demonstrated, and they can be classified into the following categories [22]:
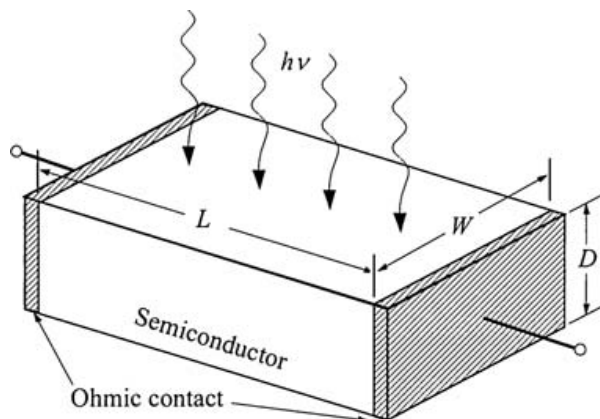
Figure 2-1 Schematic diagram of a photoconductor [23].

■ Bulk: photoconductors (photoresistors);

■ PN junction based: PN photodiodes, PIN photodiodes (PIN-PDs), UTC-PDs, OSJ-PDs, avalanche photodiodes (APDs), phototransistors;

■ Metal-semiconductor junction based: Schottky barrier photodiodes, metal-semiconductor-metal photodiodes (MSM-PDs).

The photoconductor structure is shown in Figure 2-1, light is absorbed by the bulk semiconductor material, and a large number of EHPs are generated. With the increase of EHPs, electrical conductivity also increases. Photoconductors are simple, low-speed devices, and are not suitable for high-speed telecommunication applications [22].
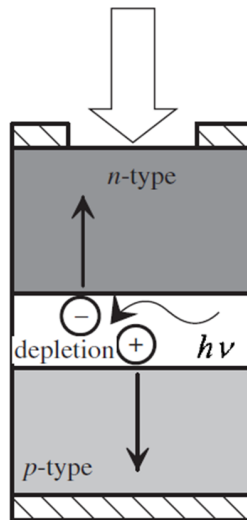
Figure 2-2 Schematic diagram of a PN junction photodiode [22].
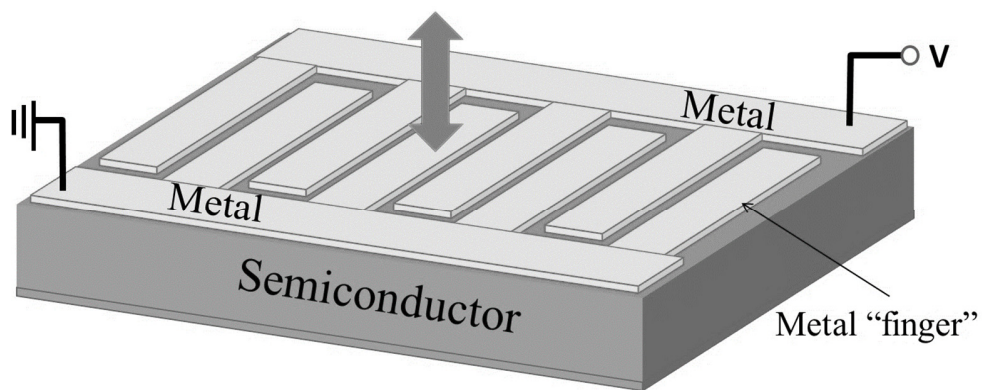
Figure 2-3 Schematic diagram of an MSM photodetector [24].

In PN junction based photodiodes, photogenerated EHPs are separated by an internal electric field. PN photodiode is the simplest photodetector structure and is shown in Figure 2-2. Photons are absorbed in the depletion region, n-type region, and a p-type region. Since

the depletion region is narrow, and the carrier diffusive process is slow, the frequency response is poor and is limited by the carrier transit time [22].

As shown in Figure 2-3, the MSM-PDs utilize interdigitated electrodes on top of a light absorption material, which forms back-to-back Schottky barrier diodes. The MSM-PDs have a much lower capacitance per unit area than PIN-PDs, and the bandwidth is often carrier transit time-limited [24]. The carrier transit time is determined by the spacing between interdigitated electrodes. The MSM-PDs have the characteristics of high speed and ease of integration. But MSM-PDs suffer from low quantum efficiency because part of the incident light will be reflected back by the electrodes. This drawback limits its application.

2.2 Photodetector materials
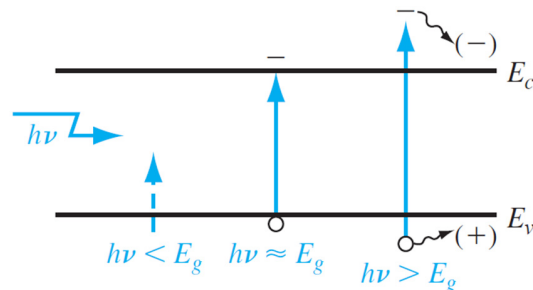
Figure 2-4 Photon absorption in a semiconductor [25].

When light is injected into a semiconductor material, the light may be absorbed or pass through the semiconductor, depending on the photon energy and the semiconductor bandgap energy E_g. (Note: light can also be absorbed by impurities or scattered inside the semiconductor; these behaviors are not considered in this thesis for simplicity.) As shown in Figure 2-4, if the photon energy $E = h\nu \geq E_g$, photons will be absorbed, and EHPs will be generated. The semiconductor's absorption coefficient α is a function of photon energy $h\nu$

and material's bandgap energy E_g. The absorption coefficient as a function of wavelength for several semiconductors is given in Figure 2-5.
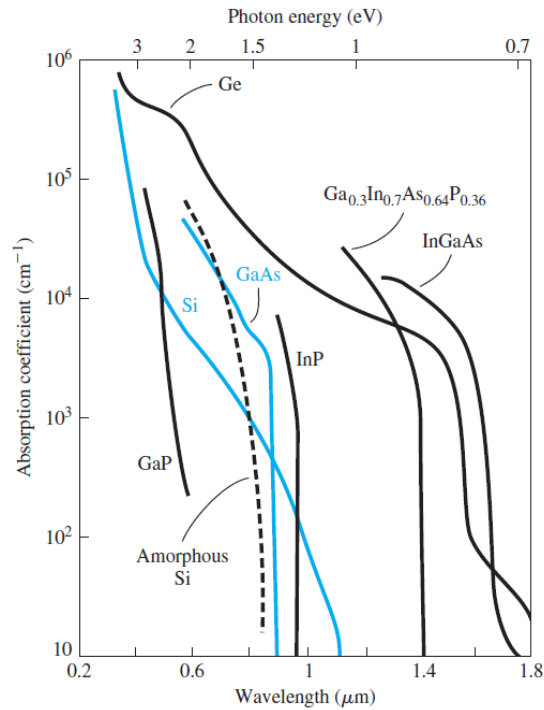
Figure 2-5 Absorption coefficient versus wavelength of several semiconductors [25].

Many semiconductor materials are adopted for different applications. Silicon (Si) is a commonly used photodetector material for the light wavelength from 0.4 to 1.0 μm. Germanium (Ge) is used for a longer wavelength of up to 1.8 μm. For high speed and high power photodetectors, III-V materials are more important. $In_{0.53}Ga_{0.47}As$ has a cutoff wavelength of 1.65 μm and is widely used for optical communications at 1.3 and 1.55 μm. GaAs has a cutoff wavelength of 0.9 μm and is used for visible and near-infrared light photodetector [26].

The energy E versus wavenumber k diagrams of GaAs and Si are given in Figure 2-6. For GaAs, both the maximum valence band energy and the minimum conduction band energy occur at the same k value. A semiconductor with this property is called a direct

bandgap semiconductor. For direct bandgap semiconductor materials, the transition between the conduction band and valence band does not involve the change in crystal momentum. For silicon, the maximum valence band energy and the minimum conduction band energy do not occur at the same k value. A semiconductor with this property is called an indirect bandgap semiconductor. The transition in indirect bandgap material involves the change in crystal momentum. Silicon and germanium are indirect bandgap materials, while InGaAs and GaAs are direct bandgap materials. Direct bandgap materials typically have a higher absorption coefficient than indirect bandgap materials.
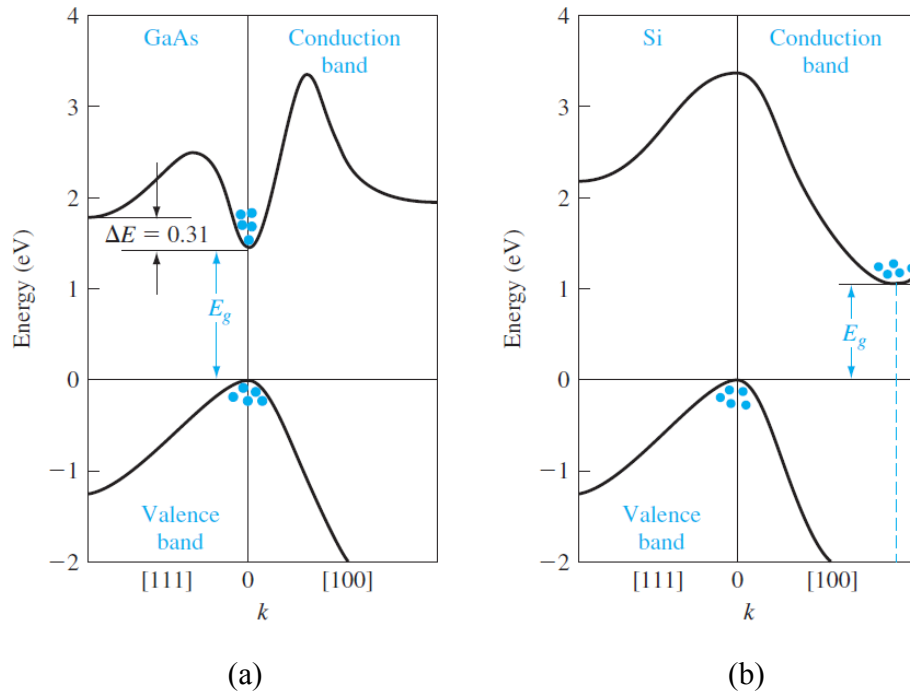
Figure 2-6 Energy-band structures of (a) GaAs and (b) Si [25].

In this thesis, we mainly study the PN junction based photodiodes, including PIN-PD, UTC-PD, and OSJ-PD. And the semiconductor materials used for these photodiodes are InGaAs, InGaAsP, and InP.

2.3 Photodiode structures

In the design of photodiodes, speed, power, and responsivity are three major performance characteristics, which should be considered carefully. In the early stage, surface illuminated PIN-PD is widely used in optical communication systems [27-32]. However, with the increasing demand for the optical communication data rate, PIN-PD cannot satisfy the requirements anymore. Various photodiode structures have been developed to boost the optical communication system performance.

2.3.1 Geometric structure
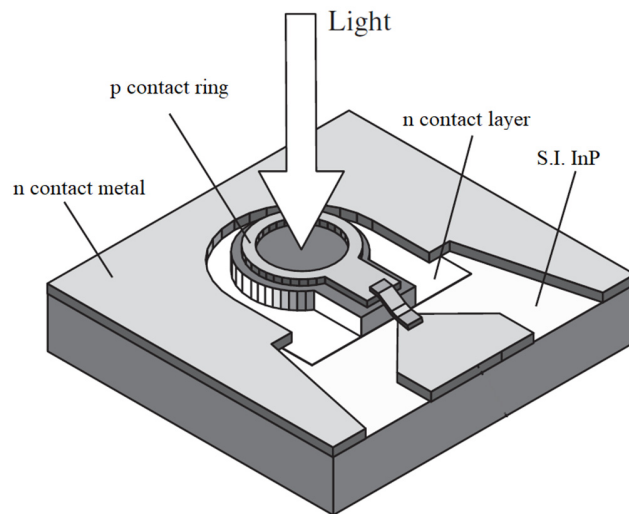
Figure 2-7 Schematic structure of a surface illuminated photodiode.

Researchers have made lots of efforts to improve the photodiodes' performance, and several photodiode structures have been developed, such as surface illuminated photodiodes, waveguide photodiodes, travelling wave photodiodes [22], etc. This thesis mainly focuses on the study of surface illuminated and waveguide photodiodes, and their schematic structures are given in Figures 2-7 and 2-8.
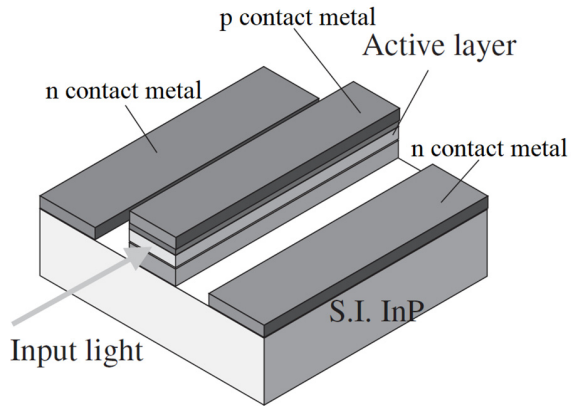
Figure 2-8 Schematic structure of a waveguide photodiode.

2.3.2 Epitaxial layer structure
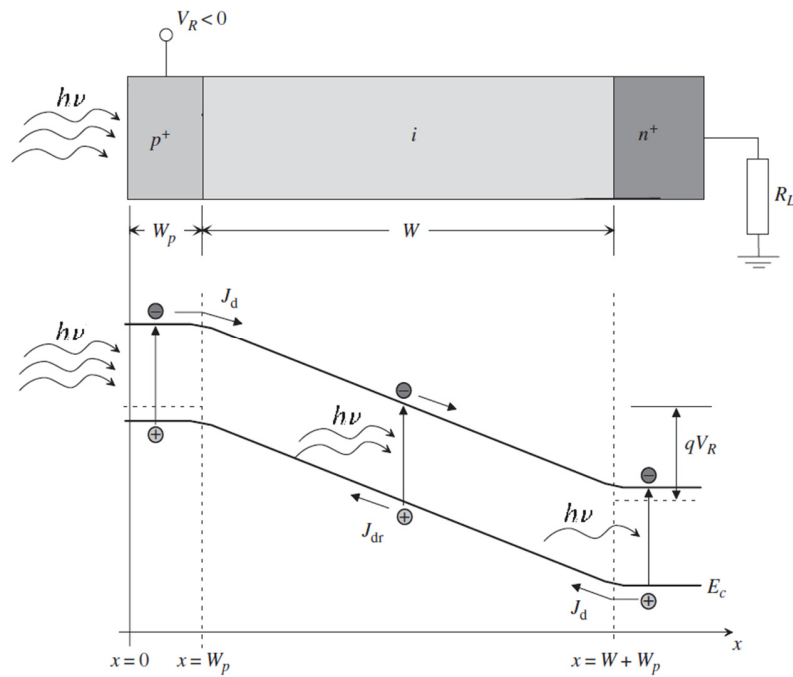
Figure 2-9 Schematic structure (above) and energy band diagram (below) of a PIN photodiode with a reverse bias voltage of V_R. (J_d is diffusion current, and J_{dr} is the drift current.)

The epitaxial layer structure of a photodiode has a significant influence on the performance. In the early days, PIN-PD has been widely used for optical communication

systems. It achieves a bandwidth of over 100 GHz [28,32]. The schematic structure and energy band diagram of a PIN-PD are given in Figure 2-9. EHPs are generated in the depletion region and then separated by the internal electric field. Since holes are slow-moving carriers, the performance of a PIN-PD, such as 3-dB bandwidth and saturation photocurrent, is mainly limited by holes.
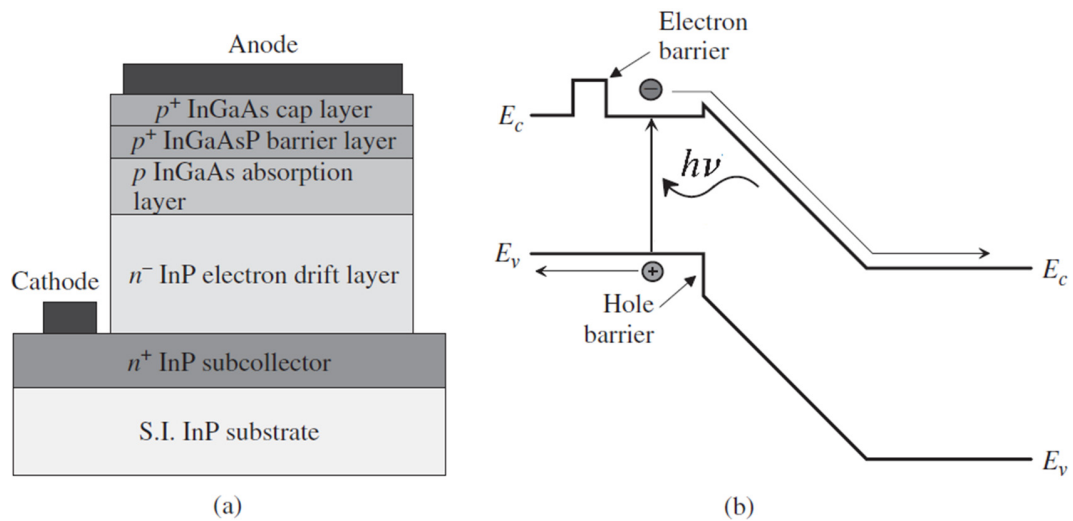
Figure 2-10 The epitaxial layer structure (a) and energy band diagram (b) of a UTC-PD.

To overcome the drawback of the PIN-PD, UTC-PD was proposed in 1997 [33]. The epitaxial layer structure and energy band diagram of a UTC-PD is given in Figure 2-10. EHPs are generated in the p InGaAs absorption layer, and then electrons will diffuse towards the collector layer and drift to the n contact layer. The 3-dB bandwidth and saturation photocurrent can be improved in UTC-PD since electrons are the only active carriers in UTC-PD.

2.4 Photodiode characteristic parameters

2.4.1 Quantum efficiency and responsivity

The quantum efficiency η of a photodiode indicates the photodiode's ability to convert optical energy into electrical energy, which is defined as:

$$\eta = \frac{number\ of\ electron\ and\ hole\ pairs\ contributing\ to\ the\ photo-induced\ current}{number\ of\ incident\ photons} \quad (2.1)$$

$$\eta = \frac{I_{ph}\ /\ q}{P_{inc}\ /\ h\nu} \times 100\ \% \quad (2.2)$$

where I_{ph} is the photo-induced current, P_{inc} is the incident optical power, q is the elementary charge, h is the Planck's constant, and ν is the frequency.

Instead of the quantum efficiency η, the responsivity R (A/W) is often used.

$$R = \frac{I_{ph}}{P_{inc}} = \frac{q\eta}{h\nu} \quad (2.3)$$

2.4.2 Frequency response

The response speed of a photodiode is usually limited by the carrier transit time τ_{tr} and RC charging time τ_{RC}. In the depleted region of a photodiode, electrons and holes travel at saturation velocity. In the undepleted region, the transportation of electrons and holes is the diffusion process. The diffusion process is usually slower than the drift process.

2.4.3 Linearity

For an ideal photodiode, the output photocurrent I_{ph} is linear with the incident optical power P_{inc}. A photodiode is linear if the responsivity R is constant. However, in reality, a

photodiode is linear only within a range of the incident optical power. The minimum incident optical power is determined by the minimum detectable optical power. The maximum incident optical power is determined by the maximum optical power with which the photodiode can handle before saturation occurs.

2.4.4 Maximum reverse bias voltage

The maximum reverse bias voltage is the voltage above which photodiode breakdown occurs. Any photodiode should be biased below this voltage.

2.5 Photodiode speed and power limitations

$$f_{3dB} = \frac{1}{2\pi\sqrt{\tau_{tr}^2 + \tau_{RC}^2}}$$

(2.4)

Generally speaking, the speed of a photodiode is mainly determined by the carrier transit time τ_{tr} and RC charging time τ_{RC}. The 3-dB bandwidth f_{3dB} can be approximately expressed as Equation (2.4). In order to increase the bandwidth, both τ_{tr} and τ_{RC} should be decreased. As shown in Figures 2-11(a) and 2-12(a), the carrier transit time in UTC-PD is mainly limited by electrons, while the carrier transit time in PIN-PD is mainly limited by slow-moving holes. To reduce holes transit time in PIN-PD, the thickness of the absorption layer should be reduced. To reduce electrons transit time in UTC-PD, the thickness of the absorption layer and the collector layer should be reduced. However, the reduction of absorption layer thickness and collector layer thickness in UTC-PD lowers the responsivity and increases the junction capacitance. The reduction of absorption layer thickness in PIN-PD lowers the responsivity and increases the junction

capacitance also. Thus, compromise should be made between carrier transit time and junction capacitance.
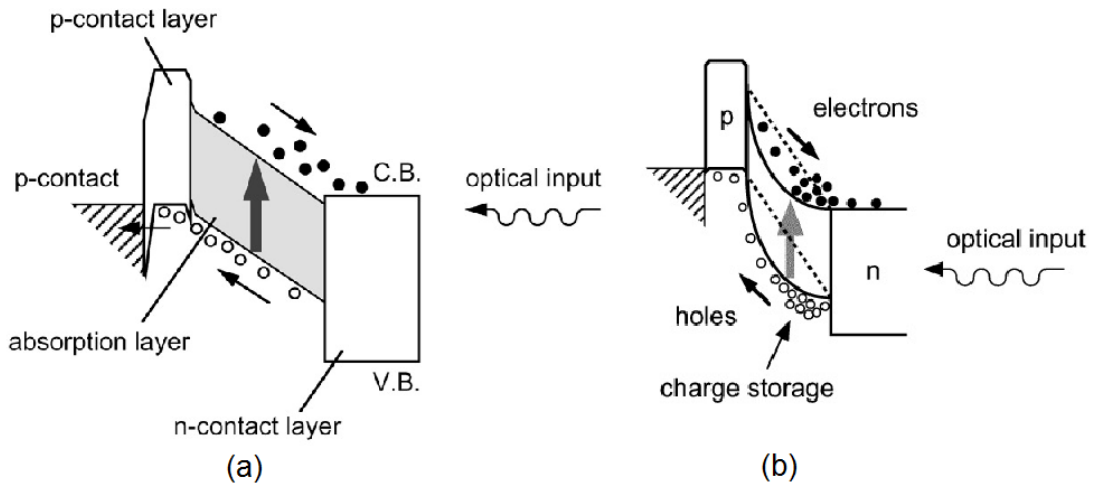
Figure 2-11 (a) Band diagram of PIN-PD and (b) space charge effect of PIN-PD at a high light intensity.
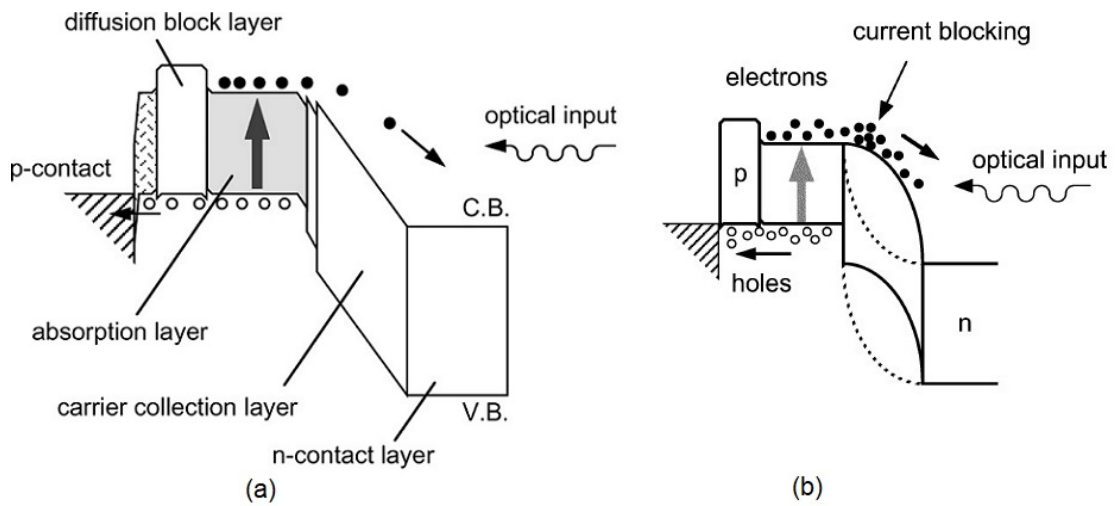
Figure 2-12 (a) Band diagram of UTC-PD and (b) space charge effect of UTC-PD at a high light intensity.

The output power of a photodiode is mainly limited by the space charge effect and thermal management. As shown in Figures 2-11(b) and 2-12(b), at a high light intensity, a

large quantity of EHPs are generated in UTC-PD and PIN-PD. As a result, the internal electric field is reduced by the EHPs, and the output photocurrent saturates. The space charge effect has an adverse effect on both 3-dB bandwidth and output photocurrent.
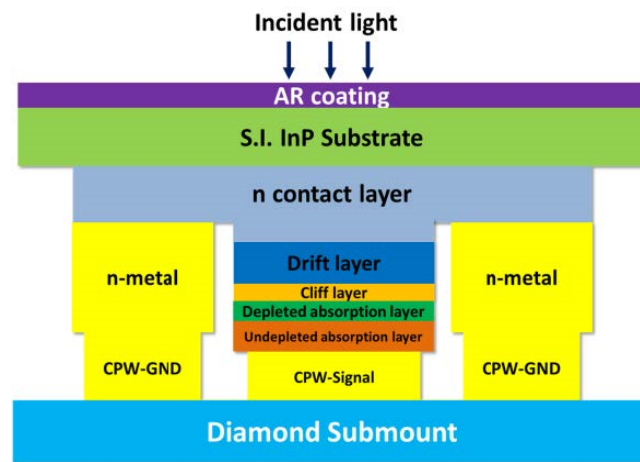
Figure 2-13 Schematic cross-section view of a photodiode flip-chip bonded onto a diamond substrate [34].

At high light injection conditions, a large amount of heat is generated, and the photodiode may burn out at high temperatures. The heat dissipation can be improved by flip-chip bonding the photodiode onto high thermal conductivity materials, such as AlN and diamond substrates. Figure 2-13 shows the schematic cross-section view of a photodiode flip-chip bonded onto a diamond substrate.

2.6 Summary

In this chapter, the fundamentals of InGaAs/InP photodiodes were introduced. Firstly, the types of semiconductor photodetectors and photodetector materials were introduced. Secondly, the geometric structure (surface illuminated photodiode and waveguide photodiode) and epitaxial layer structure (PIN photodiode and UTC photodiode) were

illustrated. Thirdly, the figures of merit of photodiodes were explained. Finally, the speed

and power limitations for photodiodes were discussed.

Chapter 3 Physics-based Device Simulation

Silvaco Atlas is a physics-based device simulation software, which predicts the electrical characteristics based on the device's physical structure and bias condition. The software approximates the operation of the device onto a two- or three-dimensional grid (Appendix A), consisting of a number of grid points called nodes. Then, a set of differential equations derived from Maxwell's Equations is applied onto this grid to simulate the transport of carriers inside the device. The physics-based simulation is predictive and can provide insight into the device. The simulation can capture and visualize theoretical knowledge. Moreover, the simulation is much faster and cheaper than performing experiments. These features make the physics-based simulation a very important methodology in the study of semiconductor devices. In this chapter, the physics equations and models related to the simulation of InGaAs/InP photodiode are introduced. The material properties of InGaAs, InP, and InGaAsP are also given in this chapter.

3.1 Basic equations

Silvaco Atlas is a fully numerical simulator that uses a set of fundamental equations for the calculation within the simulation domain. These equations, which link together the electrostatic potential and the carrier densities consist of Poisson's equation, the continuity equations, and the transport equations. Poisson's equation relates variations in the electrostatic potential to local charge densities. The continuity and the transport equations describe the details that the electron and hole densities evolve as a result of transport processes, generation processes, and recombination processes.

3.1.1 Poisson's equation

Poisson's equation is one of the basic equations that must be solved during the device simulation and is given by [34]

$$\nabla \cdot (\varepsilon \nabla \psi) = -\rho \tag{3.1}$$

where ψ is the electrostatic potential, ε is the permittivity, and ρ is the space charge density. The space charge density ρ is the sum of contributions from all mobile and fixed charges, including electrons, holes, and ionized impurities. ρ is given by

$$\rho = q[n - p + \sum(N_A^- - N_D^+)] \tag{3.2}$$

where n and p are the mobile carrier densities, i.e., electron and hole concentrations, and N_A^- and N_D^+ are the concentrations of the ionized acceptors and donors, respectively. q is the elementary charge. Poisson's equation relates the electrostatic potential to the space charge density. The electric field can be calculated from the gradient of the potential and is given by

$$\vec{E} = -\nabla \psi \tag{3.3}$$

During the device simulation, the carrier concentrations and the potential at each grid point with a given bias are calculated.

3.1.2 Carrier continuity equations

The continuity equations for electrons and holes are given by [34]

$$\frac{\partial n}{\partial t} = \frac{1}{q} \nabla \cdot \vec{J_n} + G_n - R_n \tag{3.4}$$

$$\frac{\partial p}{\partial t} = -\frac{1}{q} \nabla \cdot \vec{J_p} + G_p - R_p \tag{3.5}$$

where $\vec{J_n}$ and $\vec{J_p}$ are the electron and hole current densities; G_n and G_p are electron and hole generation rates; R_n and R_p are electron and hole recombination rates.

3.1.3 The transport equations

The current density equations are also called the transport equations. The Drift-Diffusion Model is the simplest model for charge transport. The drift-diffusion model is adequate for nearly all devices that are technologically feasible. The current flow in the semiconductor device is due to the combination of drift carriers and diffusion carriers. Drift carriers are driven by the electric field, and diffusion carriers are driven by the concentration gradient. The electron and hole current densities using the drift-diffusion model are given by [34]

$$\vec{J_n} = q\mu_n n\vec{E} + qD_n\nabla n \tag{3.6}$$

$$\vec{J_p} = q\mu_p p\vec{E} - qD_p\nabla p \tag{3.7}$$

where $\vec{J_n}$ and $\vec{J_p}$ are electron and hole current densities; n and p are electron and hole concentrations; μ_n and μ_p are electron and hole mobilities; D_n and D_p are electron and hole diffusion coefficients, and q is the elementary charge. The diffusion constants are related to mobilities by Einstein relation ($D = \frac{k_B T \mu}{q}$, where k_B is Boltzmann's constant, T is the temperature, and q is the electronic charge).

In summary, Poisson's equation, the carrier continuity equation, and the transport equations are a set of coupled differential equations that must be solved simultaneously during the device simulation. Once the mesh of the device structure and the bias are specified, these equations must be solved at each grid point of the device structure. Then, the electron and hole concentrations and electrostatic potential at each grid point of the

device structure can be obtained. From these results, the electric field and current density can be calculated throughout the device.

3.2 Mobility models

Electrons and holes inside the semiconductor devices are accelerated by the electric field but influenced by various scattering processes. The mobility of electrons and holes are functions of the local electric field, lattice temperature, doping concentration, and so on. In the simulation of InGaAs/InP photodiodes, concentration dependent mobility model and parallel field mobility model are included.

3.2.1 Concentration dependent mobility model

Generally speaking, the mobility of electrons and holes decreases with an increase in doping concentration due to ionized impurity scattering. Based on the work of Caughey and Thomas, the doping- and temperature-dependent low-field mobilities can be specified by the following equations [34].

$$\mu_{n0} = MU1N.CAUG \cdot \left(\frac{T_L}{300K}\right)^{ALPHAN.CAUG} +$$

$$\frac{MU2N.CAUG\cdot\left(\frac{T_L}{300K}\right)^{BETAN.CAUG}-MU1N.CAUG\cdot\left(\frac{T_L}{300K}\right)^{ALPHAN.CAUG}}{1+\left(\frac{T_L}{300K}\right)^{GAMMAN.CAUG}\cdot\left(\frac{N}{NCRITN.CAUG}\right)^{DELTAN.CAUG}} \quad (3.8)$$

$$\mu_{p0} = MU1P.CAUG \cdot \left(\frac{T_L}{300K}\right)^{ALPHAP.CAUG} +$$

$$\frac{MU2P.CAUG\cdot\left(\frac{T_L}{300K}\right)^{BETAP.CAUG}-MU1P.CAUG\cdot\left(\frac{T_L}{300K}\right)^{ALPHAP.CAUG}}{1+\left(\frac{T_L}{300K}\right)^{GAMMAP.CAUG}\cdot\left(\frac{N}{NCRITP.CAUG}\right)^{DELTAP.CAUG}} \quad (3.9)$$

where N is the local (total) impurity concentration in cm^{-3}, and T_L is the temperature in Kelvin. This model is activated by specifying ANALYTIC in the MODELS statement in Silvaco Atlas code. This model is used along with the CONMOB model since CONMOB specifies doping dependent low field mobilities of electrons and holes.

3.2.2 Parallel field mobility model

At the low electric field, the carrier velocity increases linearly with the electric field. However, due to various scattering processes, including lattice vibrations, impurity ions, and other imperfections, the carrier velocity saturates at the high electric field. The model used in Silvaco Atlas to represent the reduction in the carrier mobility with an increasing electric field is called the parallel field mobility model FLDMOB. The following equations are used to implement field dependent mobility for electrons and holes, which can provide a smooth transition between low field and high field behavior [34].

$$\mu_n(E) = \mu_{n0} \left[\frac{1}{1 + \left(\frac{\mu_{n0} E}{VSATN} \right)^{BETAN}} \right]^{\frac{1}{BETAN}} \tag{3.10}$$

$$\mu_p(E) = \mu_{p0} \left[\frac{1}{1 + \left(\frac{\mu_{p0} E}{VSATP} \right)^{BETAP}} \right]^{\frac{1}{BETAP}} \tag{3.11}$$

where E is the parallel electric field; μ_{n0}, and μ_{p0} are the low field electron, and hole mobilities, respectively, derived from the Caughey-Thomas model; VSATN, and VSATP are the saturation velocities, and BETAN and BETAP are fitting parameters.

3.3 Carrier generation-recombination models

Carrier generation and carrier recombination are processes by which carriers (electrons and holes) are created and eliminated. The semiconductor material will return to equilibrium after being disturbed from it through the carrier generation-recombination process. For undoped semiconductor, the electron and hole concentrations are given by

$$n_0 = p_0 = n_{ie} \tag{3.12}$$

where n_{ie} is the intrinsic carrier concentration and is given by

$$n_{ie} = \sqrt{N_c N_v} e^{-\frac{E_g}{2kT}} \tag{3.13}$$

where N_c and N_v are the effective density of states in the conduction band and valence band. E_g is the energy bandgap. For p-type semiconductor, $N_A \gg n_{ie}$ and $N_D = 0$, where N_A and N_D are acceptor and donor concentrations, respectively. The carrier concentrations can be calculated by the following equations:

$$p_0 \cong N_A \tag{3.14}$$

$$n_0 \cong \frac{n_{ie}^2}{N_A} \tag{3.15}$$

For n-type semiconductor, $N_D \gg n_{ie}$ and $N_A = 0$. The carrier concentrations can be calculated by the following equations:

$$n_0 \cong N_D \tag{3.16}$$

$$p_0 \cong \frac{n_{ie}^2}{N_D} \tag{3.17}$$

In the simulation of InGaAs/InP photodiodes, Shockley-Read-Hall (SRH) concentration-dependent lifetime model and Auger recombination model are included.

3.3.1 SRH concentration-dependent lifetime model

Phonon transitions occur in the presence of a trap (or defect) within the forbidden bandgap of the semiconductor. This is a two-step process, the theory of which was first derived by Shockley and Read and then by Hall. The recombination occurs when an electron falls into a "trap," an energy level within the bandgap caused by the presence of a foreign atom or a defect. The trap cannot accept another electron as long as it's filled. The electron occupying the trap energy can fall into an empty state in the valence band, thereby completing the recombination process. This process can either be deemed as a two-step transition of an electron from the conduction band to the valence band or also as the annihilation of the electron and hole which meet each other in the trap. The minority carrier lifetime has a doping dependence, and it decreases with an increase in impurity concentration. The Shockley-Read-Hall recombination can be modeled as [34]

$$R_{SRH} = \frac{pn - n_{ie}^2}{\tau_n[p + n_{ie}\,exp(\frac{-ETRAP}{kT_L})] + \tau_p[n + n_{ie}\,exp(\frac{ETRAP}{kT_L})]} \tag{3.18}$$

where

$$\tau_n = \frac{TAUN0}{1 + (\frac{N}{NSRHN})} \tag{3.19}$$

$$\tau_p = \frac{TAUP0}{1 + (\frac{N}{NSRHP})} \tag{3.20}$$

Here, ETRAP is the difference between the trap energy level and the intrinsic Fermi level, T_L is the lattice temperature in Kelvin, TAUN0 and TAUP0 are the electron and hole lifetimes, and N is the impurity concentration. This model is activated using the CONSRH parameter of the MODELS statement.

3.3.2 Auger recombination model

The SHR recombination is dominant at low carrier concentration or low light injection. However, at high carrier concentration or high light injection, electrons and holes are more likely to interact directly, which leads to Auger recombination. Auger recombination is a process in which an electron and a hole recombine in a band-to-band transition, but now the resulting energy is given off to the third particle (an electron or hole). The involvement of a third particle affects the recombination rate, and Auger recombination is different from band-to-band recombination. The standard Auger recombination can be modeled as [34]

$$R_{Auger} = AUGN(pn^2 - nn_{ie}^2) + AUGP(np^2 - pn_{ie}^2) \qquad (3.21)$$

where the model parameters AUGN and AUGP are user-definable Auger coefficients.

3.4 Material properties

In this thesis, the InGaAs/InP photodiodes are designed for the optical fiber communication systems working at 1550 nm wavelength. InGaAs is adopted for the absorption layer, and InP is adopted for the collection layer and substrate. InGaAsP, which is lattice matched to InP, is adopted for the transition layers.

3.4.1 Energy bandgap

The photon energy corresponds to 1550 nm wavelength is 0.8 eV. $In_{0.53}Ga_{0.47}As$ with an energy bandgap of 0.73 eV is used to absorb light. All layers except the absorption layer should have energy bandgaps larger than 0.8 eV so that light won't be absorbed in these layers. The energy bandgap for $In_{1-x}Ga_xAs_yP_{1-y}$ material is given by [35]

$$E_g = 1.35 + (0.642 + 0.758x)x + (0.101y - 1.101)y - (0.28x - 0.109y + 0.159)xy \quad (3.22)$$

In order to be lattice matched to InP, the $In_{1-x}Ga_xAs_yP_{1-y}$ material must satisfy the following equation [35]

$$x = \frac{0.1896y}{0.4176 - 0.0125y} \quad (3.23)$$

where x and y are the compositions of Ga and As.

3.4.2 Heterojunction energy band offset
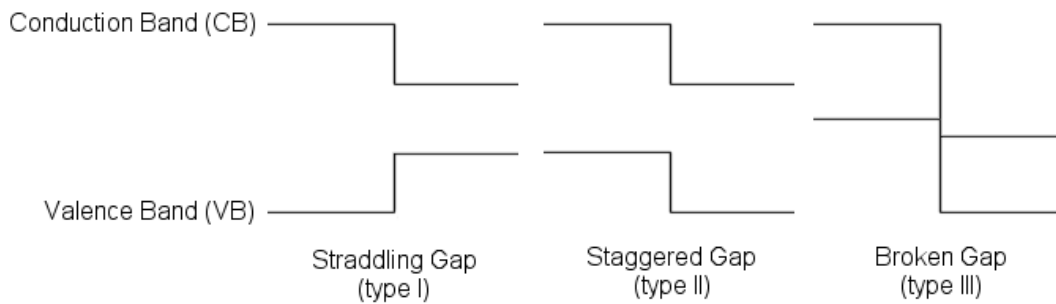
Figure 3-1 Band alignments types at a heterojunction interface (type I, type II, and type III).

The behavior of semiconductor heterojunctions depends on the alignment of the energy bands at the interface. As shown in Figure 3-1, the interfaces of such heterojunctions can be categorized into three types: straddling gap (type I), staggered gap (type II), and broken gap (type III). The most common type is the straddling gap, known as type I heterojunction. The electron affinity rule (also known as Anderson's rule) is used to construct energy band diagrams at heterojunctions between two semiconductors. It states that during the construction of an energy band diagram, the vacuum levels of the semiconductors on either side of the heterojunction should be equal. As shown in Figure 3-2, the heterojunction is formed by two different semiconductor materials having different bandgaps (i.e., E_{G1} and E_{G2}), different work functions (i.e., φ_1 and φ_2), and

different electron affinities (i.e., χ_1 and χ_2). The electron affinity of a material is the energy difference between the edge of the conduction band and the near-surface vacuum. The work function is the minimum energy needed to remove an electron from a solid to a point in the vacuum. The band discontinuities of a heterojunction are given by

$$\Delta E_c = \chi_1 - \chi_2 \qquad (3.24)$$

$$\Delta E_c + \Delta E_v = E_{G2} - E_{G1} \qquad (3.25)$$

This ideal situation is known as the electron affinity rule. There is still some uncertainty about the applicability of this rule, but it provides a good starting point for the discussion of heterojunctions [25].
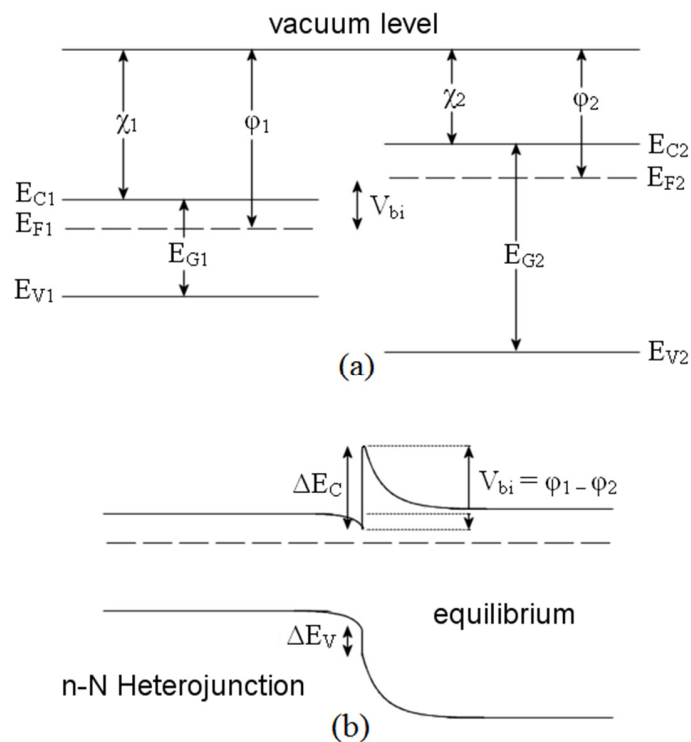
Figure 3-2 Heterojunction between two semiconductor materials with type-I band alignment (a) in isolation (b) in contact.

The energy band alignment (ΔE_c and ΔE_v) at the hererojunction should be considered carefully in the photodiode design since the energy band discontinuities can prevent the electrons and holes from traveling smoothly and rapidly in a semiconductor device. To realize high speed and high output power photodiodes, the energy band discontinuity should be minimized.

For In$_{1-x}$Ga$_x$As$_y$P$_{1-y}$/InGaAs heterojunction, which is lattice matched to InP, the energy band offset (ΔE_c and ΔE_v) can be expressed as follows [35].

$$\Delta E_c(y) = 0.271 - 0.268y + 0.003y^2 \tag{3.26}$$

$$\Delta E_v(y) = 0.35 - 0.502y + 0.152y^2 \tag{3.27}$$

The electron affinity for In$_{0.53}$Ga$_{0.47}$As is 4.58 eV, and the electron affinity for In$_{1-x}$Ga$_x$As$_y$P$_{1-y}$ can be obtained from the above equations. For In$_{1-x}$Ga$_x$As$_y$P$_{1-y}$/InP heterojunction, the energy band offset (ΔE_c and ΔE_v) can be expressed as follows [35].

$$\Delta E_c = 0.268y + 0.003y^2 \tag{3.28}$$

$$\Delta E_v = 0.502y - 0.152y^2 \tag{3.29}$$

3.4.3 Majority carrier relaxation time

In a heavily doped semiconductor material, excess majority carriers will return to thermal equilibrium status within dielectric relaxation time, which is very short. The dielectric relaxation time is given by [25]

$$\tau_d = \frac{\varepsilon_r \varepsilon_0}{\sigma} \tag{3.30}$$

where ε_r is relative permittivity, ε_0 is the permittivity of free space, and σ is conductivity given by

$$\sigma = q(p\mu_p + n\mu_n) \tag{3.31}$$

In InGaAs/InP UTC-PD, the InGaAs absorption layer is p-type, and the doping concentration is supposed to be p=1×10^{18} cm^{-3}. The corresponding hole mobility is μ_p=203 cm^2/(V·s), and the permittivity of InGaAs is 13.9. Therefore, the calculated dielectric relaxation time is τ_d=3.8 ps. The dielectric relaxation time is so short that holes have a minor influence on UTC-PD's performance.

3.4.4 Optical property
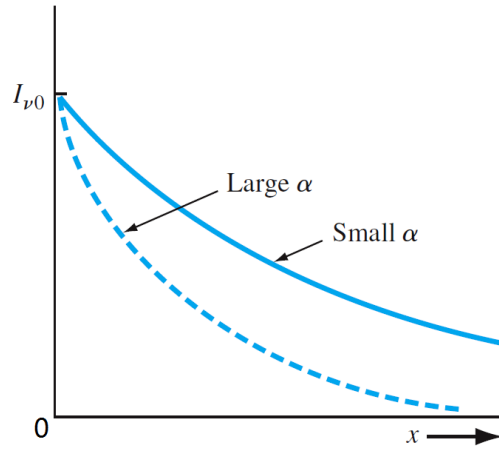
Figure 3-3 Light intensity versus distance for large and small α.

As mentioned in Section 2.2, if the energy E of the injected photons is larger than the semiconductor's energy gap E_g ($E=h\nu \geqslant E_g$), the injected photons will be absorbed, and EHPs will be generated. When the light is injected into a semiconductor material, the light intensity will decay exponentially when it passes through the semiconductor material. The light intensity at a distance x can be calculated by [25]

$$I_v(x) = I_{v0}e^{-\alpha x} \tag{3.32}$$

where I_{v0} is the incident light intensity at $x=0$, α is the absorption coefficient, and x is the traveling distance of light in the semiconductor material. As shown in Figure 3-3, the light is absorbed more rapidly in the semiconductor material with a large α.
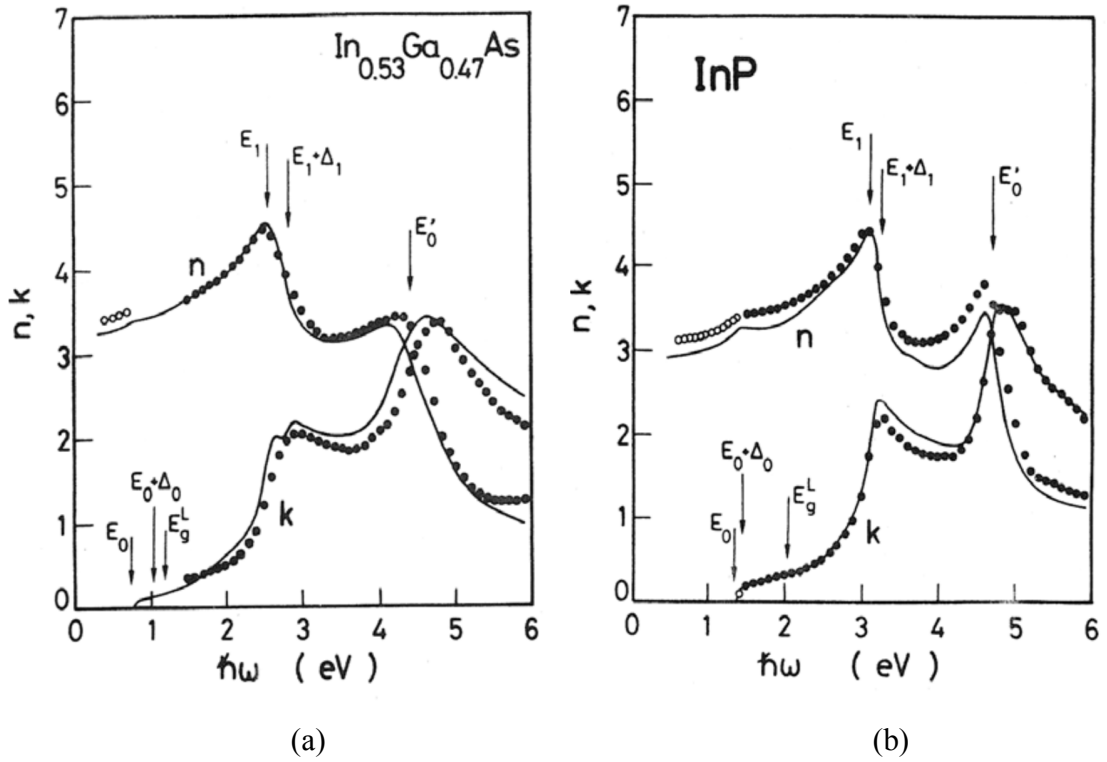
Figure 3-4 Real and imaginary refractive index of (a) InGaAs and (b) InP versus photon energy [35].
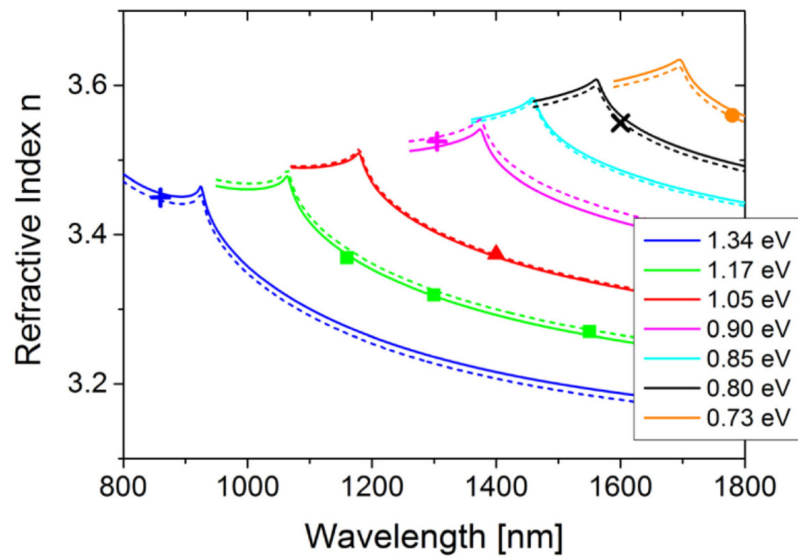
Figure 3-5 Real refractive index of InGaAsP versus wavelength for different material composition (energy bandgap) [37].

The optical property of the semiconductor material can be described as *n+ik*, where *n* is the real part, and *k* is the imaginary part of the refractive index. The relation between α and *k* can be expressed as *α=4πk/λ*. The *n* and *k* parameters of InGaAs and InP at 300K are obtained from [35] and are shown in Figure 3-4. At a wavelength of 1550 nm, the *n* and *k* values for InGaAs are 3.56 and 0.075, respectively. Since the photon energy at 1550 nm (0.8 eV) is smaller than the energy gap of InP (1.35 eV), the *k* value for InP is 0, and light won't be absorbed. The *n* value for InP is 3.17.

The real refractive index n_r of InGaAsP at a given photon energy E can be calculated by [36]

$$n_r^2 = A(y)\left[f(z) + \frac{1}{2}\left(\frac{E_g(T)}{E_g(T)+\Delta_0}\right)^{\frac{2}{3}} f(z_0) \right]$$
$$+ B(y) + \frac{1}{\varepsilon_0}\frac{\partial \varepsilon_\infty}{\partial T}(T-300)$$

(3.33)

where

$$\begin{cases} f(z) = (2 - \sqrt{1+z} - \sqrt{1-z})/z^2 \\ \qquad z = E/E_g(T) \\ \qquad z_0 = E/(E_g(T)+\Delta_0) \end{cases}$$

(3.34)

and

$$A(y) = 8.616 - 3.886y$$

$$B(y) = 6.621 + 3.461y$$

$$\Delta_0 = 0.118 + 0.225y \ (eV)$$

$$E_g(300) = 1.35 - 0.72y + 0.12y^2 \ (eV)$$

A(y) and *B(y)* are fitting coefficients, ε_0 is the dielectric constant of free space, and ε is the high-frequency dielectric constant. *E* is the photon energy of the light. $E_g(T)$ is the energy gap of InGaAsP at temperature *T*, and Δ_0 is the split-off valence bandgap at 300

K. Since we only consider the material property at 300 K, the above calculation for Equation (3.33) can be simplified. The real refractive index n of InGaAsP for different compositions can also be obtained from Figure 3-5, and the value agrees well with Equation (3.33).

3.5 Luminous: optoelectronic simulator

Luminous is a general-purpose program for light propagation and absorption, which is integrated into Silvaco Atlas. Luminous calculates optical intensity profiles within the semiconductor device, and the intensity profiles are then converted into photogeneration rates. This unique feature allows users to simulate electrical responses to optical signals for various optical detectors. In Luminous, there are four physical models for light propagation, including ray tracing (RT), the transfer matrix method (TMM), the beam propagation method (BPM), and finite difference time domain (FDTD) method. Ray tracing is used in the following Silvaco Atlas simulations.

Optoelectronic device simulation can be split into two distinct models that are used to calculate simultaneously at each DC bias point [34].

1. Ray tracing model using the real part of the refractive index to calculate the optical intensity at each grid point.

2. Absorption or photogeneration model using the imaginary part of the refractive index to calculate the carrier concentration at each grid point.

Then, an electrical simulation is performed to calculate the terminal currents.

The schematic for ray tracing in 2D device simulation is shown in Figure 3-6. An optical beam is specified using the BEAM statement. The origin of the beam is defined by

parameters X.ORIGIN and Y.ORIGIN. The ANGLE parameter specifies the propagation direction of the beam. MIN.WINDOW and MAX.WINDOW parameters define the illumination window. As shown in Figure 3-6, the Illumination Window is automatically clipped to the edge of the device. The beam is automatically split into a series of rays so that all of the rays cover the entire width of the illumination window.
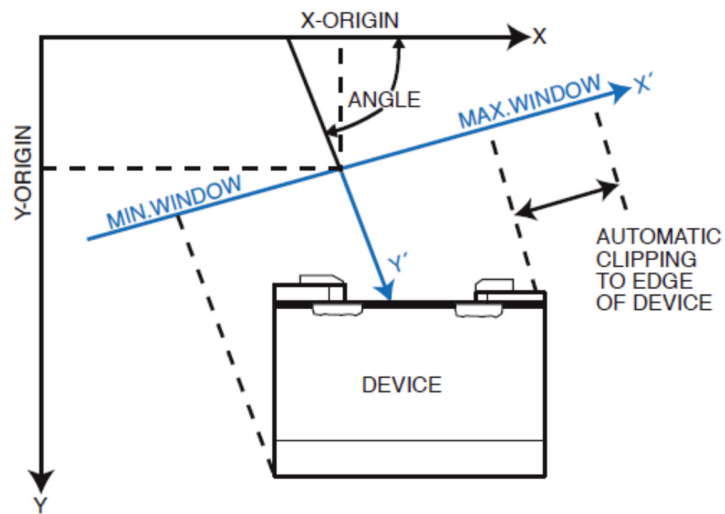
Figure 3-6 Schematic of the ray tracing in 2D [34].

3.6 Summary

In this chapter, the underlying basic equations and physical models of the physics-based device simulator (Silvaco Atlas) were introduced briefly. The material properties of InGaAs, InP, and InGaAsP, including energy bandgap, energy bandgap offset, carrier relaxation time, and optical property, were also presented. Finally, the schematic of ray tracing in Luminous 2D device simulation was introduced.

Chapter 4 High-Speed InGaAs/InP One-Sided Junction Photodiodes with Low Junction Capacitance

4.1 Introduction

The photodiode is the key component for various applications. Thanks to the development of EDFA, by combining high-speed photodiode and powerful EDFA, THz and MMW signals can be generated directly from photonics links. Compared with other THz and MMW signal generation techniques [21], this approach can eliminate the need for bulky and expensive electrical post-amplifiers. Thus, the overall bandwidth can be very broad, and the overall system complexity can be reduced. Moreover, the photodiode can be integrated with a photonic integrated circuit (PIC) component and even with a planar antenna for various applications [8,9,38,39].

Since photodiode is the main limitation for the overall performance of the aforementioned systems, there is an urgent need for high speed and high output power photodiodes. Before the invention of UTC-PD, PIN-PD [27-32] has been used for fiber-optic communications, since it has a broad bandwidth of 67 GHz [27] and over 100 GHz [28,32]. However, for conventional PIN-PD, both holes and electrons are active carriers. Since the holes drift at a lower velocity, the performance of PIN-PD, such as bandwidth, is limited by holes. And thus, there is an inevitable tradeoff between output power and other characteristics.

To overcome the inherent drawbacks of PIN-PD, UTC-PD was first developed in 1997 [33]. Since UTC-PD utilizes fast carrier electrons as the only active carriers, the

speed and output power are improved significantly compared to PIN-PD. In UTC-PD, the absorption layer and depletion layer are separated, which decouples the bandwidths determined by transit time and resistance-capacitance charging time. With the increasing demand for wireless communications, the MMW frequency range from 40 GHz to 300 GHz has attracted more and more attention. MMW-over-fibre (MoF) technique is a promising solution for such wireless communication systems. Nowadays, UTC-PD has been widely used for MoF links. It has been demonstrated that the UTC-PD at C-band wavelength range can have a bandwidth from 20 GHz to 315 GHz [40-48]. All UTC-PD structures, such as stepped doping [40,44,46] or linear-graded doping [41-43,45] in the absorption layer, modified UTC-PD (MUTC-PD) [40], triple transition region photodiode (TTR-PD) [48], and near-ballistic UTC-PD (NBUTC-PD) [41-43,45] have been proposed from the basic UTC-PD structure [33].

To simplify the epitaxial layer structure and improve the performance of photodiodes, a high-speed OSJ-PD with low junction capacitance is proposed and studied here. The OSJ-PD can be an excellent photodiode for optical fiber communications, radio-over-fiber wireless communication systems, MMW, and THz signal generation schemes. The OSJ-PD is proposed based on the concept of the InGaAs Schottky barrier photodiode (SB-PD) [49-53] and UTC-PD [33]. However, since the Schottky barrier height of InGaAs is very low (about 0.2 to 0.3 eV), the dark current of InGaAs SBD is high [51]. This drawback has dramatically limited the applications of InGaAs SB-PD, and there are very few reports on it. Extensive studies have been conducted to overcome this drawback, and different approaches have been adopted to increase the InGaAs Schottky barrier height. These approaches include cryogenic processing of metal deposition [54,55], chemical passivation [56], employing a thin cap layer of InAlAs, InP, Al_2O_3, GaAs or InGaP to

increase barrier height [57-61], adding a thin counter-doped p$^+$-InGaAs layer on n-InGaAs [61-63], etc. However, cryogenic processing and chemical passivation require additional fabrication steps, and employing a thin cap layer will result in energy band discontinuity. Thus, an OSJ-PD structure is desirable without complicating the fabrication process and causing energy band discontinuity.

In this chapter, the OSJ-PD is proposed and studied by theoretical analysis and Technology Computer-Aided Design (TCAD) simulation. Firstly, the epitaxial layer structures and the energy band diagrams of UTC-PD and OSJ-PD are illustrated and compared. Then, the simulated characteristics of UTC-PD and OSJ-PD, including internal electric field distribution, energy band diagram, electron and hole concentration, electron and hole current, frequency response, photocurrent, and junction capacitance are presented and compared.

4.2 Device design and operation

An asymmetrical *pn* junction is called a one-sided junction, either a p^+n junction or an n^+p junction, where p^+ and n^+ indicate heavily doped semiconductor. The schematic diagram of a p^+n junction is given in Figure 4-1. For the p^+n junction, $x_p \ll x_n$ and $W \approx x_n$, where x_p is the depletion width in p^+ region, x_n is the depletion width in *n* region, and *W* is the total depletion width. The heavily doped semiconductor is similar to metal, which has no depletion [64]. As shown in Figure 4-1, almost the whole depletion region extends into the low-doped *n* region and the depletion region in the heavily doped p^+ region is negligible. The OSJ-PD structure is similar to the SB-PD structure [49-53] since the heavily doped *p* contact layer is similar to metal. The epitaxial layer structure of the

designed OSJ-PD is given in Table 4-1. In order to make a comparison, the epitaxial layer structure of the conventional UTC-PD is given in Table 4-2. The detailed numerical modelling study of the conventional UTC-PD is given in [65]. Obviously, the OSJ-PD has a much simpler structure, which can lower the cost for epitaxial layer material growth.

Table 4-1 Epitaxial layer structure of the OSJ-PD.

Layer	Material	Bandgap (eV)	Thickness (nm)	Doping level (cm^{-3})	Dopant type
P Contact	InGaAs	0.734	50	1×10^{19}	P
Absorption	InGaAs	0.734	300	5×10^{15}	Undoped
Spacer	InGaAsP	0.882	20	5×10^{15}	Undoped
Spacer	InGaAsP	1.105	20	5×10^{15}	Undoped
Collector	InP	1.35	300	2×10^{16}	N
N Contact	InP	1.35	800	8×10^{18}	N

Table 4-2 Epitaxial layer structure of the UTC-PD [65].

Layer	Material	Bandgap (eV)	Thickness (nm)	Doping level (cm^{-3})	Dopant type
P Contact	InGaAs	0.73	50	3×10^{19}	P
Block	InGaAsP	0.85	20	2×10^{19}	P
Absorption	InGaAs	0.73	220	1×10^{18}	P
Spacer	InGaAs	0.73	8	1×10^{15}	Undoped
Spacer	InGaAsP	1.00	16	1×10^{15}	Undoped
Spacer	InP	1.35	6	1×10^{15}	Undoped
Cliff	InP	1.35	7	1×10^{18}	N
Collector	InP	1.35	263	1×10^{16}	N
Subcollector	InP	1.35	50	5×10^{18}	N
N Contact	InGaAs	0.73	10	1×10^{19}	N
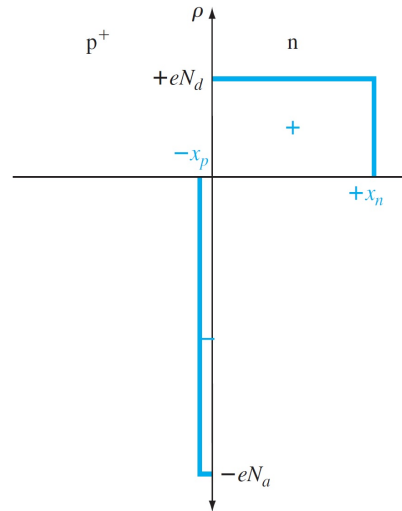
Figure 4-1 Space charge density of a one-sided p^+n junction.

The designed OSJ-PD is a backside illuminated photodiode, operating at around 1550 nm light wavelength. From top to bottom, the OSJ-PD epitaxial layer structure consists of a heavily doped p-type InGaAs contact layer, a lightly doped n-type InGaAs absorption layer, two lightly doped n-type InGaAsP spacer layers, a lightly doped n-type InP collector layer and a heavily doped n-type InP contact layer. This simple structure can be grown by Metal-organic Chemical Vapor Deposition (MOCVD) or Molecular beam epitaxy (MBE).

To better understand the operating mechanism and the advantages of the OSJ-PD, the energy band diagram of the OSJ-PD is given in Figure 4-2(c). The energy band diagrams of the PIN-PD and UTC-PD are also given in Figures 4-2 (a) and (b) for comparison. Light is injected into the bottom N contact layer and passes through the collector layer, which is composed of wide energy gap material InP, and then absorbed in the absorption layer, which is composed of narrow energy gap material InGaAs. The electron and hole pairs are generated in the absorption layer and then separated and swept away quickly by the strong electric field in the absorption layer. This phenomenon differs significantly from the conventional UTC-PD [65], which utilizes electrons as the only active carriers. In the

UTC-PD, electron and hole pairs are generated in the absorption layer, and minority carrier electrons will diffuse/drift to the collector layer. Since electrons' diffusive velocity in the absorption layer is usually lower than the drift velocity in the collector layer, the bandwidth of UTC-PD is mainly dominated and limited by electrons' travelling time in the absorption layer [66].
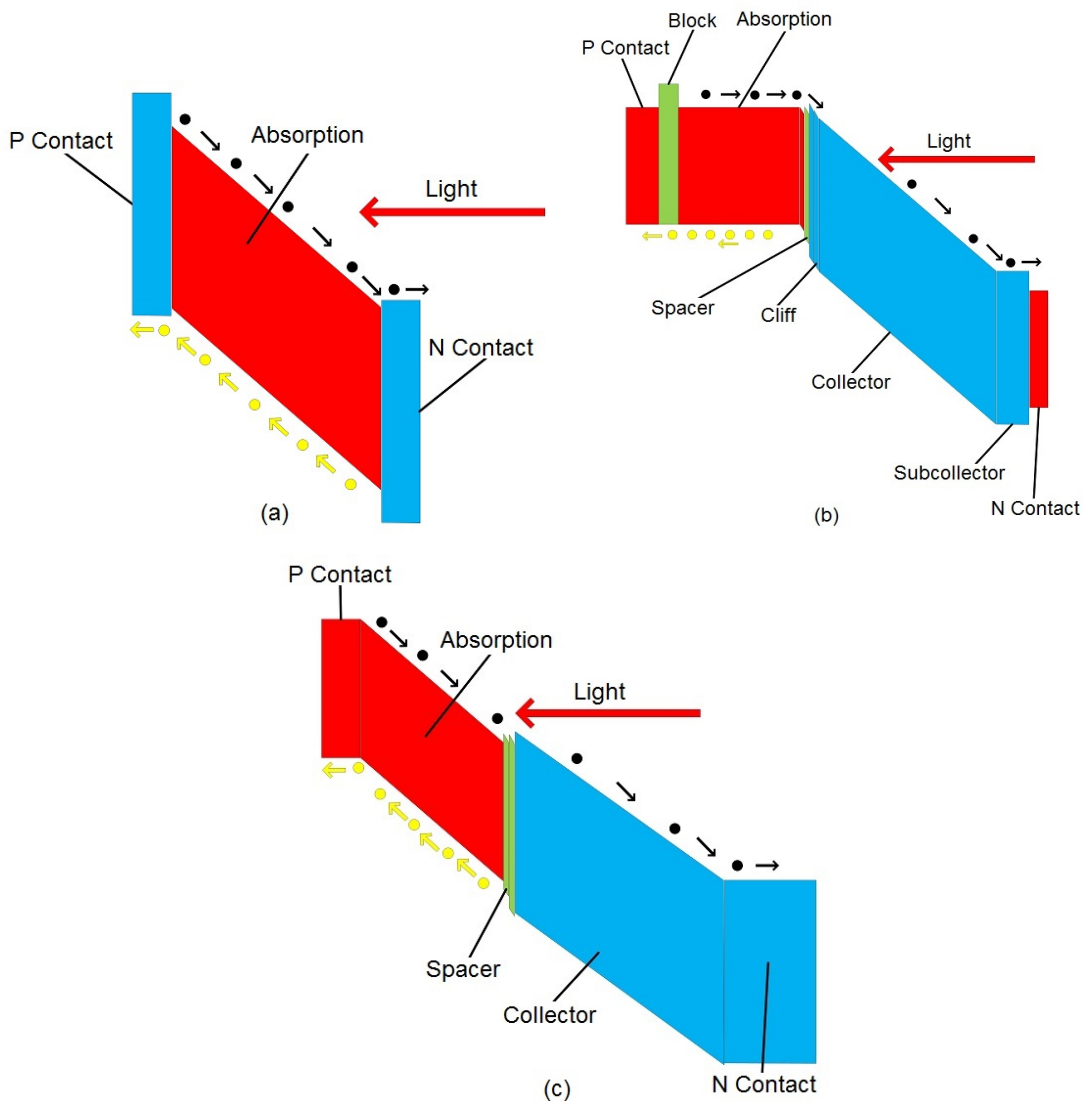
Figure 4-2 Energy band diagram of (a) PIN-PD, (b) UTC-PD, and (c) OSJ-PD.

In the OSJ-PD, since all the active layers are depleted, the slow diffusion process can be eliminated. Both electrons and holes travel at saturation velocity or faster. The

saturation velocities of electrons and holes in InGaAs are 2.5×10^7 cm/s and 5×10^6 cm/s respectively, and the saturation velocities of electrons and holes in InP are 2.6×10^7 cm/s and 6.6×10^6 cm/s respectively [35,66-68]. As shown in Figure 4-2(c), the travelling distance of holes is much shorter than that of electrons. Even though the saturation velocity of holes is slower than that of electrons, the travelling time of electrons and holes can be tuned by carefully designing the thickness of an absorption layer and a collector layer. Generally speaking, the speed of a photodiode, i.e., 3-dB bandwidth, is mainly determined by,

$$f_{3dB} = \frac{1}{2\pi\sqrt{\tau_{tr}^2 + \tau_{RC}^2}}$$

(4.1)

where τ_{tr} is carrier transit time and τ_{RC} is RC charging time. The output power of a photodiode is mainly determined by the space charge effect and thermal management. In OSJ-PD, since the absorption layer and collector layer are separated, the carrier transit time and RC charging time can be adjusted independently. Thus, the OSJ-PD can be designed with a comparable bandwidth to UTC-PD. Because the OSJ-PD is reversely biased at high voltage and the internal electric field is high, the space charge effect can be reduced as well, and thus high output power is achievable.

4.3 Physics model for OSJ-PD

TCAD simulation is used to design and analyze OSJ-PD. The physics-based device simulator ATLAS has been used to predict device performance and provide an in-depth insight view into the physics of device operation [34]. Device characteristics are obtained

by solving the Poisson's equation (Equation 3.1), the continuity equation (Equations 3.4 and 3.5), and the transport equation (Equations 3.6 and 3.7) of electrons and holes.

The electrical and optical properties of InGaAs and InP materials are taken from [35,67,68,69-73]. Basic models included in TCAD simulation are concentration-dependent lifetime model CONSRH, concentration-dependent mobility model ANALYTIC, parallel electric field dependent mobility model FLDMOB, Shockley-Read-Hall recombination minority carrier lifetime model SRH, and Auger recombination model AUGER. In order to verify the accuracy of our simulation models and configurations, we have compared our simulation results with [65,69], and similar results can be reproduced. To make the simulated results comparable, all devices' area is set to 20 μm^2, and load resistance is set to 50 Ω. Excluding contact layers, the UTC-PD has a thickness of 590 nm, and the OSJ-PD has a comparable thickness of 640 nm.

4.4 Device characteristics

4.4.1 Reverse bias voltage and internal electric field

Photodiode serves as an Optical-to-electrical (O/E) converter. In order to get high output, reverse bias voltage should always be applied. However, a high reverse bias voltage could result in device breakdown. The breakdown electric fields of InGaAs and InP are around 2×10^5 V/cm and 5×10^5 V/cm, respectively [72]. In conventional UTC-PD given in Table 3-2, the depletion region is the spacer layers, cliff layer, and collector layer. The total depletion width is around 300 nm. As shown in Figure 3-3(a), at bias voltages of -2 V and -4 V, the electric fields in spacer and cliff layers are around 200 kV/cm and 250

kV/cm respectively, and the electric fields in the collector layer are around 100 kV/cm and
150 kV/cm respectively.
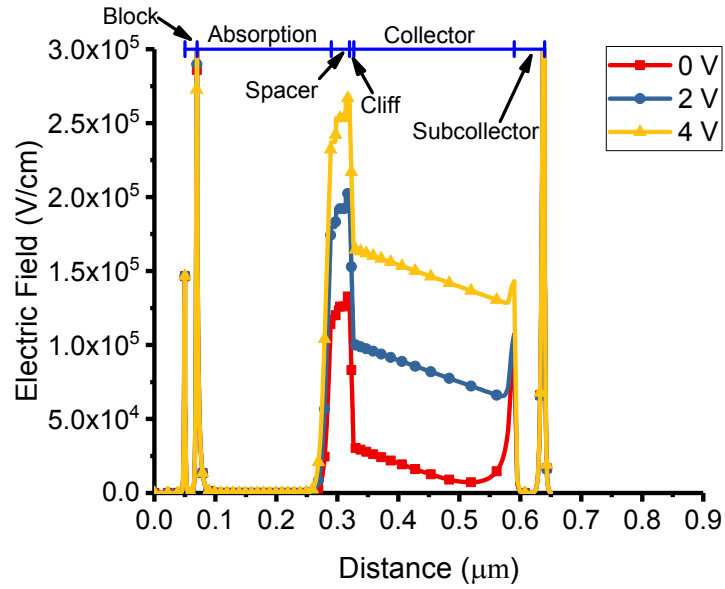
(a)
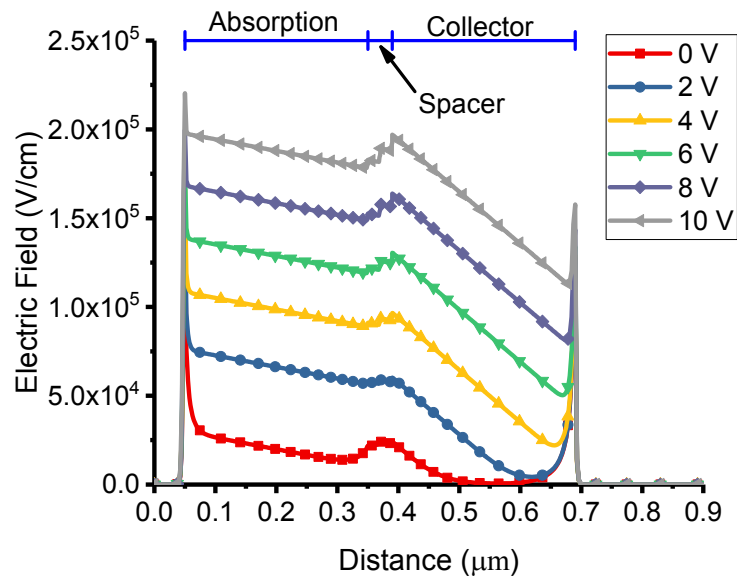
(b)

Figure 4-3 Internal electric field distribution of (a) UTC-PD and (b) OSJ-PD with
different reverse bias voltage.
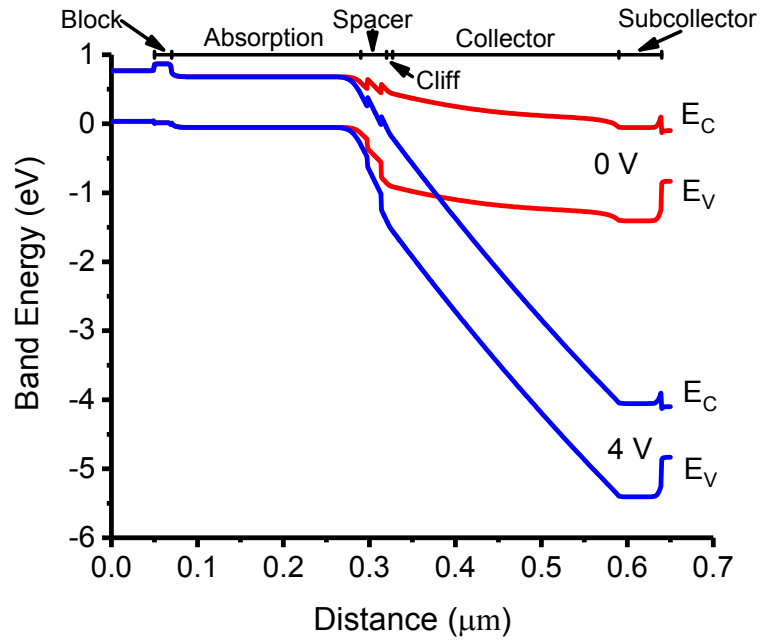
(a)
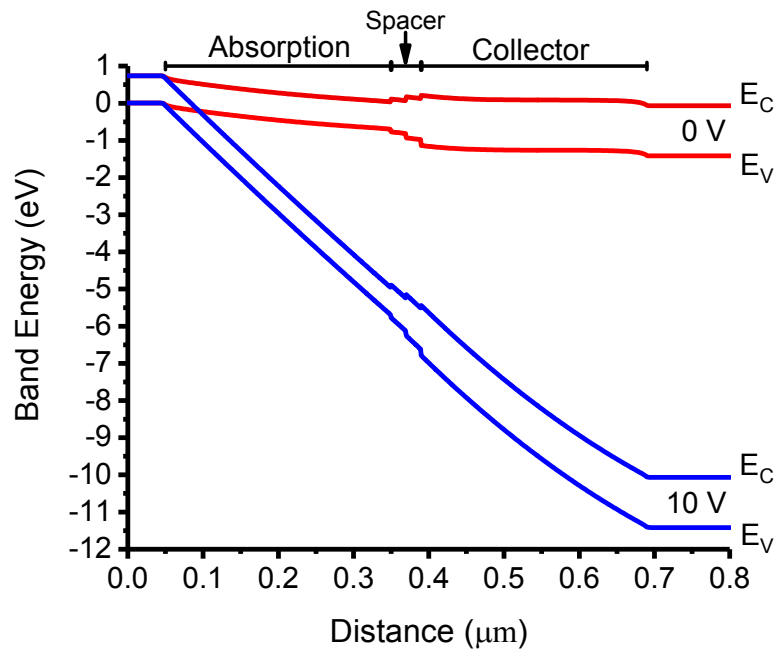
(b)

Figure 4-4 Simulated energy band diagram of (a) UTC-PD and (b) OSJ-PD.

For the OSJ-PD, the situation is completely different. Since all the active layers are depleted, a large reverse bias voltage can be applied without causing device breakdown. The internal electric field of OSJ-PD simulated at a bias voltage of 0, 2, 4, 6, 8, and 10 V is shown in Figure 4-3(b). The one-sided junction structure (similar to Schottky diode, since heavily doped p contact layer is similar to metal.) can produce a 25 kV/cm built-in electric field in the absorption layer without any bias voltage. At a high reverse bias voltage of 10 V, the maximum internal electric field is around 200 kV/cm. Since the depletion width is very large, about 640 nm, the device cannot be broken-down even at a large reverse bias voltage of 10 V, and a large bias voltage can produce higher output current. Thus, the OSJ-PD is suitable for applications that require high RF output power.

4.4.2 Energy band diagram

The energy band diagrams of UTC-PD (Table 4-2) and OSJ-PD (Table 4-1) with and without reverse bias voltage are given in Figure 4-4. Obviously, the operation mechanisms of UTC-PD and OSJ-PD are different. In UTC-PD, the electric field in the absorption layer is almost zero, and a block layer is used to prevent the photogenerated electrons from diffusing towards the contact layer. In OSJ-PD, the electric field in the absorption layer is strong enough, and photogenerated electron and hole pairs will be swept out of the depletion region quickly. Thus, there is no need for a block layer, which is necessary for conventional UTC-PD. Electrons and holes will drift towards n and p contact layers, respectively. This feature differs significantly from the conventional UTC-PD and greatly simplifies the epitaxial layer structure. In UTC-PD, a cliff layer is used to increase the electric field and facilitate the travelling of electrons at the interface between the

absorption layer and the collector layer. In OSJ-PD, the electric field is too high so that

electrons can travel through spacer layers easily, even without a cliff layer.
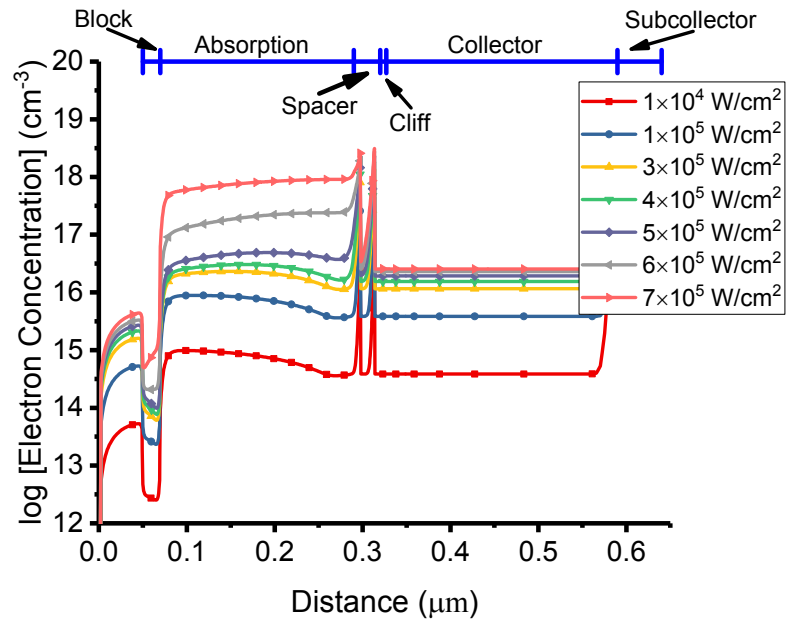
(a)
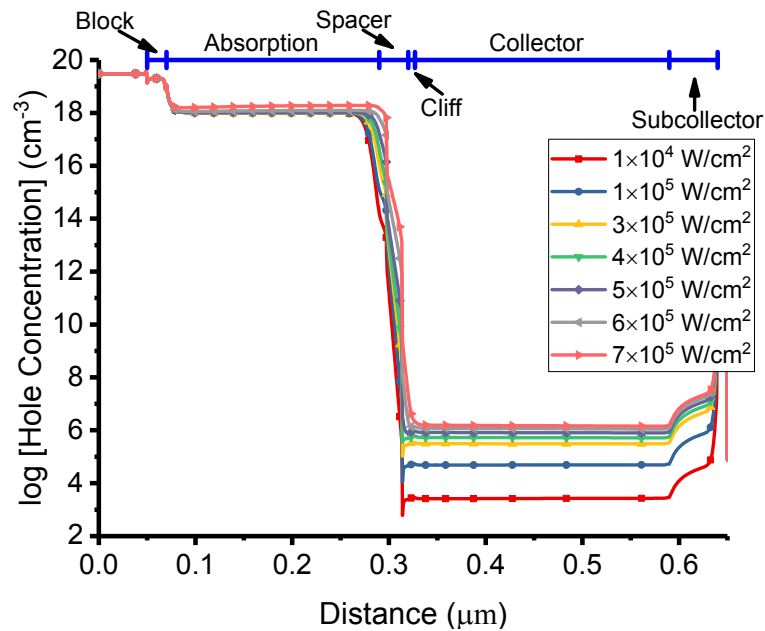
(b)

Figure 4-5 (a) Electron and (b) hole concentration profiles of UTC-PD with 4 V reverse bias voltage at different light intensities.

4.4.3 Electron and hole concentration
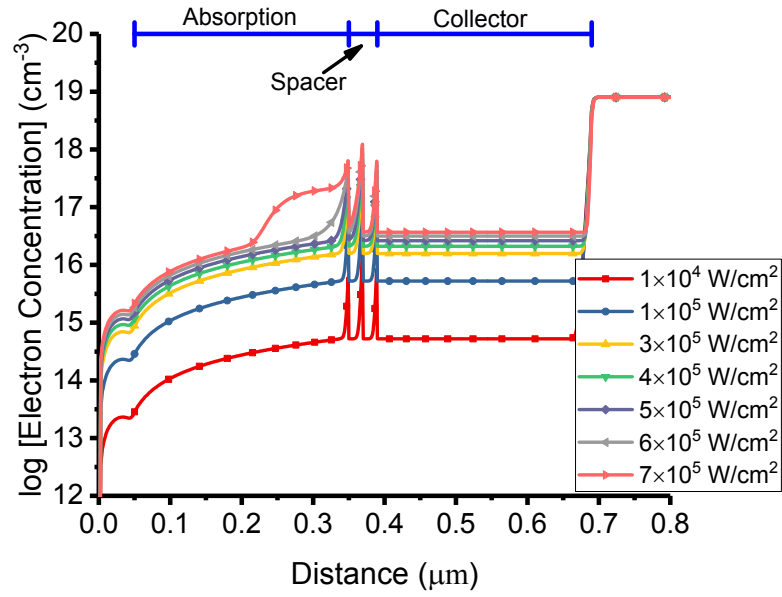
(a)
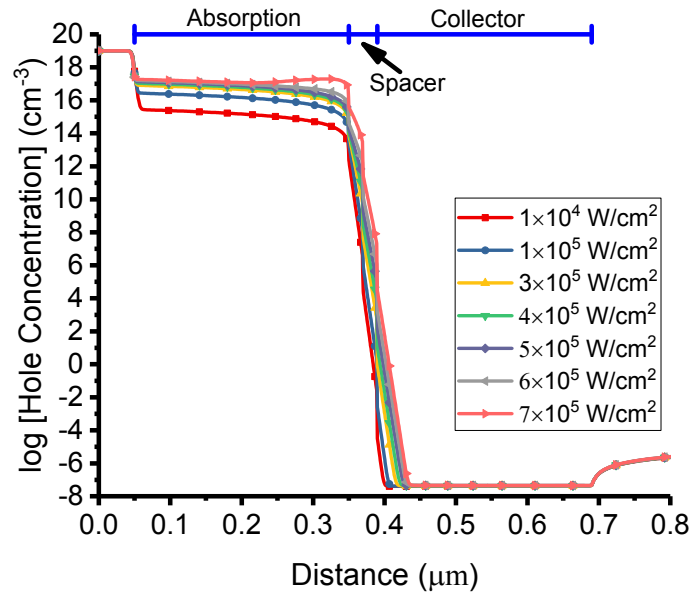
(b)

Figure 4-6 (a) Electron and (b) hole concentration profiles of OSJ-PD with 10 V reverse bias voltage at different light intensities.

For the UTC-PD, the electron and hole concentration profiles across the device are given in Figure 4-5. Light is absorbed in the absorption layer, and EHPs are generated in this layer. Photogenerated electrons diffuse towards spacer layers and then drift through spacer and collector layers under a high electric field. As shown in Figure 4-5(a), electron concentration across the device increases with injected light intensity. However, the electron concentration in the collector layer stops to increase when light intensity goes beyond 5×10^5 W/cm^2. A large amount of electrons begin to accumulate in the absorption layer, and saturation occurs. Since holes are majority carriers in the heavily doped p-type absorption layer, photogenerated holes respond very fast within the dielectric relaxation time, and excess holes will return to equilibrium by the conduction process. As shown in Figure 4-5(b), the hole concentration across the device is almost constant at different light intensities. The variation of hole concentration in the collector layer is mainly due to light absorbed in the 10 nm InGaAs contact (etch stop) layer. Therefore, the photoresponse of a UTC-PD is mainly determined by electron transportation.

For the OSJ-PD, the electron and hole concentration profiles across the device are given in Figure 4-6. The absorption layer is totally depleted. Photogenerated electron and hole pairs are separated by the internal electric field, and electrons and holes drift towards n-type and p-type contact layers, respectively. The photoresponse of an OSJ-PD is determined by both electrons and holes, which is significantly different from a UTC-PD. Thanks to the shorter travelling distance of holes, though holes travel at a relatively low saturation velocity of 5×10^6 cm/s, they won't slow down the overall speed. As shown in Figure 4-6(a), the electron concentration increases with injected light intensity. However, electrons in the absorption layer start to accumulate when light intensity reaches 6×10^5 W/cm^2, and electron concentration in the collector layer stops to increase. As shown in
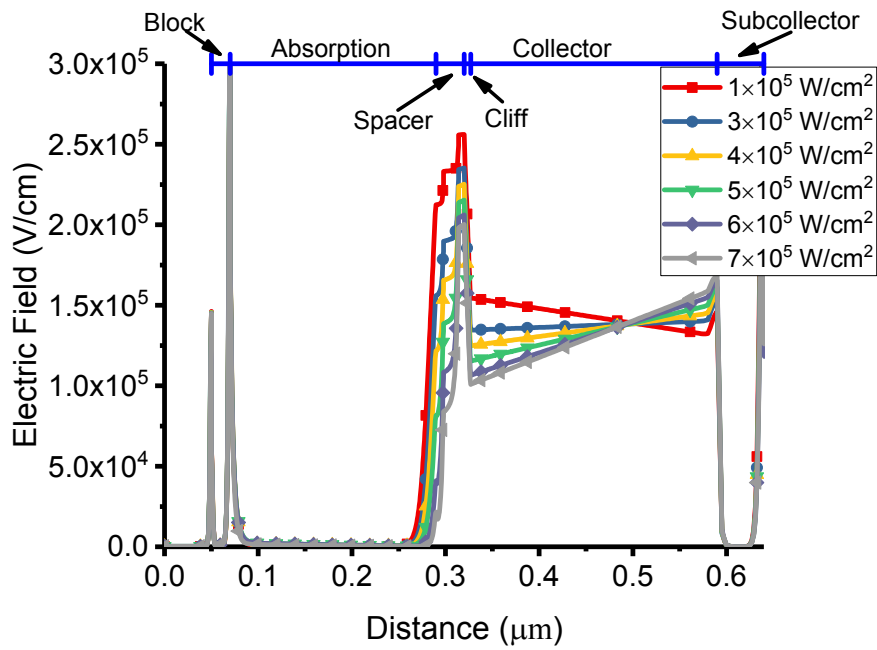
(a)
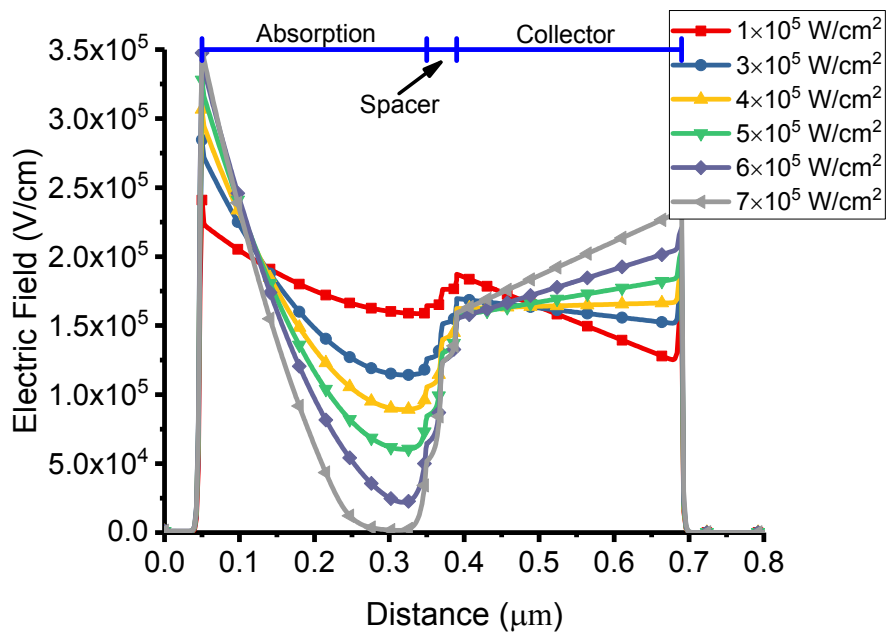
(b)

Figure 4-7 Internal electric field of (a) UTC-PD with 4 V reverse bias voltage and (b) OSJ-PD with 10 V reverse bias voltage at different light intensities.

Figure 4-6(b), the hole concentration across the device is almost constant at different light intensities, except in the absorption layer. In the absorption layer, hole concentration increases with injected light intensity. Obviously, hole accumulation doesn't occur from a low light intensity of 1×10^4 W/cm^2 to a high light intensity of 6×10^5 W/cm^2. Holes start to accumulate near the interface between the absorption layer and the spacer layer at a light intensity of 7×10^5 W/cm^2. At high light intensity, not only holes but also electrons accumulate. The electrons accumulation is mainly caused by conduction band discontinuity between InGaAs and InP. When a large number of electrons accumulate, the internal electric field starts to drop. Once the internal electric field drops to below 40 kV/cm, the travelling velocity of holes starts to decrease, and holes accumulation occurs. Since there isn't any valence band discontinuity between the p contact layer and absorption layer, holes can travel easily from the absorption layer to the *p* contact layer, and holes accumulation is not prominent.

4.4.4 Internal electric field at different light intensities

The internal electric field of UTC-PD with 4 V reverse bias voltage versus different injected light intensities is given in Figure 4-7(a). When light intensity reaches 5×10^5 W/cm^2, the electric field at the interface of the absorption layer and spacer layers drops to zero, and electrons start to accumulate. It agrees well with the phenomenon in Figure 4-5(a) that electron concentration in the collector layer doesn't increase with injected light intensity when it goes beyond 5×10^5 W/cm^2.

The internal electric field of OSJ-PD with 10 V reverse bias voltage versus different injected light intensities is given in Figure 4-7(b). When light intensity reaches 6×10^5 W/cm^2, the electric field at the interface of the absorption layer and spacer layers drops to

below 40 kV/cm, and both electrons and holes start to accumulate. It agrees well with the phenomenon in Figure 4-6(a) that electron concentration in the collector layer doesn't increase with injected light intensity when it goes beyond 6×10^5 W/cm^2.

4.4.5 Frequency response
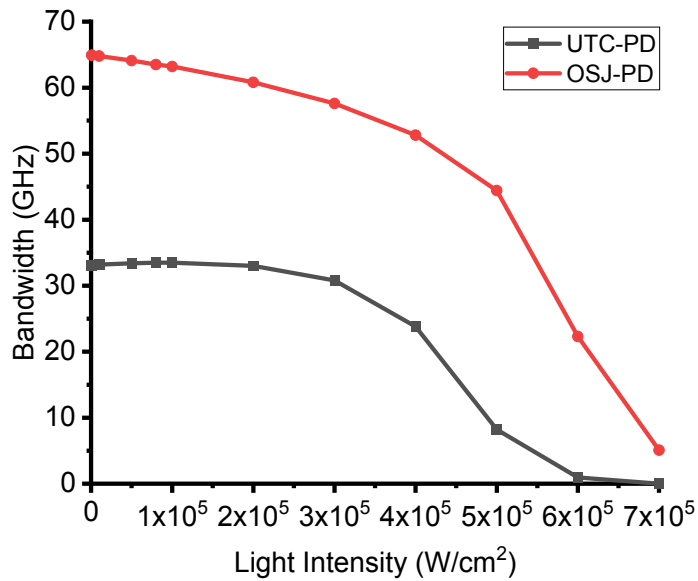
Figure 4-8 Simulated 3-dB bandwidth of UTC-PD and OSJ-PD versus light intensity.

The frequency responses of the UTC-PD and OSJ-PD are obtained by small-signal analysis in TCAD simulation and are given in Figure 4-8. For both UTC-PD and OSJ-PD, because of the space charge effect, the 3-dB bandwidth drops when injected light intensity increases. However, their mechanisms for bandwidth degradation are different. For UTC-PD, electrons are driven by the concentration gradient in the absorption layer. As shown in Figure 4-5(a), an electron concentration gradient is prominent when light intensity is below 4×10^5 W/cm^2, and the gradient vanishes at light intensities above 5×10^5 W/cm^2. The variation of the electron concentration gradient in Figure 4-5(a) agrees well with the

change of 3-dB bandwidth in Figure 4-8. For OSJ-PD, both electrons and holes are driven by an internal electric field. As shown in Figure 4-7(b), the internal electric field drops to zero at a light intensity of 7×10^5 W/cm^2. The variation of the internal electric field in Figure 4-7(b) corresponds well with the change of 3-dB bandwidth in Figure 4-8.

As shown in Figure 4-8, the UTC-PD with a 220 nm absorption layer and 263 nm collector layer has a bandwidth of 33.5 GHz at a low light intensity, while the OSJ-PD with 300 nm absorption layer and 300 nm collector layer has a bandwidth of 64 GHz at a low light intensity.

4.4.6 Photocurrent

The simulated DC photocurrent densities of the UTC-PD and OSJ-PD versus injected light intensity with different bias voltages are given in Figure 4-9. The UTC-PD can achieve a photocurrent density of more than 1.1×10^5 A/cm^2 with a bias voltage of 4 V. The OSJ-PD can achieve a photocurrent density of more than 2.4×10^5 A/cm^2 with a bias voltage of 10 V. In reality, the maximum current density can be improved by thermal management, i.e., flip-chip bonding the photodiode onto high thermal conductive substrates such as AlN or Diamond. Obviously, the reverse bias voltage has a significant influence on the photocurrent, and the photocurrent density usually increases with bias voltage. However, the bias voltage should be lower than the breakdown voltage of the device. Mainly due to the much higher bias voltage, the saturation photocurrent of the OSJ-PD is much higher than the UTC-PD. It's worth mentioning that the space charge effect in the UTC-PD and OSJ-PD can be relaxed by MUTC-PD structure and MOSJ-PD structure, respectively.
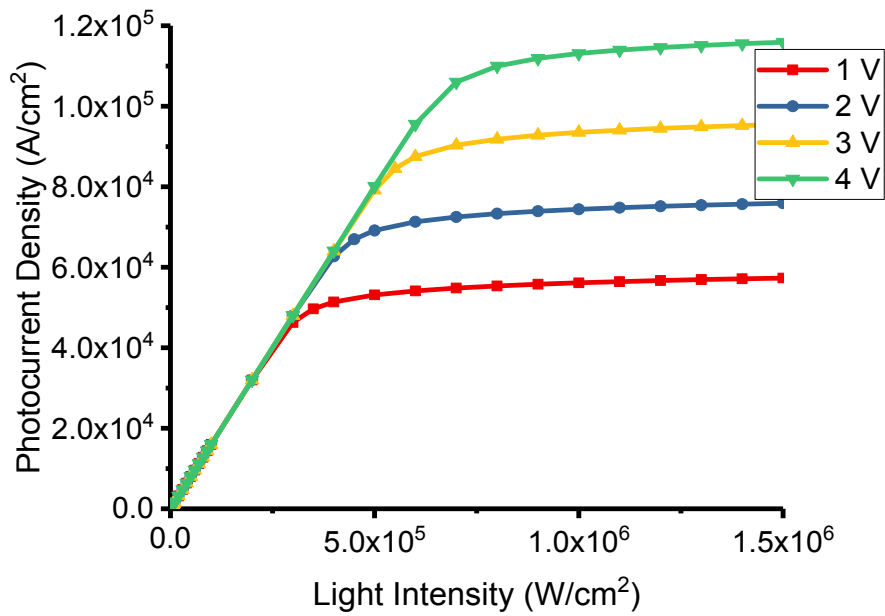
(a)
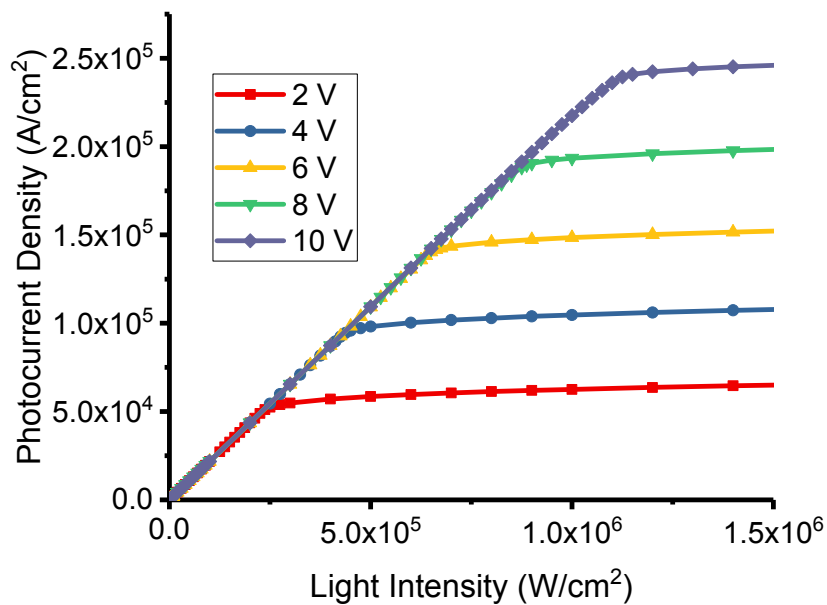
(b)

Figure 4-9 Simulated DC photocurrent density versus light intensity with a different reverse bias voltage of (a) UTC-PD and (b) OSJ-PD.

4.4.7 Junction capacitance

Since the overall speed of the photodiode is determined by transit time and RC charging time (Equation 4.1), another effective way to improve speed is to reduce the RC charging time. The RC charging time can be expressed as,

$$\tau_{RC} = (R_s + R_L)(C_j + C_p) \tag{4.2}$$

where R_s, R_L, C_j, and C_p are series resistance, load resistance, junction capacitance, and parasitic capacitance, respectively. Photodiode with a lower junction capacitance leads to a higher speed. The photodiode junction capacitance is similar to parallel plate capacitance, which is given by

$$C = \frac{\varepsilon_r \varepsilon_0 A}{d} \tag{4.3}$$

where ε_r, ε_0, A, and d are the relative permittivity, the permittivity of free space, area of the junction, and depletion width, respectively. The photodiode has a multilayer dielectric, and the calculation of a multilayer dielectric capacitor is given in Appendix C. In the UTC-PD, the depleted region is the spacer layers, cliff layer, and collector layer. In the OSJ-PD, the depleted region is the absorption layer, spacer layers, and collector layer. Since the depletion width of OSJ-PD is usually larger than UTC-PD, for a device with the same area, the junction capacitance of OSJ-PD can be lower than UTC-PD.

4.5 Conclusions

In this chapter, a novel concept, one-sided junction photodiode, is proposed. The concept of OSJ-PD is different from the UTC-PD in the epitaxial layer structure, internal electric field distribution, energy band diagram, and operation mechanism. It has been demonstrated that the OSJ-PD has the characteristics of the simple epitaxial layer structure,

high speed, high output power, and low junction capacitance. The OSJ-PD with 300 nm absorption layer thickness has achieved a bandwidth of 64 GHz (without considering the external circuit) and a photocurrent density of 2.4×10^5 A/cm^2 under a 10 V bias voltage. The OSJ-PD can become an attractive choice for high-speed fibre-optic communication systems, radio-over-fibre wireless communication systems, and THz and MMW generation schemes in the future.

Chapter 5 Modified InGaAs/InP One-Sided Junction Photodiodes with Improved Response at High Light Intensity

5.1 Introduction

Photodiodes convert optical signals into electrical signals and are widely used in optical fiber communication systems, photonics generation of MMW and THz wave, and radio-over-fiber wireless communication systems. Photodiodes must be capable of generating broadband and high power electric signals to improve the overall system performance. UTC-PD is an excellent candidate for high speed and high power applications since its first invention in 1997. In UTC-PD, light is absorbed in the p-type absorption layer, and electrons are the only active carriers, thus minimizing the influence of slow holes transportation. Consequently, high speed and high power can be achieved by UTC-PD.

Generally speaking, the maximum output power of the photodiode is limited by the space charge effect and heat dissipation. The space charge effect at high light intensity can be reduced by bandgap engineering [40-48,74-78], and heat dissipation can be improved by flip-chip bonding the photodiode onto high thermal conductivity materials, such as AlN and diamond substrates [17,41-43,45,47,74]. To suppress the space charge effect and improve performance characteristics, many derivative structures of UTC-PD have been designed, such as stepped doping [40,44,47] or linear-graded doping [41-43,45] in the

absorption layer, MUTC-PD [40,74,77,78], TTR-PD [48], partially depleted absorption layer [75] and nonuniform doping in the collector layer [76].

The OSJ-PD is briefly introduced in this chapter. Compared with UTC-PD, the OSJ-PD has the advantages of simpler epitaxial layer structure and lower junction capacitance, while the high speed and high power characteristics are maintained. Similar to UTC-PDs, the OSJ-PDs also suffer from space charge effect at a high light intensity. To improve the space charge effect at a high light intensity, a MOSJ-PD is proposed for the first time by inserting a cliff layer into the absorption layer of OSJ-PD.

In this chapter, the MOSJ-PD is proposed and designed by theoretical analysis and TCAD simulation. The performance characteristics of MOSJ-PD are studied carefully. First, the epitaxial layer structure and the energy band diagram of MOSJ-PD are illustrated. Next, the considerations for TCAD simulation are explicitly explained. Then, the space charge effect at high light intensity is analyzed, and the effect of the cliff layer is studied. After that, the simulated characteristics of MUTC-PD [78], OSJ-PD, and MOSJ-PD, including internal electric field distribution, energy band diagram, frequency response, responsivity, photocurrent, junction capacitance, are presented. Finally, discussions and comparisons between MUTC-PD, OSJ-PD, and MOSJ-PD are made.

5.2 Device design and operation

The epitaxial layer structure of the OSJ-PD and MOSJ-PD are given in Table 5-1 and Table 5-2, respectively. The main difference is the absorption layer. A lightly doped p-type cliff layer is inserted into the absorption layer of OSJ-PD, and the energy band diagram can be modified to suppress the space charge effect. In order to make a

comparison between MOSJ-PD and MUTC-PD, the epitaxial layer structure of MUTC-PD [78] is given in Table 5-3, and the energy band diagram of MUTC-PD is given in Figure 5-1.

Table 5-1 Epitaxial layer structure of the OSJ-PD.

Layer	Material	Bandgap (eV)	Thickness (nm)	Doping level (cm^{-3})	Dopant type
P Contact	InGaAs	0.734	50	1×10^{19}	P
Absorption	InGaAs	0.734	280	6×10^{15}	N
Spacer	InGaAsP	0.882	20	6×10^{15}	N
Spacer	InGaAsP	1.105	20	6×10^{15}	N
Collector	InP	1.35	300	2×10^{16}	N
N Contact	InP	1.35	800	8×10^{18}	N

Table 5-2 Epitaxial layer structure of the MOSJ-PD.

Layer	Material	Bandgap (eV)	Thickness (nm)	Doping level (cm^{-3})	Dopant type
P Contact	InGaAs	0.734	50	1×10^{19}	P
Absorption	InGaAs	0.734	50	1×10^{16}	N
Cliff (Absorption)	InGaAs	0.734	230	4×10^{16}	P
Spacer	InGaAsP	0.882	20	3×10^{16}	N
Spacer	InGaAsP	1.105	20	3×10^{16}	N
Collector	InP	1.35	300	3×10^{16}	N
N Contact	InP	1.35	800	8×10^{18}	N

As shown in Figure 5-1, for MUTC-PD, stepped doping in the absorption layer is used to accelerate the slow diffusive transport process of electrons. A cliff layer is inserted between the spacer layer and the collector layer, which can increase the electric field in the depleted absorption layer. Thus, the space charge effect can be suppressed, and the output current can be increased. In MOSJ-PD, a cliff layer is inserted between the

absorption layer and the spacer layer. Different from the MUTC-PD, the cliff layer in MOSJ-PD also serves as the absorption layer. In MOSJ-PD, the electric field in the cliff layer is very high, which reduces the space charge effect and increases the output current. Obviously, the MOSJ-PD has a much simpler epitaxial layer structure than the MUTC-PD. The epitaxial layer material can be grown by MOCVD or MBE. The simple structure can reduce the cost of epitaxial layer material growth. And the fabrication process flow of MOSJ-PD is precisely the same as MUTC-PD.

Table 5-3 Epitaxial layer structure of the MUTC-PD [78].

Layer	Material	Bandgap (eV)	Thickness (nm)	Doping level (cm^{-3})	Dopant type
P Contact	InGaAs	0.73	50	2×10^{19}	P
Block	InP	1.35	100	2×10^{18}	P
Spacer	InGaAsP	1.13	10	2×10^{18}	P
Spacer	InGaAsP	0.89	10	2×10^{18}	P
Absorption	InGaAs	0.73	50	2×10^{18}	P
Absorption	InGaAs	0.73	50	1×10^{18}	P
Absorption	InGaAs	0.73	50	5×10^{17}	P
Absorption	InGaAs	0.73	30	1×10^{16}	N
Spacer	InGaAsP	0.89	10	1×10^{16}	N
Spacer	InGaAsP	1.13	10	1×10^{16}	N
Cliff	InP	1.35	30	3×10^{17}	N
Collector	InP	1.35	300	1×10^{16}	N
Subcollector	InP	1.35	100	1×10^{18}	N
N Contact	InP	1.35	1000	1×10^{19}	N

From top to bottom, the MOSJ-PD epitaxial layer structure consists of a heavily doped p-type InGaAs contact layer, a lightly doped n-type InGaAs absorption layer, a lightly doped p-type InGaAs cliff layer, two InGaAsP spacer layers, a lightly doped n-type InP collector layer and a heavily doped n-type InP contact layer. By inserting a cliff layer

into the OSJ-PD, the energy band diagram and internal electric field can be modified. Thus, improvement in 3-dB bandwidth and output current at high light intensity can be realized.
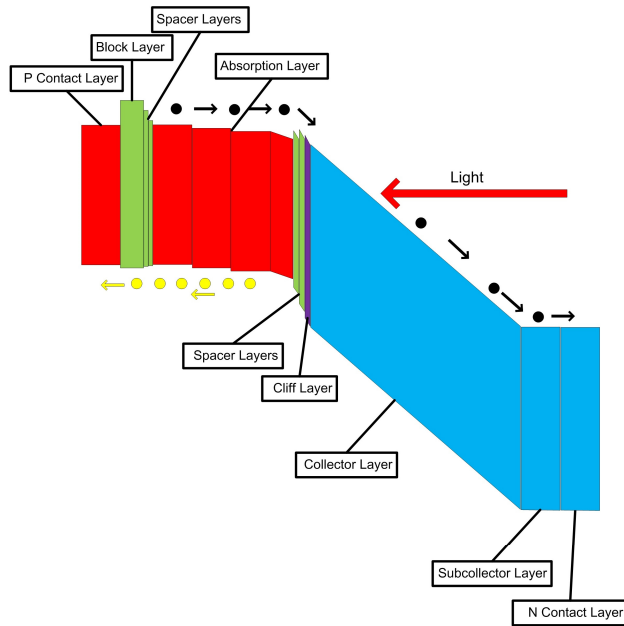
Figure 5-1 Energy band diagram of the MUTC-PD [78].
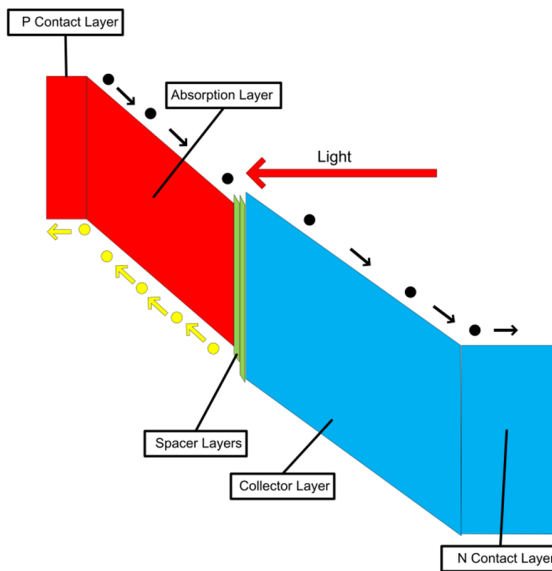
Figure 5-2 Energy band diagram of the OSJ-PD.
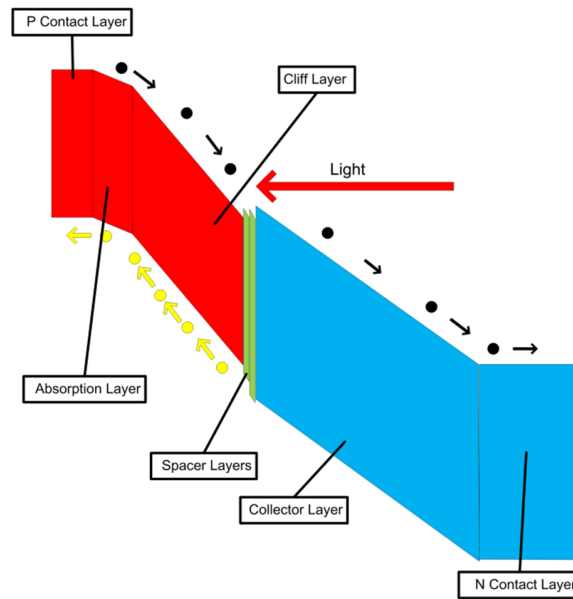
Figure 5-3 Energy band diagram of the MOSJ-PD.

To better understand the operation mechanism and the difference between OSJ-PD and MOSJ-PD, the energy band diagrams of OSJ-PD and MOSJ-PD are given in Figures 5-2 and 5-3, respectively. The designed OSJ-PD and MOSJ-PD are back-sided illuminated photodiodes, operating at around 1550 nm light wavelength. Since InP and InGaAsP are wide bandgap materials, the light at 1550 nm won't be absorbed in these layers. Light is injected into the bottom N contact layer and passes through the collector layer and spacer layers, and then the light is absorbed in cliff and absorption layers. The EHPs are generated in the absorption and cliff layers, and then EHPs are swept away quickly by the strong electric field in the absorption and cliff layers. The difference between OSJ-PD and MOSJ-PD is that the electric field in the cliff layer of MOSJ-PD is higher than the OSJ-PD. Consequently, the space charge effect in MOSJ-PD can be suppressed at a high light intensity.

Similar to OSJ-PD, both electrons, and holes in MOSJ-PD travel at saturation velocity or faster. The saturation velocities of electrons in InGaAs and InP are 2.5×10^{7}cm/s

and 2.6×10^7cm/s respectively. The saturation velocities of holes in InGaAs and InP are 5×10^6cm/s and 6.6×10^6cm/s, respectively. In OSJ-PD, the electric field in the absorption layer collapses at a high light intensity, while in MOSJ-PD, the collapse of the electric field occurs until a higher light injection condition and thus the performance of MOSJ-PD can be improved.

5.3 Simulation considerations

The design of MOSJ-PD is verified by TCAD simulator ATLAS, which is based on the physics model of the semiconductor device. ATLAS can be used to predict the performance of the device and provide a deep insight view into the physics process of the device [34]. In TCAD simulation, the characteristics of the device are obtained by solving the Poisson's equation, the transport equation, and the continuity equation of electrons and holes [34]. In our simulation, concentration-dependent lifetime model CONSRH, concentration-dependent mobility model ANALYTIC, parallel electric field dependent mobility model FLDMOB, Shockley-Read-Hall recombination minority carrier lifetime model SRH, and Auger recombination model AUGER are included. The electrical and optical properties of InGaAs and InP materials are taken from [35,67,68,69-73,79], and the parameters used in our simulation are given in Appendix B. In this chapter, the area of device and load resistance are set to 20 μm^2, and 50 Ω, respectively. And the injected light wavelength is set to 1550 nm.

The TCAD simulation can be used to predict the performance of semiconductor devices. However, there is always a discrepancy between the simulated results and experimental results. It's shown in [65,66,80,81] that the simulated results utilizing the

drift-diffusion model are underestimated compared with the experimental results. It has been demonstrated that the coplanar waveguide (CPW) pad [45,82] and external packaging circuit [83] also have influences on the performance. Even if the same devices are utilized, when combined with different CPW pads and packaging circuits, the results can be different. To our knowledge, the influences of the CPW pad and packaging circuit cannot be simulated in TCAD simulator. This should be one of the reasons which result in discrepancy.

To verify the reliability of the parameters and models used in our simulation, we have compared our simulation with the simulation results in [65,69], and good agreement has been achieved.

5.4 Space charge effect in OSJ-PD and MOSJ-PD

5.4.1 Space charge effect in OSJ-PD

At low light injection conditions, photogenerated EHPs are swept out of the depleted region quickly, and there is no performance degradation. However, at high light injection conditions, the concentration of photogenerated EHPs is very high, which can result in electric field collapse and thus performance degradation. An effective way to suppress the space charge effect is bandgap engineering, which is realized by controlling the composition and doping of semiconductors. Utilizing bandgap engineering, the internal electric field can be modified to counterbalance with the space charge effect. Thus, electric field collapse and output saturation can be relaxed at high light injection conditions.
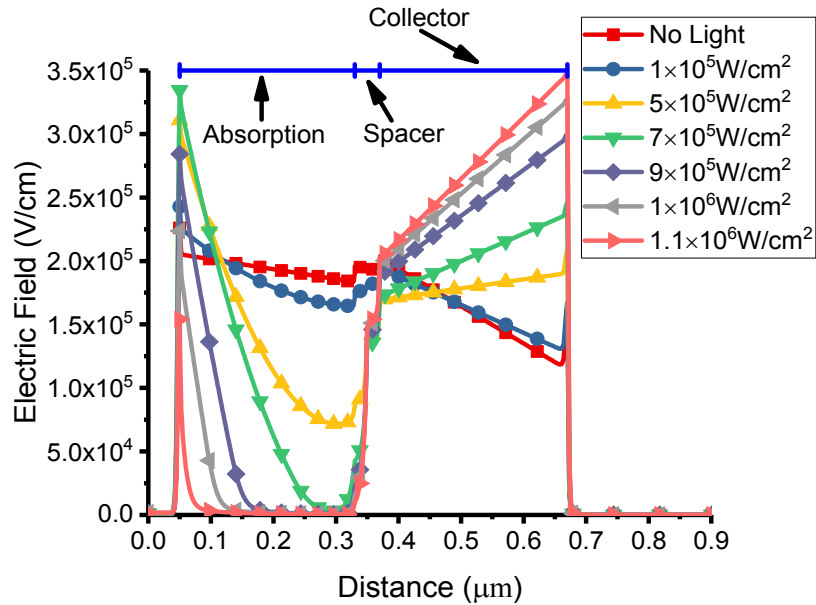
Figure 5-4 Internal electric field of OSJ-PD at the different light intensity with a reverse bias voltage of 10 V.

To have an insight view of the space charge effect in OSJ-PD, the internal electric field at different light intensities is given in Figure 5-4. The electric field in the absorption layer decreases with the increase of light intensity. Because there is a discontinuity in the conduction band between the absorption layer and collector layer, a large number of electrons are accumulated at the interface, which results in the decrease of the electric field. The decrease of the electric field will slow down the travelling speed of holes and makes the situation even worse. As a result, at high light injection, the 3-dB bandwidth decreases and output current saturates. The 3-dB bandwidth versus varying light intensity is given in Figure 5-5. The bandwidth drops to 6.4 GHz and 3.3 GHz at light intensities of 7×10^5 W/cm^2 and 8×10^5 W/cm^2, respectively. In InGaAs, holes travel at saturation velocity under a high electric field. Once the electric field drops to about 40 k V/cm, the travelling velocity of holes will start to drop. The reduction of bandwidth (Figure 5-5) agrees well with the reduction in an electric field (Figure 5-4), which verifies the simulation.
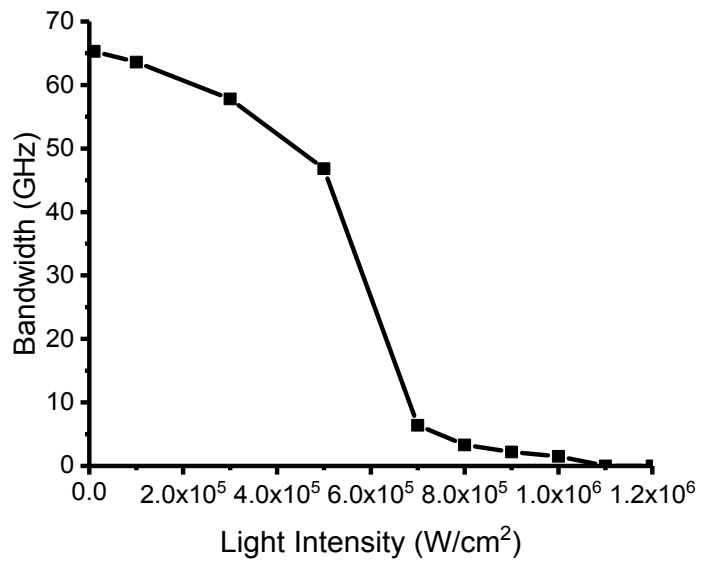
Figure 5-5 3-dB bandwidth of OSJ-PD at the different light intensity with a reverse bias voltage of 10 V.
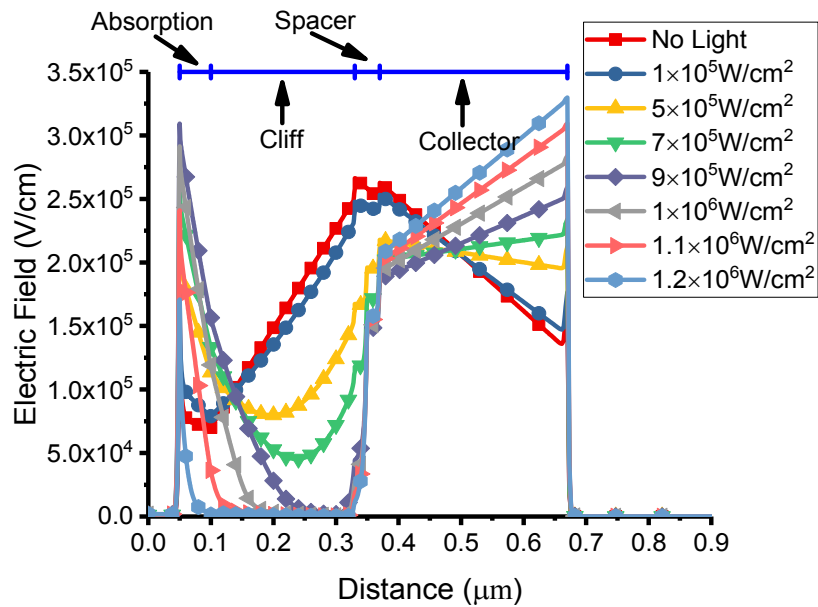
Figure 5-6 Internal electric field of MOSJ-PD at the different light intensity with a reverse bias voltage of 10 V.

5.4.2 Effect of the cliff layer in MOSJ-PD
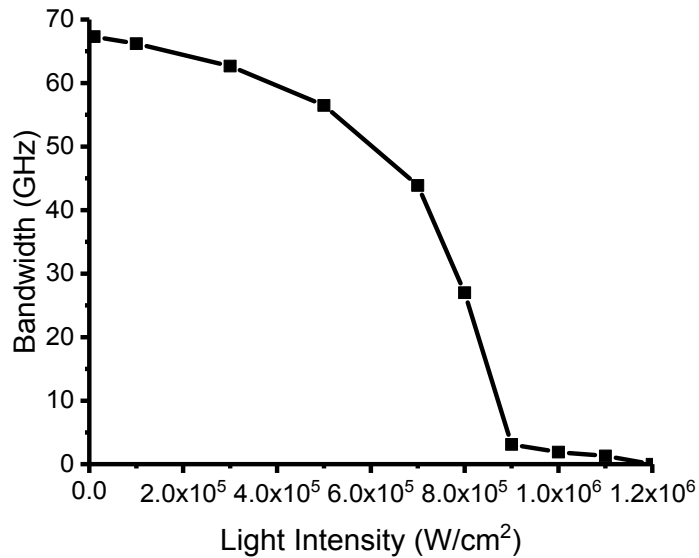
Figure 5-7 3-dB bandwidth of MOSJ-PD at the different light intensity with a reverse bias voltage of 10 V.

To suppress the space charge effect in OSJ-PD, a cliff layer is inserted into the absorption layer. As shown in Figure 5-6, the internal electric field of MOSJ-PD is modified to counterbalance with the space charge effect. The electric field at the interface between the absorption layer and the collector layer drops slower than the OSJ-PD at a high light intensity. As shown in Figures 5-4 and 5-6, the collapse of the electric field occurs at a light intensity of 7×10^5 W/cm^2 in OSJ-PD and 9×10^5 W/cm^2 in MOSJ-PD. The full collapse of the electric field occurs at a light intensity of 1.1×10^6 W/cm^2 in OSJ-PD and 1.2×10^6 W/cm^2 in MOSJ-PD. The collapse of the electric field is the main reason which results in 3-dB bandwidth degradation and output photocurrent saturation. The 3-dB bandwidth of the MOSJ-PD versus different light intensity is shown in Figure 5-7. The 3-dB bandwidths of OSJ-PD and MOSJ-PD are given in Table 5-4, at light intensities of

7×10^5 W/cm^2 and 8×10^5 W/cm^2; the improvements are 37.5 GHz and 23.7 GHz respectively. The function of cliff layers in both MUTC-PD and MOSJ-PD are similar, by modifying the internal electric field distribution, higher bandwidth, and output current can be achieved at high light injection condition.

Table 5-4 Improvement of bandwidth at a different light intensity.

Light Intensity (W/cm^2)	1×10^4	1×10^5	3×10^5	5×10^5	7×10^5	8×10^5	9×10^5	1×10^6	1.1×10^6	1.2×10^6
Bandwidth of OSJ-PD (GHz)	65.3	63.6	57.8	46.8	6.4	3.3	2.2	1.5	0	0
Bandwidth of MOSJ-PD (GHz)	67.3	66.2	62.7	56.5	43.9	27	3.1	1.9	1.3	0
Improvement (GHz)	2	2.6	4.9	9.7	37.5	23.7	0.9	0.4	1.3	0

5.5 Device characteristics

5.5.1 Internal electric field and bias voltage
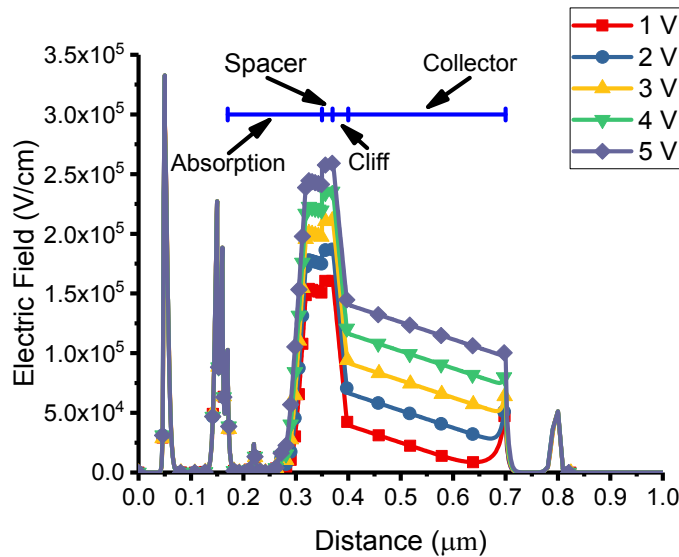
Figure 5-8 Internal electric field of MUTC-PD with different reverse bias voltage.
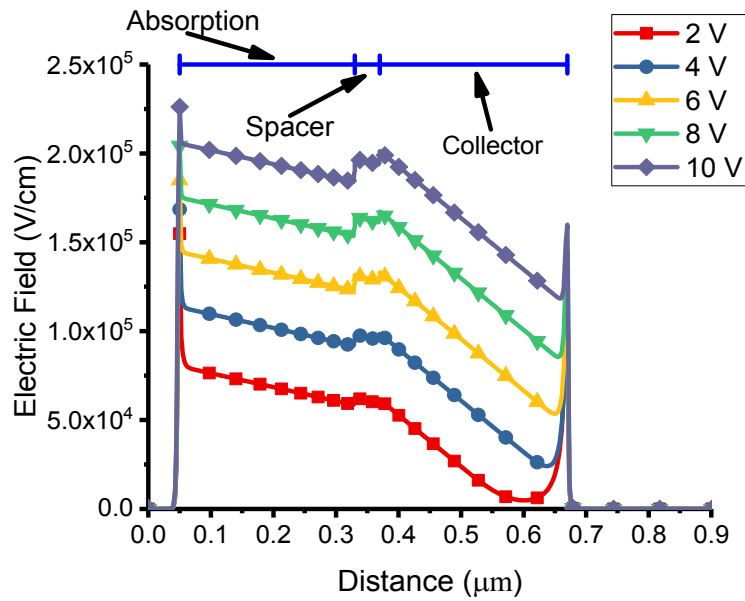
Figure 5-9 Internal electric field of OSJ-PD with different reverse bias voltage.
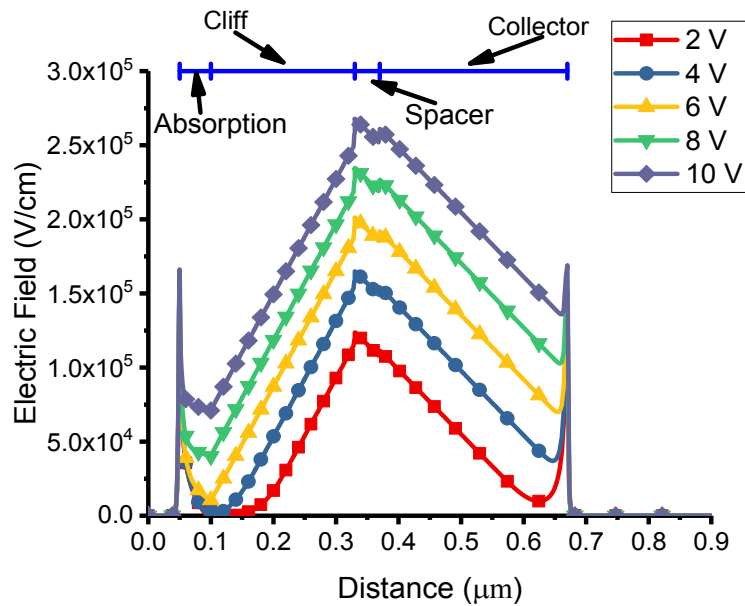
Figure 5-10 Internal electric field of MOSJ-PD with different reverse bias voltage.

The bias voltage has a great influence on photodiodes' performance. Generally speaking, the saturation current increases with bias voltage. However, the bias voltage should be lower than the breakdown voltage. The breakdown electric fields of InGaAs and

InP are around 2×10^5 V/cm and 5×10^5 V/cm, respectively [72]. The simulated internal electric fields of MUTC-PD [78] and MOSJ-PD versus bias voltage are given in Figures 5-8, 5-9 and 5-10, respectively. In order to compare the simulated results of MUTC-PD, OSJ-PD, and MOSJ-PD, the area and load resistance of the devices are set to be the same, 20 μm^2 and 50 Ω, respectively. For the MUTC-PD, the cliff layer can greatly enhance the electric field in the depleted absorption layer and transition layers, which results in a higher output current than UTC-PD. The depleted region includes a 30 nm absorption layer, transition layers, cliff layer, and collector layer. The maximum electric field of MUTC-PD reaches 2.5×10^5 V/cm with a reverse bias voltage of 5 V. In MOSJ-PD, all layers, except the contact layers, are depleted. The cliff layer in MOSJ-PD serves as an absorption layer, and at the same time, it can change the internal electric field distribution. Since the MOSJ-PD has a much larger depletion width, the maximum electric field reaches 2.5×10^5 V/cm with a reverse bias voltage of 10 V. The higher bias voltage is favourable for higher output current.
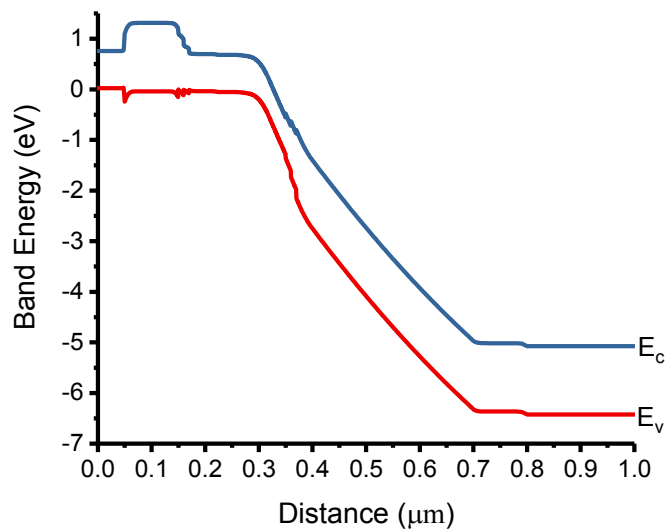
Figure 5-11 Band diagram of MUTC-PD with a reverse bias voltage of 5 V.

5.5.2 Energy band diagram
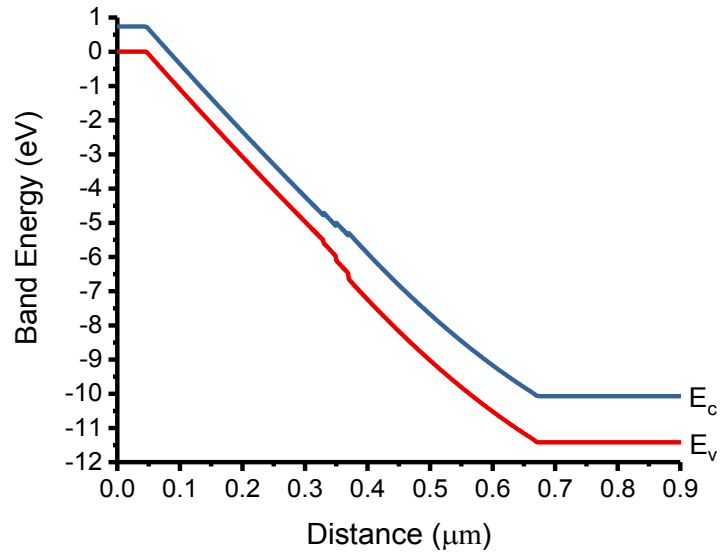
Figure 5-12 Band diagram of OSJ-PD with a reverse bias voltage of 10 V.
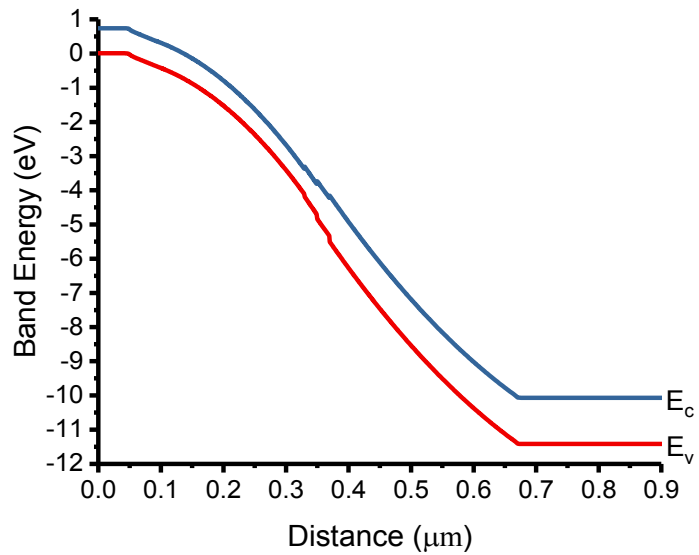
Figure 5-13 Band diagram of MOSJ-PD with a reverse bias voltage of 10 V.

The energy band diagrams of MUTC-PD, OSJ-PD, and MOSJ-PD, are given in Figures 5-11, 5-12 and 5-13, respectively. Obviously, the energy band of MUTC-PD and MOSJ-PD drops steeply at the cliff layer. Generally speaking, the energy band drops more steeply at the higher electric field. The cliff layers in MUTC-PD and MOSJ-PD have the same function, enhancing the electric field and making the saturation occur at higher light injection conditions.

5.5.3 Frequency response
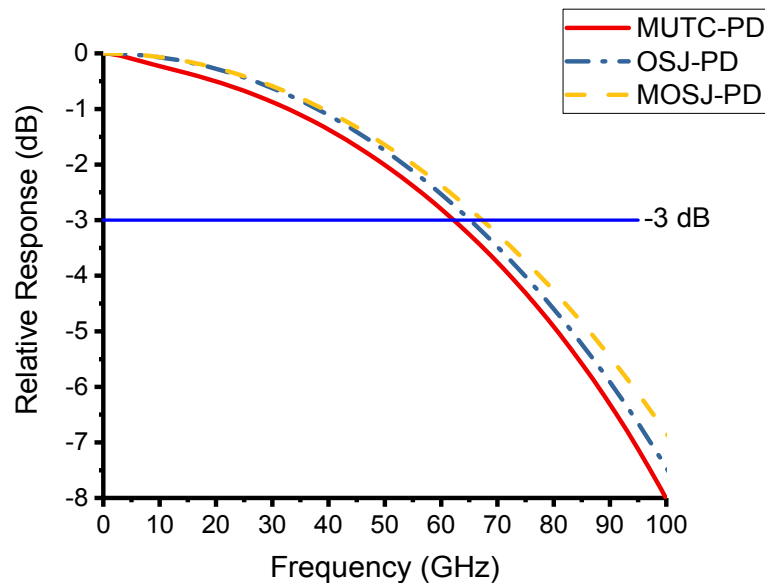
Figure 5-14 Frequency response of MUTC-PD, OSJ-PD, and MOSJ-PD.

The small-signal analysis of MUTC-PD, OSJ-PD, and MOSJ-PD is performed, and the frequency response is given in Figure 5-14. In MOSJ-PD, both electrons and holes travel at saturation velocity under a high electric field. The travelling time of holes is determined by the thickness of the absorption layer and cliff layer, while the travelling time of electrons is determined by the thickness of absorption, cliff, and collector layers.

Different from the MUTC-PD, holes in MOSJ-PD travel at a saturation velocity of 5×10^6 cm/s. Thanks to the shorter travelling distance of holes, holes won't slow down the overall speed. The simulated 3-dB bandwidths of MUTC-PD, OSJ-PD, and MOSJ-PD with 20 μm^2 areas and 50 Ω load resistance are 62.3 GHz, 65.3 GHz, and 67.3 GHz respectively.

5.5.4 Output photocurrent

The output photocurrent of MUTC-PD, OSJ-PD, and MOSJ-PD is studied in this section, and the results are given in Figures 5-15, 5-16, and 5-17. Generally speaking, the output photocurrent increases with bias voltage, and a high reverse bias voltage is favourable for high output power. However, the bias voltage should be lower than the breakdown voltage of the device. As shown in Figures 5-8, 5-9 and 5-10, the depletion width of MUTC-PD is much narrower than the OSJ-PD and MOSJ-PD. The internal electric field of MUTC-PD reaches about 2.5×10^5 V/cm with a reverse bias voltage of 5 V, while the electric field of MOSJ-PD reaches 2.5×10^5 V/cm with a reverse bias voltage of 10 V. With a reverse bias voltage of 5 V, the output photocurrent of MUTC-PD saturates at a light intensity around 9.5×10^5 W/cm^2, and the saturation photocurrent density is 1.22×10^5 A/cm^2. With reverse bias voltage of 10 V, the output photocurrents of OSJ-PD and MOSJ-PD saturate at light intensities around 1.1×10^6 W/cm^2 and 1.2×10^6 W/cm^2, and the saturation photocurrent densities are 2.2×10^5 A/cm^2 and 2.4×10^5 A/cm^2 respectively. Obviously, the high saturation current of OSJ-PD and MOSJ-PD is mainly due to the high reverse bias voltage.
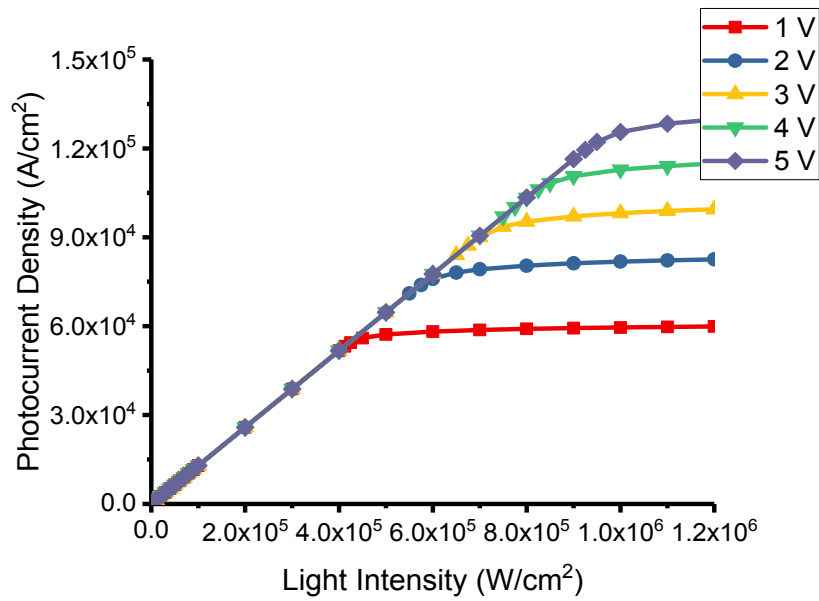
Figure 5-15 Output photocurrent density versus injected light intensity with a different reverse bias voltage (MUTC-PD).
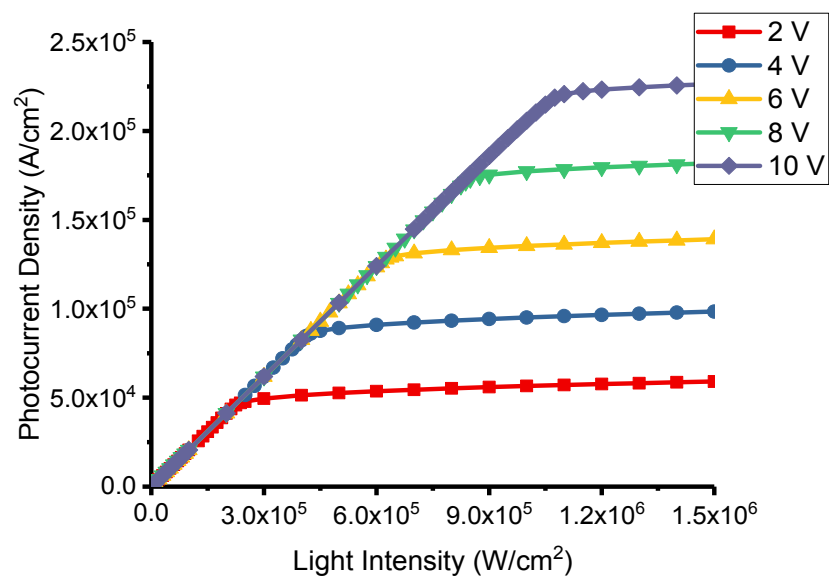
Figure 5-16 Output photocurrent density versus injected light intensity with a different reverse bias voltage (OSJ-PD).
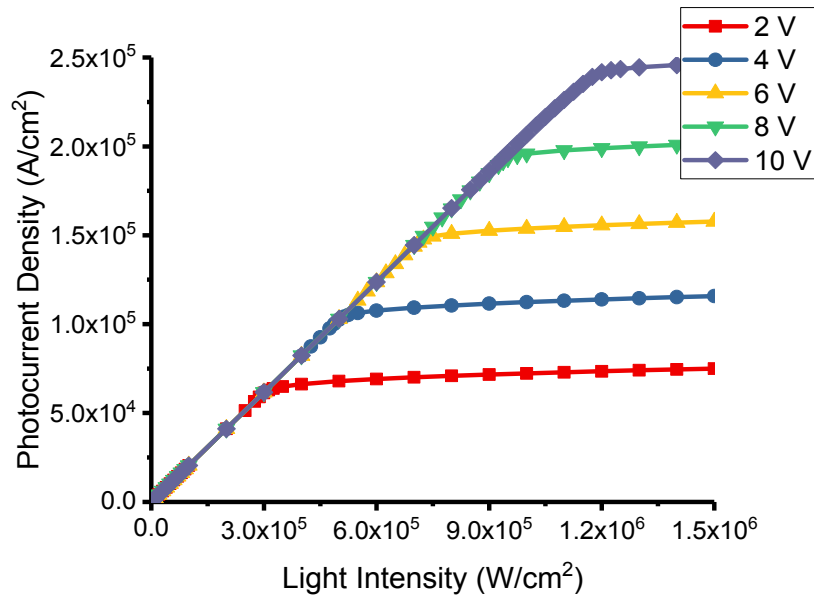
Figure 5-17 Output photocurrent density versus injected light intensity with a different reverse bias voltage (MOSJ-PD).

5.5.5 Responsivity
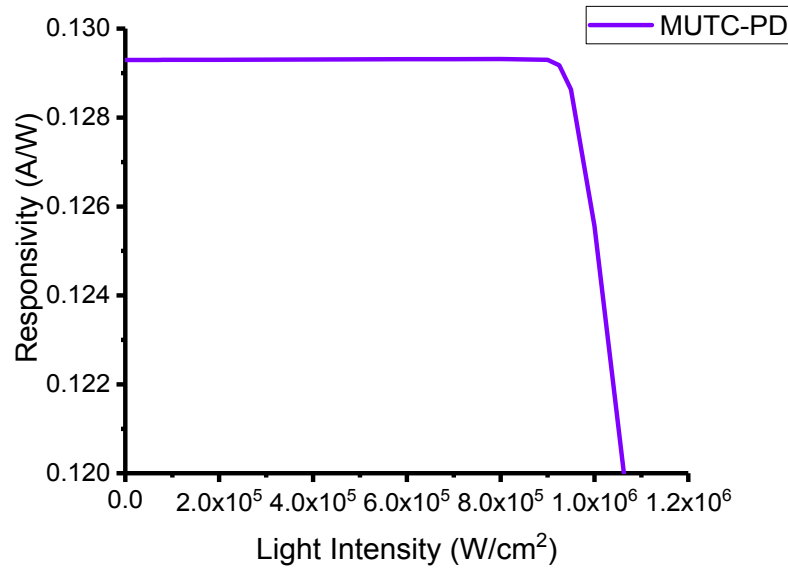
Figure 5-18 Responsivity of MUTC-PD with a reverse bias voltage of 5V.
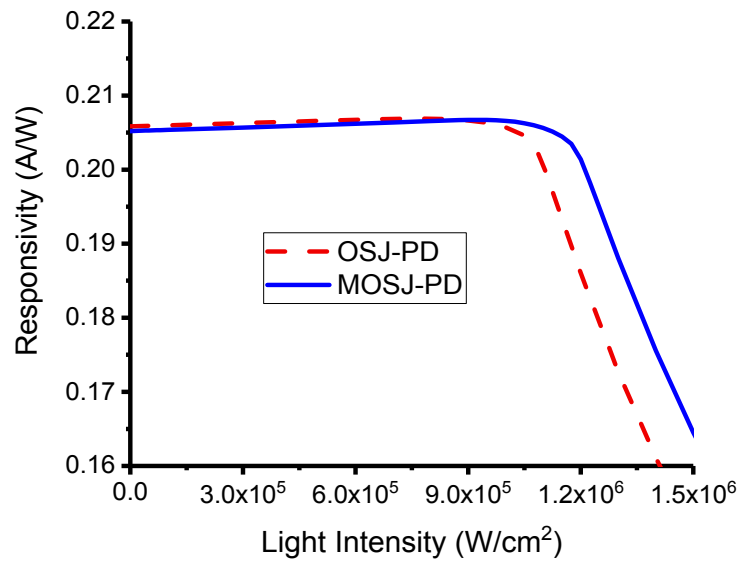
Figure 5-19 Responsivity of OSJ-PD and MOSJ-PD with a reverse bias voltage of 10V.

The responsivity of the MUTC-PD at a reverse bias voltage of 5 V is given in Figure 5-18. The MUTC-PD with a total absorption layer thickness of 180 nm achieves a responsivity of 0.129 A/W. The responsivity of the MOSJ-PD at a reverse bias voltage of 10 V is given in Figures 5-19. In order to make a comparison, the responsivity of the OSJ-PD is also given. The MOSJ-PD with a total absorption layer thickness of 280 nm achieves a responsivity of 0.205 A/W, which is similar to the OSJ-PD. The responsivity of the OSJ-PD begins to drop at a light intensity of 1.1×10^6 W/cm^2, while the responsivity of the MOSJ-PD begins to drop at a light intensity of 1.2×10^6 W/cm^2. This phenomenon agrees well with the electric field collapse shown in Figures 5-4 and 5-6. The internal electric field of the OSJ-PD fully collapses at a light intensity of 1.1×10^6 W/cm^2, while the electric field of the MOSJ-PD fully collapses at a light intensity of 1.2×10^6 W/cm^2. Obviously, the saturation of MOSJ-PD occurs at a higher light intensity.

5.5.6 Junction capacitance

Generally speaking, the overall speed of a photodiode is determined by the carrier transition time τ_{tr} and RC charging time τ_{RC}. The junction capacitance of photodiodes is similar to parallel plate capacitance. The photodiode has a multilayer dielectric, and the calculation of a multilayer dielectric capacitor is given in Appendix C.

The junction capacitance can be lowered by increasing the depletion width. However, the maximum depletion width is limited by the transit time. As shown in Figure 5-8, the fully depleted region in the MUTC-PD includes a 50 nm absorption layer, spacer layers, cliff layer, and collector layer. The total depletion width is about 400 nm. For the MOSJ-PD, all layers, except contact layers, are fully depleted. The total depletion width is about 620 nm. Generally speaking, photodiode with lower junction capacitance is less affected by RC charging time limited bandwidth.
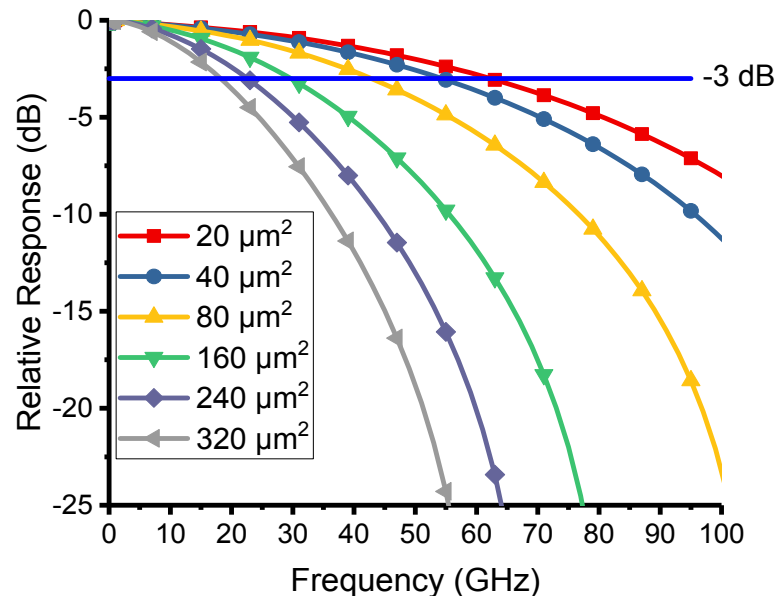
Figure 5-20 3-dB bandwidth of MUTC-PD with different device areas.
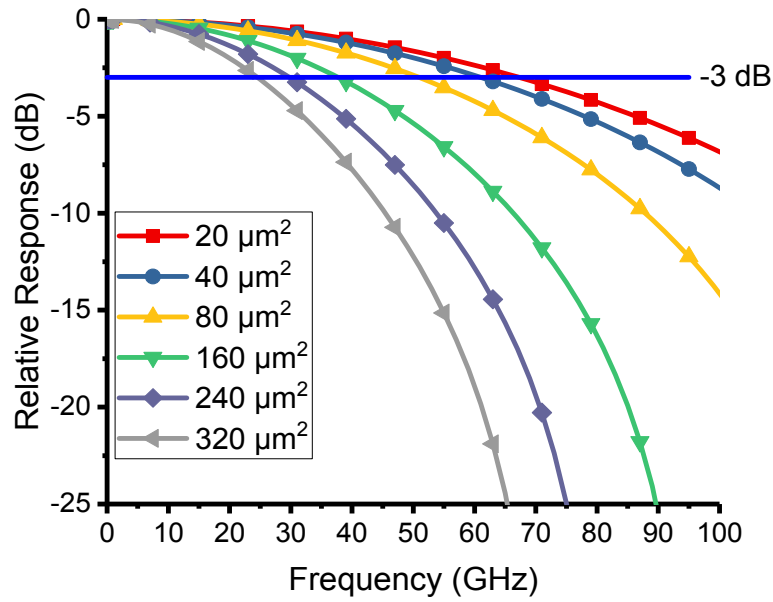
Figure 5-21 3-dB bandwidth of MOSJ-PD with different device areas.

The 3-dB bandwidths of the MUTC-PD and MOSJ-PD with different device areas are given in Figures 5-20 and 5-21. For the MUTC-PD, the device area increases from 20 μm^2 to 320 μm^2, and the 3-dB bandwidth decreases from 62.3 GHz to 18.3 GHz. For the MOSJ-PD, the device area increases from 20 μm^2 to 320 μm^2, and the 3-dB bandwidth decreases from 67.3 GHz to 24.5 GHz. The 3-dB bandwidth of the MUTC-PD and MOSJ-PD is mainly transit time limited with a device area of 20 μm^2 and is mainly *RC* charging time limited with a device area of 320 μm^2.

5.6 Conclusions

To reduce the space charge effect of OSJ-PD at a high light injection condition, a new structure, modified OSJ-PD, is proposed. Compared with the OSJ-PD, the MOSJ-PD has better performance characteristics at high light injection conditions. At the high light

intensity of 7×10^5 W/cm^2, the 3-dB bandwidth of the MOSJ-PD is 43.9 GHz, which is 37.5 GHz higher than the OSJ-PD. With a reverse bias voltage of 10 V, the saturation current density of the MOSJ-PD is 2.4×10^5 A/cm^2, which is 9% higher than the OSJ-PD. Due to the higher reverse bias voltage of MOSJ-PD, the saturation current density is 96.7% higher than the MUTC-PD with a saturation current density of 1.22×10^5 A/cm^2. The MOSJ-PD with a 280 nm absorption layer achieves a bandwidth of 67.3 GHz and a responsivity of 0.205 A/W. Compared with MUTC-PD and TTR-PD, the MOSJ-PD has a much simpler epitaxial layer structure and a lower junction capacitance. In conclusion, the MOSJ-PD has great potential for applications in high-speed fiber-optic communication systems, radio-over-fiber wireless communication systems, and THz and MMW generation schemes.

Chapter 6 InGaAs/InP Evanescently Coupled One-Sided Junction Waveguide Photodiode Design

6.1 Introduction

(a) Topside illuminated

optical input

top contact

Absorber

side contact

Substrate

(b) Backside illuminated

top contact

Absorber

side contact

Substrate

optical input
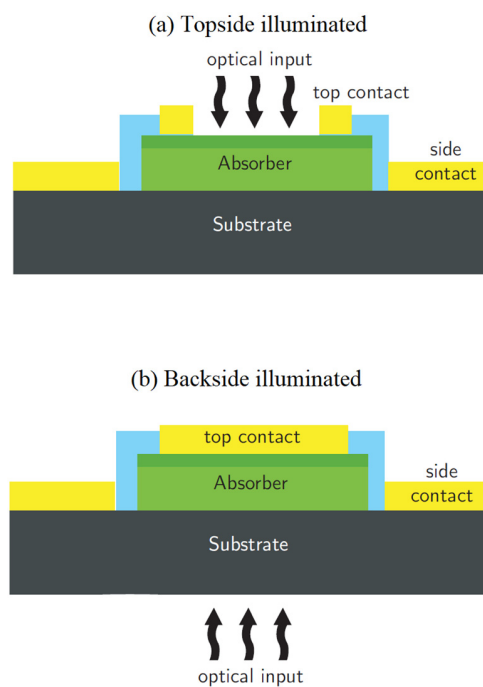
Figure 6-1 Surface illuminated photodiodes: (a) Topside illuminated and (b) Backside illuminated.

Photodiodes convert optical signals into electrical signals and have been widely used in optical fiber communication systems, photonics generation of MMW and THz wave, and radio-over-fiber wireless communication systems. There are mainly three configurations of photodiodes: the surface illuminated (topside illuminated and backside illuminated) photodiode (Figure 6-1) [29-33,40,44,46,84], the side illuminated waveguide photodiode (Figure 6-2) [85-91], and the evanescently coupled waveguide photodiode

(Figure 6-3) [48,92-106,109]. The surface illuminated photodiode has a simpler structure since it does not include the optical waveguide. The surface illuminated photodiode structures include PIN-PD [29-32], UTC-PD [33,38], MUTC-PD [40], etc. The carrier transit time limited bandwidth of the surface illuminated photodiode can be increased by reducing the absorption layer thickness. However, the responsivity decreases with the reduction of the absorption layer thickness. There is always a tradeoff between the bandwidth and the responsivity of the surface illuminated photodiode. For the side illuminated and evanescently coupled waveguide photodiode, the travelling direction of the light is perpendicular to the travelling direction of electrons and holes. The carrier transit time limited bandwidth, and the responsivity can be decoupled. This feature makes the carrier transit time limited bandwidth almost independent of the responsivity. Thus, both high speed (bandwidth) and high quantum efficiency (responsivity) can be achieved for the side illuminated and evanescently coupled waveguide photodiode.
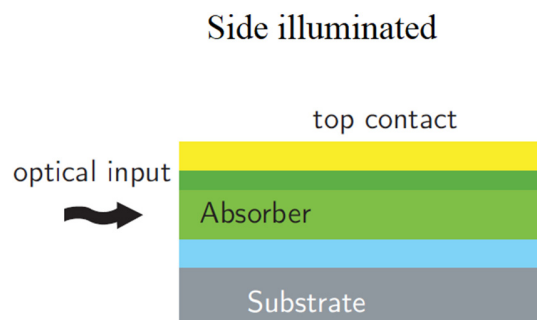
Figure 6-2 Side illuminated waveguide photodiode.
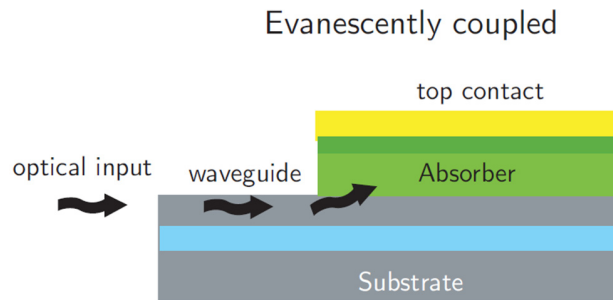
Figure 6-3 Evanescently coupled waveguide photodiode.

For the side illuminated waveguide photodiode, light is directly injected into the edge of the absorption layer. Most of the injected optical energy is focused on the input edge of the waveguide photodiode, which limits the power handling capability of the side illuminated waveguide photodiode [94,95,104]. For the evanescently coupled waveguide photodiode, light is gradually coupled to the photodiode, which allows a more uniform distribution of the optical energy [94,95,98,104]. Thus, an evanescently coupled waveguide photodiode structure has been adopted in our design. Compared to the UTC-PD and MUTC-PD, the OSJ-PD and MOSJ-PD have simpler epitaxial layer structures, while the characteristics of high speed and high output power are maintained [110,111]. Thus, the InGaAs/InP evanescently coupled one-sided junction waveguide photodiode (EC-OSJ-WGPD) is designed and investigated in this chapter.

Earlier works have demonstrated many sides illuminated [85-91] and evanescently coupled [48,92-109] waveguide photodiode structures, but comprehensive numerical analyses of these waveguide photodiodes have been rarely published [103,105,112,113]. The numerical study, which provides information inside the device, such as photogeneration rate and internal optical power distribution, which cannot be experimentally measured, but provide some physical understandings. In addition,

numerical modelling of the waveguide photodiode is an effective way to estimate the performance before the complicated and expensive nanofabrication process. It is the purpose of this chapter to provide a comprehensive numerical modeling procedure and analyses of the EC-OSJ-WGPD.
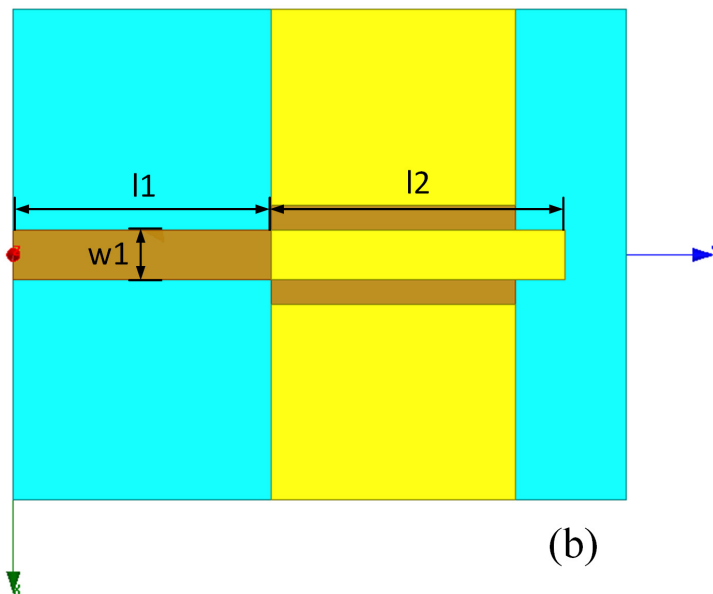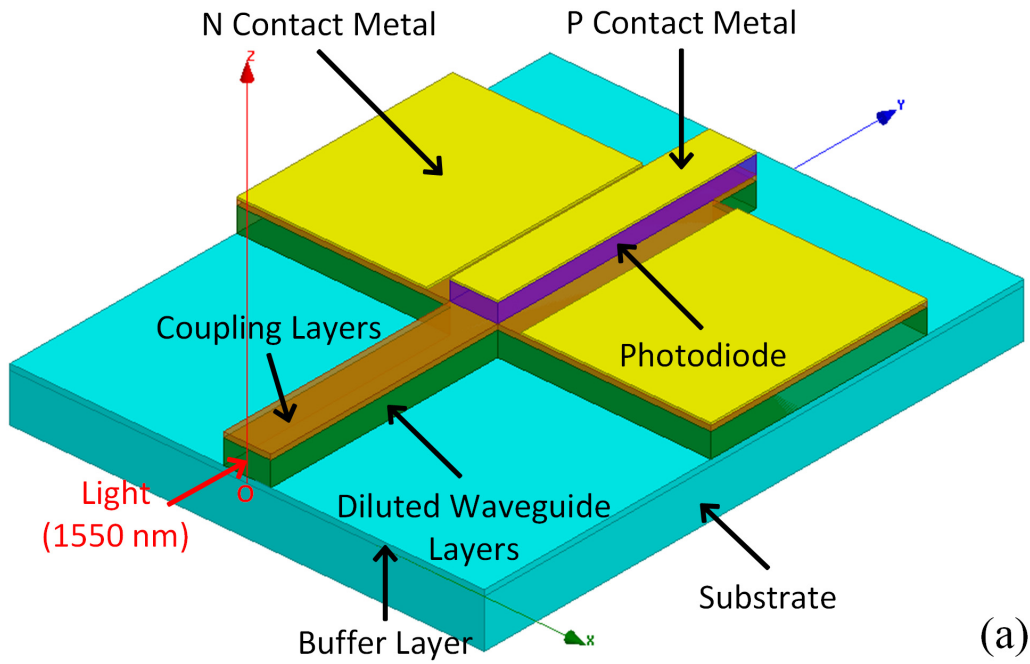
Figure 6-4 EC-OSJ-WGPD structure, (a) 3D view, and (b) top view.

In this chapter, the EC-OSJ-WGPD is simulated by RSoft BeamProp, Lumerical FDTD, and Silvaco Atlas software. The performance characteristics of the EC-OSJ-WGPD are explicitly studied. Firstly, the three-dimensional (3D) structure and the epitaxial layer structure of the EC-OSJ-WGPD are introduced. Next, the EC-OSJ-WGPD is simulated by RSoft BeamProp, and the internal optical power distribution is given. Then, the multiphysics simulation (optical and electrical simulation) procedure is briefly introduced. After that, the simulated characteristics of the EC-OSJ-WGPD, including internal optical power distribution, energy band diagram, internal electric field, photocurrent, and 3-dB bandwidth, are investigated. Finally, a discussion and summary of the EC-OSJ-WGPD are provided.

6.2 3D and epitaxial layer structure

Table 6-1. Epitaxial layer structure of the EC-OSJ-WGPD.

Layer	Material	Thickness (nm)	Doping type and level	
P-contact	$In_{0.53}Ga_{0.47}As$	50	P	1×10^{19}
Absorption	$In_{0.53}Ga_{0.47}As$	350	N	5×10^{15}
Transition	$In_{0.65}Ga_{0.35}As_{0.75}P_{0.25}$	10	N	5×10^{15}
Transition	$In_{0.77}Ga_{0.23}As_{0.5}P_{0.5}$	10	N	5×10^{15}
Transition	$In_{0.89}Ga_{0.11}As_{0.25}P_{0.75}$	10	N	5×10^{15}
Collection	InP	100	N	2×10^{16}
Coupling	$In_{0.77}Ga_{0.23}As_{0.5}P_{0.5}$	250	N	2×10^{18}
Coupling	$In_{0.89}Ga_{0.11}As_{0.25}P_{0.75}$	400	N	2×10^{18}
Coupling	InP	80	Undoped	
Coupling	$In_{0.89}Ga_{0.11}As_{0.25}P_{0.75}$	220	Undoped	
Diluted Waveguide	8 periods of InP/$In_{0.89}Ga_{0.11}As_{0.25}P_{0.75}$ layers	1,600	Undoped	
Buffer	InP	500	Undoped	
Substrate	InP	300,000	Undoped	
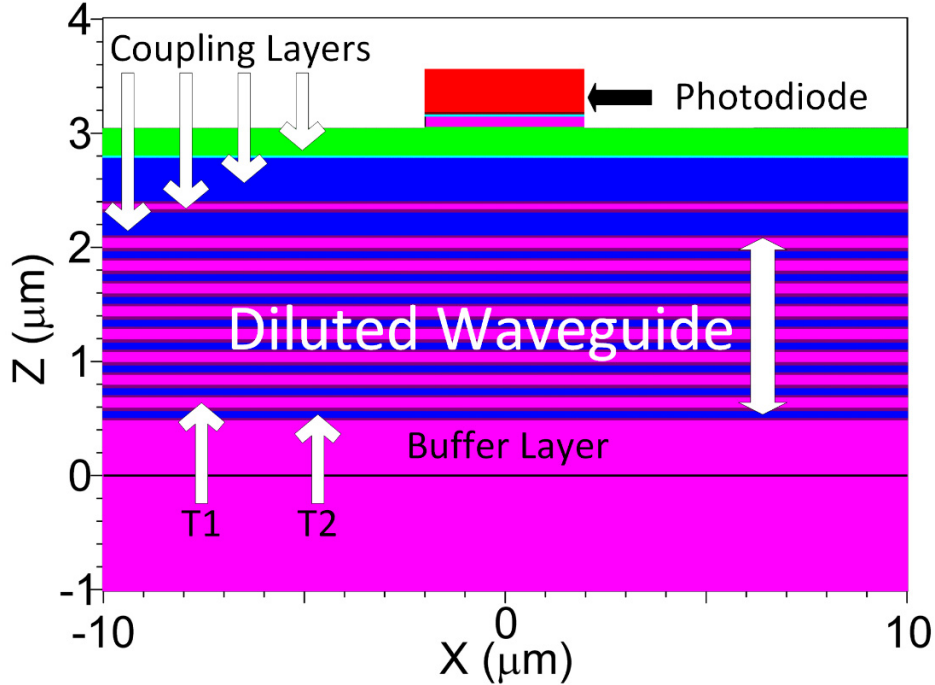
Figure 6-5 Epitaxial layer structure of the diluted waveguide.

The designed EC-OSJ-WGPD structure is shown in Figure 6-4. The width and length of the diluted waveguide are $w1$ = 4 μm and $l1$ = 20 μm, respectively. The length of the photodiode is $l2$ = 20 μm. The epitaxial layer structure of the EC-OSJ-WGPD is given in Table 6-1, and the epitaxial layer structure of the diluted waveguide is shown in Figure 6-5. The design of waveguide photodiode involves many parameters [86], such as the composition and thickness of each quaternary layer (InGaAsP), number of quaternary layers, the thickness of the absorption layer, and thickness of the coupling layers, etc. The thicknesses of the absorption layer and collection layer are 350 nm and 100 nm, respectively. The coupling layers are composed of 4 dielectric layers with different refractive indexes and are given in Table 6-1. As shown in Figure 6-5, the diluted waveguide is composed of 8 periods of InP/In$_{0.89}$Ga$_{0.11}$As$_{0.25}$P$_{0.75}$ layers. The InP layers

(pink layers) have a constant thickness of $T1$=120 nm. The In$_{0.89}$Ga$_{0.11}$As$_{0.25}$P$_{0.75}$ layers (blue layers) have a constant thickness of $T2$=80 nm. All these parameters have an influence on the performance of waveguide photodiode, which will be introduced in the following discussions.

6.3 Beam propagation method simulation

Table 6-2. Material properties used in the optical simulation.

Material	Real refractive index (1550 nm)	Imaginary refractive index (1550 nm)	Energy gap (eV)
InP	3.17	0	1.35
In$_{0.53}$Ga$_{0.47}$As	3.56	0.075	0.74
In$_{0.65}$Ga$_{0.35}$As$_{0.75}$P$_{0.25}$	3.5	0	0.85
In$_{0.77}$Ga$_{0.23}$As$_{0.5}$P$_{0.5}$	3.4	0	0.99
In$_{0.89}$Ga$_{0.11}$As$_{0.25}$P$_{0.75}$	3.25	0	1.16

There are many parameters in the waveguide photodiode design, and it's time-consuming to study the influence of each parameter on the performance. In this chapter, the epitaxial layer structure of diluted waveguide and coupling layers are mainly designed by experience and verified by the RSoft BeamProp 3D beam propagation method (BPM). The structure and parameters of the designed EC-OSJ-WGPD are given in Table 6-1 and Figure 6-5. The simulated TE- and TM-mode optical power distribution and absorption are given in Figures. 6-6 and 6-7.

The material properties used for the optical simulation are given in Table 6-2. The properties of binary material (InP), ternary material (InGaAs), and quaternary material (InGaAsP) can be found in Chapter 4. In$_{1-x}$Ga$_x$As$_y$P$_{1-y}$ lattice matched to InP should satisfy Equation (3.22). The refractive index n_r of InGaAsP at a given photon energy E can be calculated by Equation (3.30).
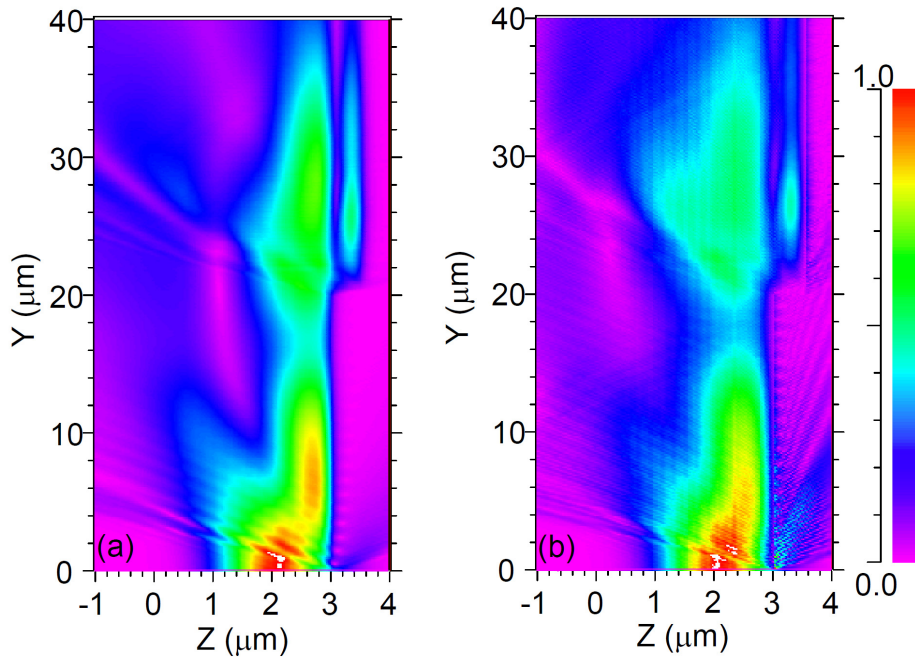
Figure 6-6 Optical power distribution for (a) TE-, and (b) TM-Mode.
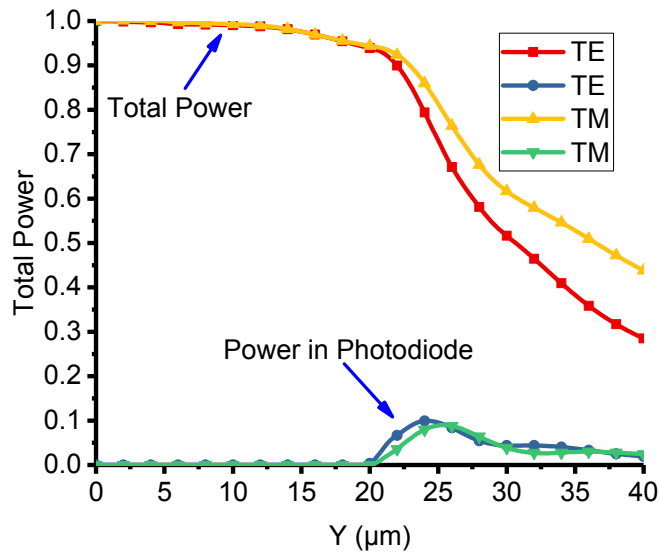
Figure 6-7 Optical power absorption for TE- and TM-Mode.

In Figure 6-6, the optical power distributions in *YZ*-plane for *TE*- and *TM*-Mode are

given. In Figure 6-7, the total power inside the EC-OSJ-WGPD and the power inside the

photodiode are given. The optical power distribution profiles shown in Figure 6-6 correspond well with the optical power absorption profiles given in Figure 6-7. From $y =$ 0 to 20 μm, the total power is almost constant, which indicates that the light propagates efficiently inside the diluted waveguide. From $y = 20$ to 40 μm, the total power drops gradually. The power in the photodiode increases at the beginning and then drops. This phenomenon indicates that the light is gradually coupled from the diluted waveguide to the photodiode and then absorbed by the photodiode. In the simulation, the scattering loss of the waveguide is not considered, and only a small portion of optical energy escapes from the waveguide structure, which is negligible.

As shown in Figures 6-6 and 6-7, the total power can be used to estimate the power absorbed by the photodiode. The total power at the end of the EC-OSJ-WGPD (y=40 μm) indicates the residual power. The more power absorbed by the photodiode, the lower the residual power at the end of the waveguide photodiode. The propagation and absorption of the TE and TM polarized light (Figures 6-6 and 6-7) vary with the change of parameters of the EC-OSJ-WGPD (Table 6-1). The design goal is to increase the absorption efficiency of TE and TM polarized light and minimize the discrepancy between them. It's found in the simulation that the thicknesses of the four coupling layers can change the absorption efficiency of TE and TM polarized light. Thus, the coupling layers should be designed carefully. Since the RSoft BeamProp software cannot calculate the photogeneration rate and photocurrent of the EC-OSJ-WGPD, a Multiphysics simulation methodology is introduced in the following section.

6.4 Multiphysics simulation
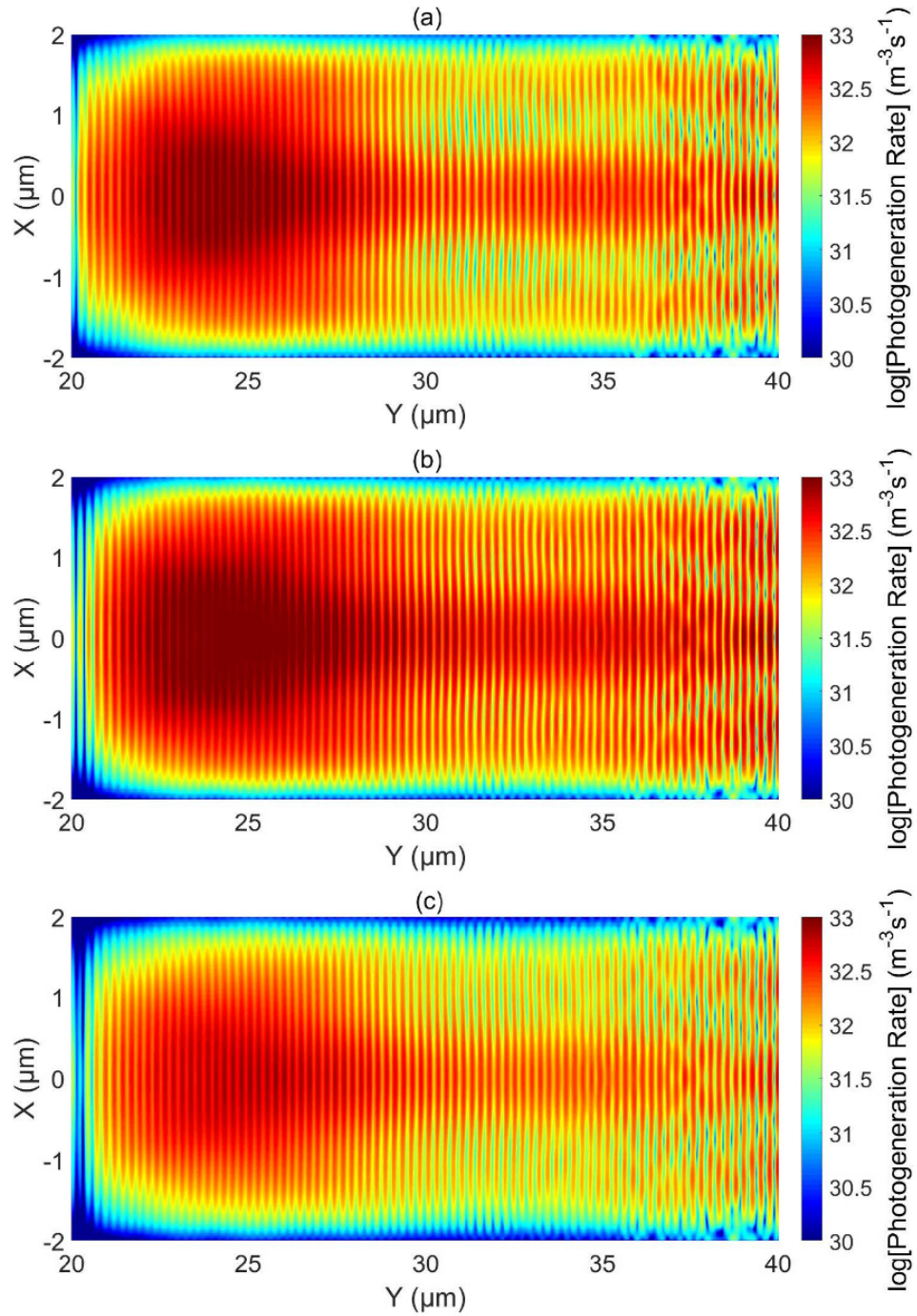
Figure 6-8 Photogeneration rate at (a) bottom, (b) middle, and (c) top of the absorption region with an injected light power of 1 mW in TE-Mode.
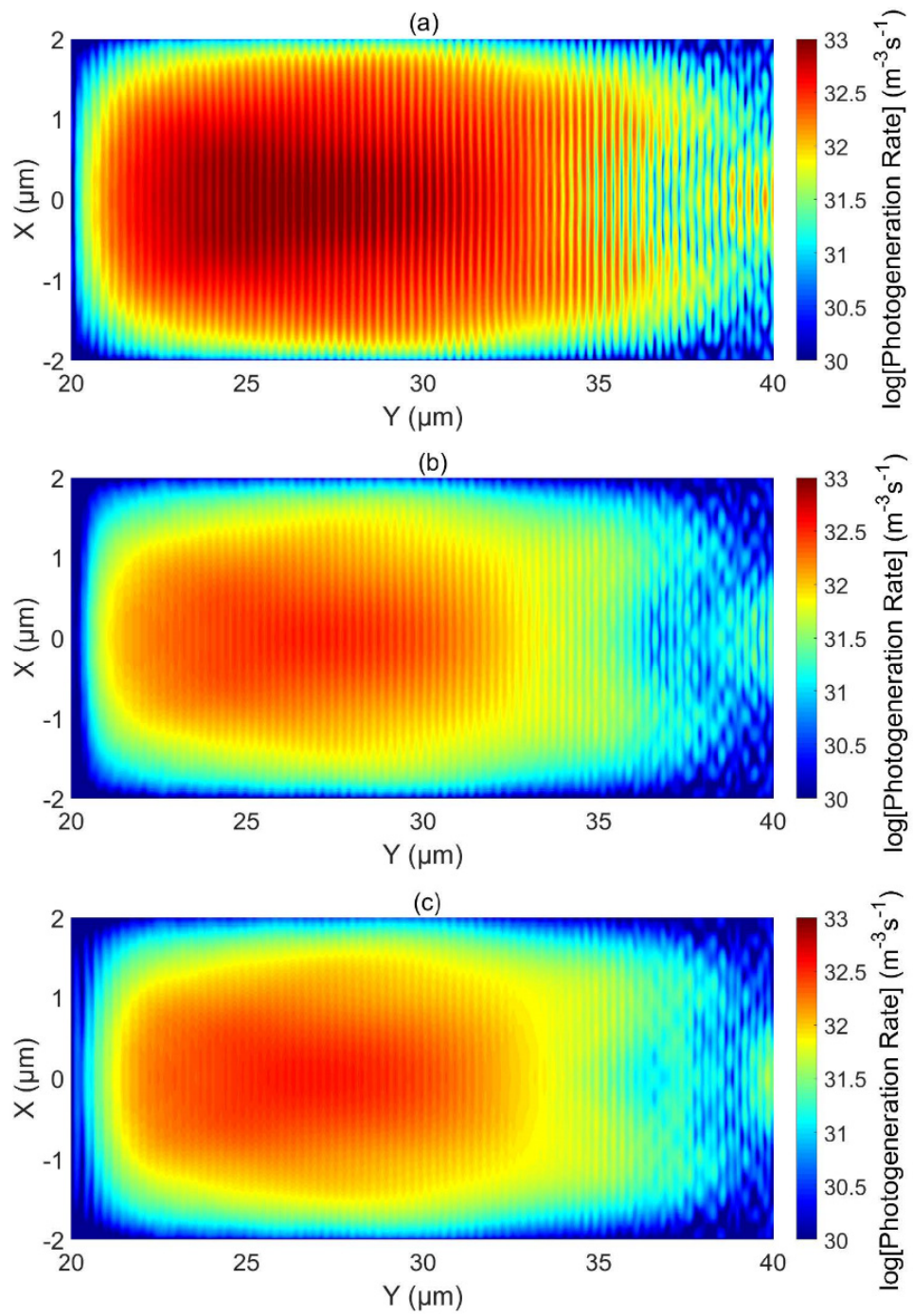
Figure 6-9 Photogeneration rate at the (a) bottom, (b) middle, and (c) top of the absorption region with an injected light power of 1 mW in TM-Mode.
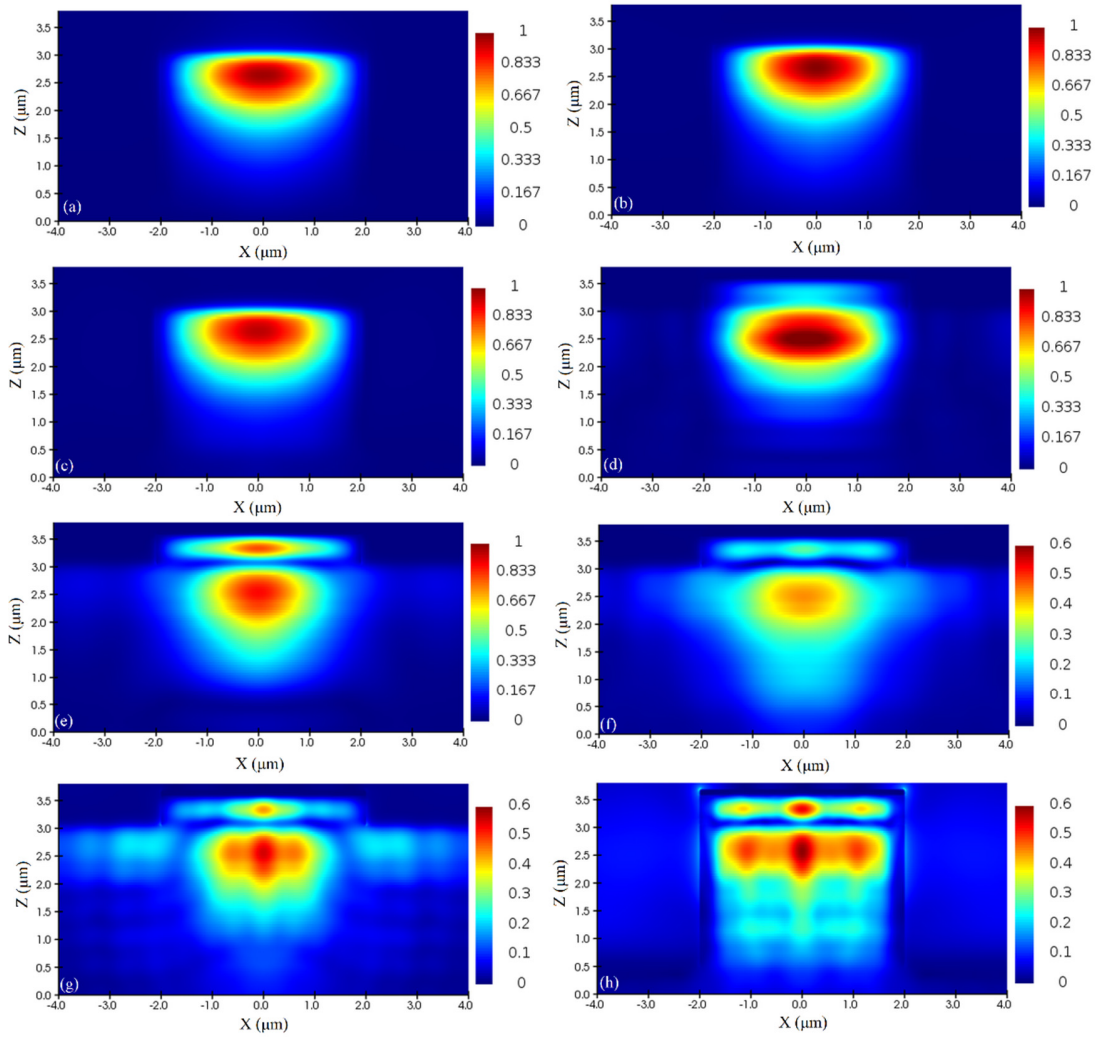
Figure 6-10 Optical power distribution at (a) y=0.1 μm, (b) y=10 μm, (c) y=16 μm, (d) y=21 μm, (e) y=26 μm, (f) y=30 μm, (g) y=35 μm, and (h) y=39 μm in TE-Mode.

The design of waveguide photodiode consists of two parts (optical component design and electrical component design), and it can be simulated using the combination of optical simulation and electrical simulation (Multiphysics simulation). The optical performance of the EC-OSJ-WGPD is simulated using Lumerical FDTD, and the photogeneration rate is calculated. Then the photogeneration rate is imported to Silvaco Atlas for the calculation of photocurrent. The absorption region of the EC-OSJ-WGPD has a thickness of 350 nm, and the cross-section views (*XY*-plane) of the photogeneration rate at the bottom, middle,

and top of the absorption region are given in Figures 6-8 and 6-9. In the Lumerical FDTD simulation, a power monitor is placed at y=0.1 μm to monitor the injected light power. At injected light power of 1 mW, the photogeneration rate is approximately between 1×10^{30} and 1×10^{33} $m^{-3}\cdot s^{-1}$. The photogeneration rate at the beginning of the photodiode is much higher than that at the end of the photodiode because most of the light is absorbed in the beginning part. The photogeneration rate in TE-mode is higher than that in TM-mode because more light is absorbed in TE-mode, as shown in Figures 6-6 and 6-7. The parameters used for TCAD simulation are given in Appendix B. The photogeneration rate is averaged along the Y-axis to obtain 2D photogeneration rate (XZ-plane). (Note: the coordinate systems in all Figures consistent with each other.)

6.5 Device characteristics

6.5.1 Internal optical power distribution

The internal optical power distribution is obtained by placing 8 power monitors along the Y-axis in the Lumerical FDTD simulation. The cross-section views of the internal optical power distribution of the EC-OSJ-WGPD in TE- and TM-mode are given in Figures 6-10 and 6-11, respectively. As shown in Figures 6-10 and 6-11, fundamental TE- and TM-mode are considered in the simulation. In the waveguide section (0 μm≤y≤20 μm), light propagates efficiently inside the diluted waveguide and coupling layers. In the photodiode section (20μm≤y≤40μm), light is gradually coupled from the diluted waveguide to the photodiode and then absorbed by the photodiode. At the end of the photodiode (y=39 μm), the residual optical power in TE- and TM-mode is low, which indicates that light has been absorbed
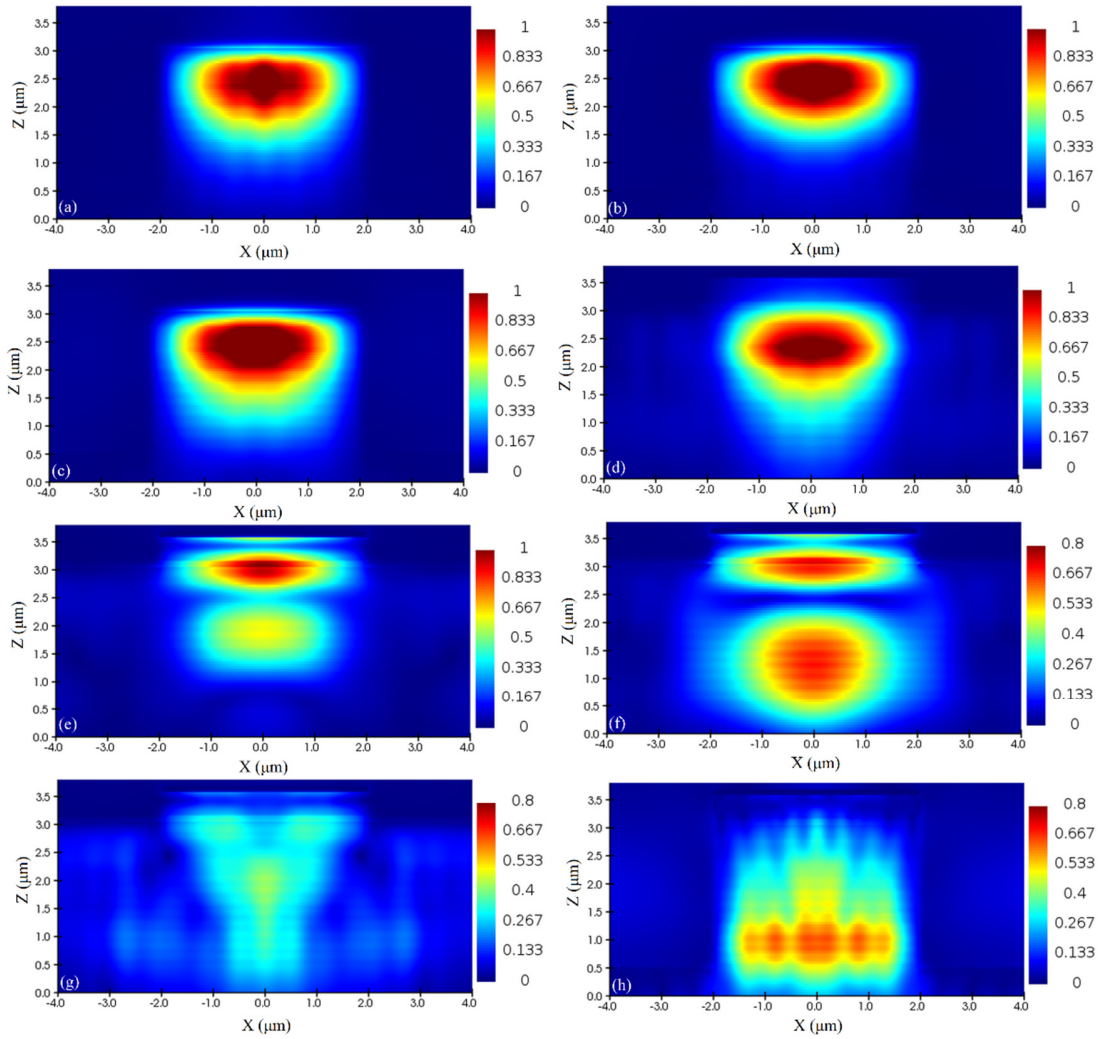
Figure 6-11 Optical power distribution at (a) y=0.1 μm, (b) y=10 μm, (c) y=16 μm, (d) y=21 μm, (e) y=26 μm, (f) y=30 μm, (g) y=35 μm, and (h) y=39 μm in TM-Mode.

by the photodiode efficiently. As shown in Figures 6-10 and 6-11, there is a difference in the propagation of TE- and TM-mode light inside the EC-OSJ-WGPD. Thus, the absorption efficiency for TE- and TM-mode light is different. It's worth mentioning that the photodiode, the coupling layers, and the diluted waveguide should be considered as a whole in the design of EC-OSJ-WGPD. The cross-section views in Figure 6-6 (*YZ*-plane) and Figures 6-10 and 6-11 (*XZ*-plane) show clearly the light propagation inside the

waveguide photodiode, which is helpful for the understanding of the operation mechanisms of the waveguide photodiode.

6.5.2 Internal electric field and energy band diagram of the EC-OSJ-WGPD
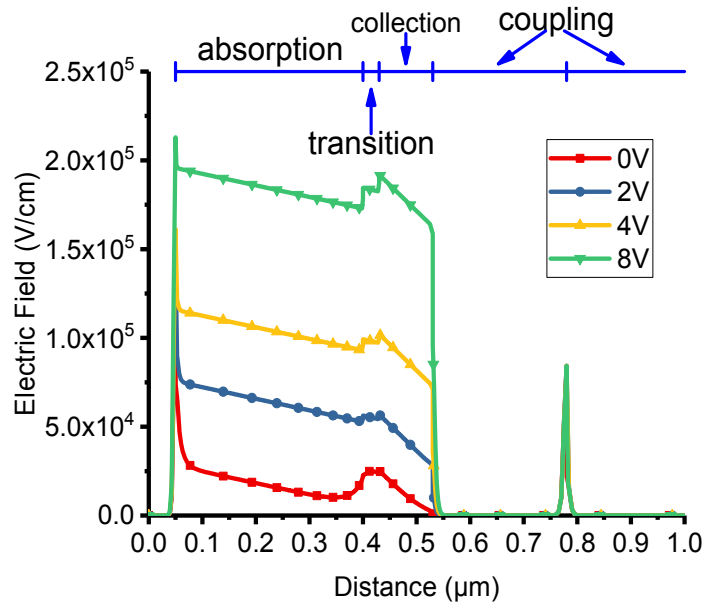
Figure 6-12 Internal electric field of the EC-OSJ-WGPD at different bias voltages.

The bias voltage has a significant influence on the photodiode's performance. In order to get high output power, bias voltage should always be applied. Since all layers (except contact layers) are depleted, and the depletion width is large, the EC-OSJ-WGPD can be biased at a high voltage without causing device breakdown. As shown in Figure 6-12, at a bias voltage of 8 V, the internal electric field is around 2×10^5 V/cm, which is below the breakdown electric field of 2.5×10^5 V/cm for InGaAs.

The energy band diagram of the EC-OSJ-WGPD is given in Figure 6-13. The conduction band energy and valence band energy drop smoothly in the absorption layer,

transition layers, and collection layer, which could facilitate the transportation of electrons and holes.
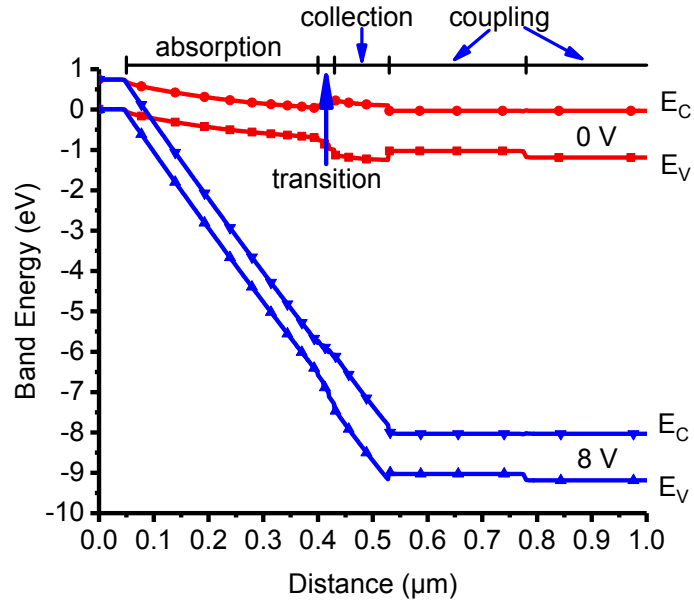
Figure 6-13 Energy band diagram of the EC-OSJ-WGPD at bias voltages of 0 and 8 V.

6.5.3 Frequency response of the EC-OSJ-WGPD
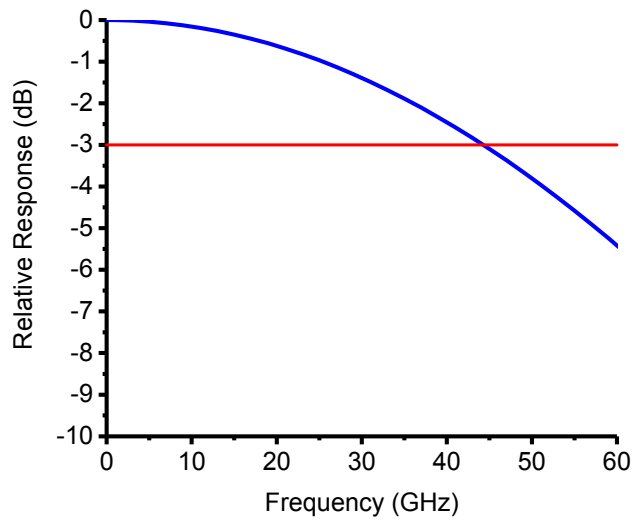
Figure 6-14 3-dB bandwidth of the EC-OSJ-WGPD.

In order to estimate the bandwidth of the EC-OSJ-WGPD, 2D TCAD simulation in Silvaco Atlas is used. The area of the photodiode and the load resistance are set to 80 μm^2 and 50 Ω, respectively. In the absorption layer, both electrons and holes travel at saturation velocity (2.5×10^7 cm/s for electrons and 5×10^6 cm/s for holes). Thanks to the shorter traveling distance of the holes, the slow-moving holes won't slow down the speed of the photodiode. As shown in Figure 6-14, the EC-OSJ-WGPD achieves a bandwidth of 44.5 GHz.

6.5.4 Output photocurrent
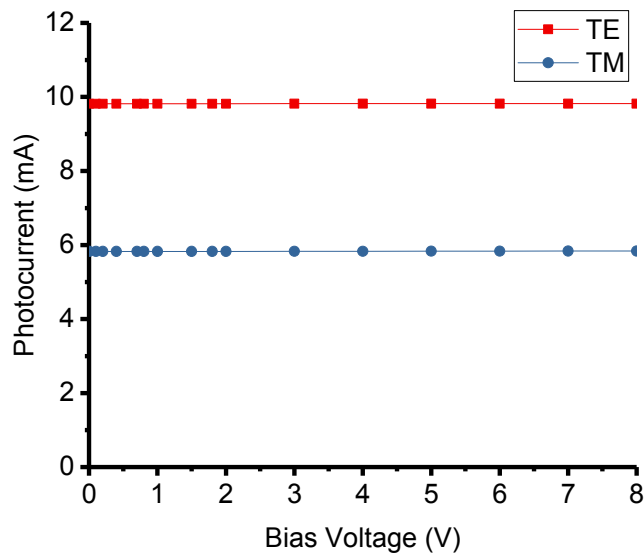
Figure 6-15 Output photocurrent of the EC-OSJ-WGPD with injected light power of 10 mW.

The output photocurrent is an essential figure of merit. Different from the topside illuminated and backside illuminated photodiode, the photocurrent generation inside the evanescently coupled waveguide photodiode is quite complicated. As shown in Figures 6-8 and 6-9, the photogeneration rate inside the absorption layer is nonuniform. Since the

photogenerated electron and hole pairs (EHPs) are nonuniform inside the photodiode, 3D TCAD simulation is needed. However, the 3D TCAD simulation is time-consuming and may encounter a convergence problem. Thus, the 3D photogeneration rate is averaged along the *Y*-axis to obtain 2D photogeneration rate (*XZ*-plane). Then, the 2D TCAD simulation is used to calculate the photocurrent. In theory, the photocurrent calculated by 2D and 3D TCAD simulation should be similar. The bias voltage and load resistance are set to 8 V and 50 Ω, respectively, for the photocurrent calculation. The simulated photocurrent of the EC-OSJ-WGPD with an injected optical power of 10 mW is given in Figure 6-15. The injected optical power in TE- and TM-mode is set to 10 mW, and the output photocurrents for TE- and TM-mode are 9.8 and 5.8 mA, respectively. The responsivity for TE- and TM-mode is 0.98 and 0.58 A/W, respectively. In order to get high responsivity (efficiency), the influence of the diluted waveguide, coupling layers, and photodiode should be considered in the design procedure. (Limitation: this modeling methodology cannot calculate the photocurrent at high optical power since the photocurrent might saturate at the beginning part, where the photogeneration rate is high.)

The methodology introduced above has been adopted to calculate the responsivity of the waveguide photodiode [104]. The waveguide photodiode with an absorption layer thickness of 500 nm and an area of 5×20 μm^2 achieves a simulated responsivity of 0.93 A/W, which is close to the measured responsivity of 1 A/W.

6.6 Conclusions

Waveguide photodiode can provide higher efficiency than surface illuminated photodiode because the traveling direction of light is perpendicular to the traveling

direction of electrons and holes. This feature makes the carrier transit time limited bandwidth and the absorption efficiency quasi-independent of each other. In this chapter, an EC-OSJ-WGPD has been designed and analyzed. The 3D structure and epitaxial layer structure have been given. The 3D BPM simulation has shown that the designed waveguide photodiode absorbs TE and TM polarized light efficiently. To achieve a balanced absorption and high sensitivity (efficiency), the diluted waveguide, the coupling layers, and the photodiode should be considered as a whole in the design procedure. To estimate the performance of EC-OSJ-WGPD, a simple numerical modeling procedure has been proposed. The Multiphysics simulation method can be an effective way to predict the performance of similar waveguide photodiode before the complicated and expensive nanofabrication process. The designed EC-OSJ-WGPD has a bandwidth of 44.5 GHz (without considering the external circuit) and achieves a responsivity of 0.98 A/W. The proposed EC-OSJ-WGPD structure can be used for applications in high-speed fiber-optic communication systems, radio-over-fiber wireless communication systems, and THz and MMW generation schemes.

Chapter 7 Equivalent Circuit Model of InGaAs/InP Photodiodes

7.1 Introduction

Technology Computer-Aided Design (TCAD) refers to the use of computer simulation to model semiconductor devices' fabrication process and their operation. The TCAD process and device simulation tools support a broad range of applications, such as CMOS, power devices, memory, image sensors, solar cells, etc. As discussed in Chapter 3, TCAD software solves fundamental physical partial differential equations, such as diffusion and transport equations, to model the structural properties and electrical behavior of semiconductor devices. This physics-based methodology gives TCAD simulation excellent predicting capability for a broad range of technologies. Therefore, TCAD simulations are used to reduce the costly and time-consuming test wafer runs when developing and characterizing a new semiconductor device or technology.

However, the performance of InGaAs/InP photodiode is not only determined by the device itself but also by the external microwave circuit. As discussed in section 5.3, there is always a discrepancy between TCAD simulation and measurements [81]. To overcome the drawback and improve the accuracy during the numerical modelling process, the equivalent circuit model, which combines the TCAD and microwave circuit simulation, is adopted to analyze the frequency response of InGaAs/InP photodiode. Firstly, the methodology is investigated and verified by comparing the simulated results with the experimental results. Then, the methodology is used to analyze the frequency response of

OSJ-PD, MOSJ-PD, and EC-OSJ-WGPD. Finally, a discussion and summary of the equivalent circuit model are given.

7.2 Methodology investigation

The frequency analysis methodology using an equivalent circuit model introduced in this chapter is unique since it combines the simulated results obtained from TCAD and Advanced Design System (ADS) simulation. The TCAD simulation considers the semiconductor device itself, and the ADS simulation considers the external microwave circuit. By combining them together, the accuracy of frequency response analysis can be significantly improved. As a result, the equivalent circuit model can be used to predict the frequency response of InGaAs/InP photodiode when high accuracy is required.
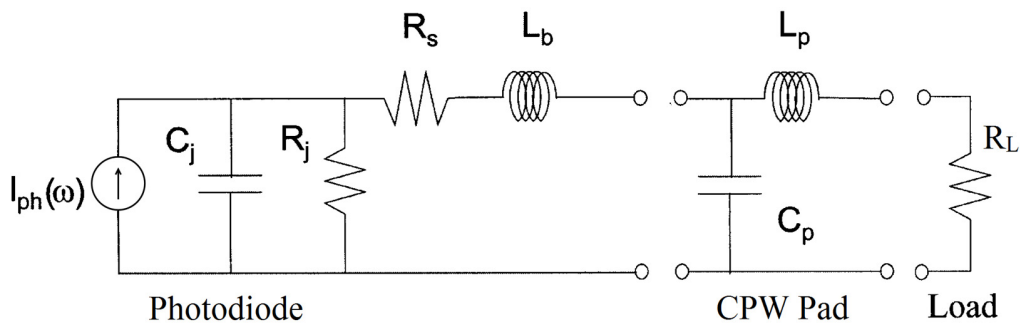
Figure 7-1Basic equivalent circuit model of the InGaAs/InP photodiode.

The basic equivalent circuit model of the InGaAs/InP photodiode is given in Figure 7-1. The photocurrent source $I_{ph}(\omega)$, junction capacitance C_j and junction resistance R_j represent the photodiode itself. The series resistance R_s, air bridge inductance L_b, coplanar pad capacitance C_p, coplanar pad inductance L_p, and load resistance R_L represent the external circuit. The photodiode is always reverse biased or zero biased during operation. C_j can be calculated by the equation of a parallel capacitor (Appendix C), and R_j has a

large value (>100 kΩ). R_s is due to the ohmic contact resistance and bulk resistance induced by the metallic connection. L_b is determined by the geometry of the air bridge. C_p and L_p are determined by the characteristic impedance $Z_c = \sqrt{L_p/C_p}$ of the CPW pad. R_L is usually set to 50 Ω.

The equivalent circuit model is used in earlier works [45,78,82,92,94,114-120] to understand the operation mechanism and analyze the frequency response of a photodiode. In these works, the parameters of the equivalent circuit model are extracted from the measured S_{11} data, which demonstrates high reliability. However, the transit time limited bandwidth cannot be measured, and it plays an important role in the frequency response. In previous works, the transit time (τ_e and τ_h) is usually obtained from the empirical model [121], and the frequency response can be calculated by [94]

$$
\begin{aligned}
I_L(\omega) &= \frac{I_{ph}(\omega)}{1+\frac{R_S+R_L}{R_j}-C_jL_b\omega^2+j\omega(\frac{L_b}{R_j}+C_j(R_S+R_L))} \\
&= \frac{\left[\frac{1}{j\omega\tau_e}\left(1-\frac{1-\exp(-j\omega\tau_e)}{j\omega\tau_e}\right)+\frac{1}{j\omega\tau_h}\left(1-\frac{1-\exp(-j\omega\tau_h)}{j\omega\tau_h}\right)\right]\exp(j\omega t)}{1+\frac{R_S+R_L}{R_j}-C_jL_b\omega^2+j\omega\left(\frac{L_b}{R_j}+C_j(R_S+R_L)\right)}I(0)
\end{aligned}
\tag{7.1}
$$

Assuming that *I(0)* is the dc photocurrent (equal to the responsivity–optical power product *R·P$_{opt}$*), *I$_{ph}$(ω)* is the ac photocurrent, and *I$_L$(ω)* is the current flowing through the load.
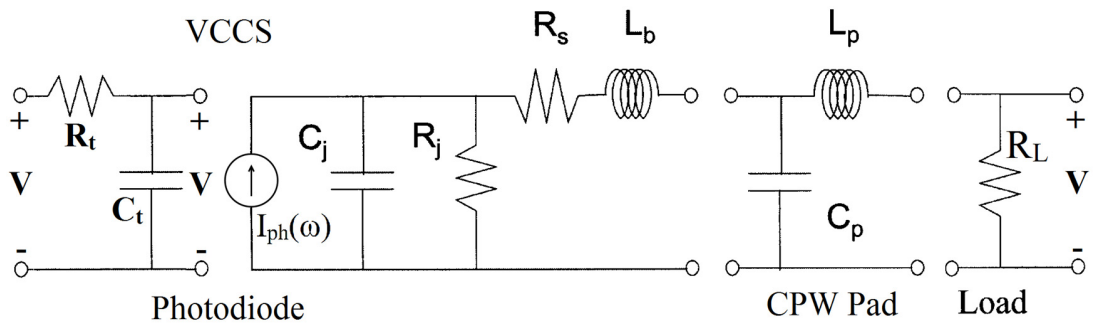
Figure 7-2 Improved equivalent circuit model of the InGaAs/InP photodiode.

The improved equivalent circuit model is given in Figure 7-2. The photocurrent source $I_{ph}(\omega)$ in Figure 7-1 is replaced by a Voltage Controlled Current Source (VCCS) in Figure 7-2. The frequency response of the VCCS is determined by the carrier transit time τ_{tr}, which can be calculated by $\tau_{tr} = R_t \cdot C_t$ (Note: R_t and C_t are used to represent the transit time and have no physical meaning.). Similar to Equation (7.1), the frequency response of the improved equivalent circuit model is given by

$$I_L(\omega) = I_{ph}(\omega) \cdot H(\omega) = I(0) \cdot \frac{1}{1+j\omega R_t C_t} \cdot H(\omega) = I(0) \cdot \frac{1}{1+j\omega R_t C_t} \cdot \frac{R_j}{A+j\cdot B} \quad (7.2)$$

where $I_{ph}(\omega)$ is the ac photocurrent; $H(\omega)$ is the transfer function of the circuit; $I(0)$ is the dc photocurrent; A and B are given by

$$A = R_j + R_s + R_L - \omega^2\left(C_jL_bR_j + C_pL_pR_j + C_pL_pR_s + C_pL_bR_L + C_jL_pR_j + C_jC_pR_jR_LR_s\right)$$
$$+ \omega^4 C_jC_pL_bL_pR_j$$

$$B = \omega\left(L_b + L_p + C_jR_jR_s + C_pR_LR_j + C_pR_LR_s + C_jR_jR_L\right) - \omega^3\left(C_pL_bL_p + C_jC_pL_pR_jR_s\right.$$
$$\left. + C_jC_pL_bR_jR_L\right)$$

The bandwidth of the ac photocurrent $I_{ph}(\omega)$ is $f_{3dB} = \frac{1}{2\pi\tau_{tr}} = \frac{1}{2\pi R_t C_t}$, which is determined by the transit time. Obviously, the overall frequency response of the circuit model shown in Figure 7-2 is determined by the transit time τ_{tr}, junction capacitance C_j, junction resistance R_j, and other parameters of the external circuit.

A similar circuit model has been used in previous works [78,117,118] to study the frequency response of a photodiode. And all the parameters of the equivalent circuit model are obtained from measured S_{11} data and frequency response using data fitting [118]. In the following discussions, a unique analysis methodology using an equivalent circuit model is investigated. The parameters (R_t, C_t, C_j, and R_j), which are used to represent the photodiode, can be obtained from TCAD simulation. Then, these parameters (R_t, C_t, C_j,

and R_j) are combined with other parameters (R_s, L_b, C_p, and L_p) to analyze the frequency response of a photodiode. The advantage of this methodology is the capability to predict the frequency response of a new device structure based on the TCAD simulation and the equivalent circuit model.

7.3 Methodology verification

7.3.1 Equivalent circuit model of the waveguide photodiode
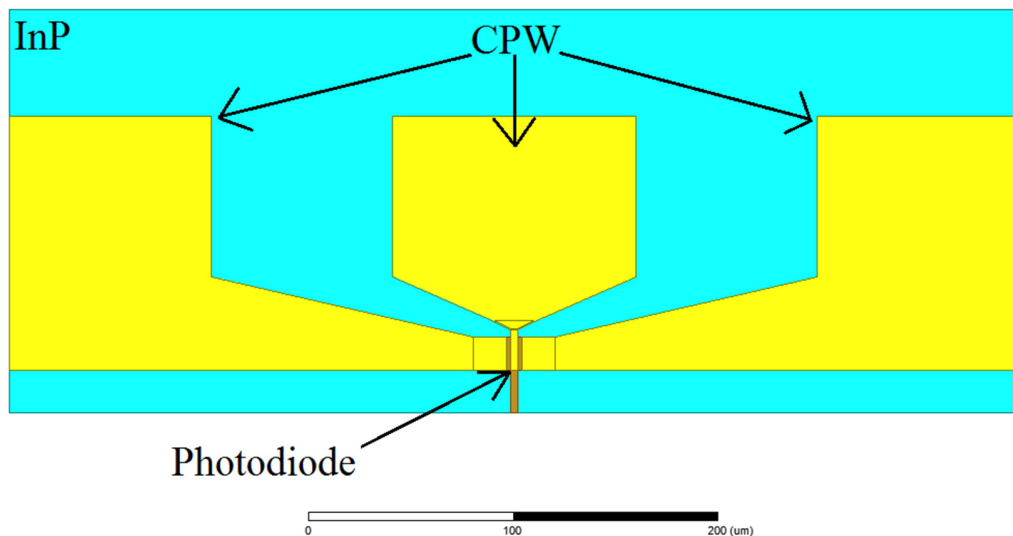
Figure 7-3 Structure of the waveguide photodiode chip.

The structure of a waveguide photodiode chip is shown in Figure 7-3. In Silvaco Atlas TCAD simulation, only the photodiode is considered (Figure 6-4), while in equivalent circuit model simulation, both the photodiode and the CPW pad are included (Figures 7-3 and 7-4). The equivalent circuit model of the waveguide photodiode [94] obtained using data fitting (Circuit Model A) is given in Figure 7-4. The parameters (R_j, C_j, R_s, L_b, C_p, and L_p) are determined by choosing the most appropriate values that make the simulated impedance well fits the measured impedance [94]. Then, the transit time is determined by

choosing appropriate values of C_t and R_t to make the simulated frequency response close to the measured frequency response. As shown in Figure 7-5, the simulated frequency response achieves a bandwidth of 40 GHz, which is close to the measured bandwidth of 45 GHz (bias voltage is 3 V) [94]. The discrepancy is mainly due to the overestimated value of C_j given in [94]. (Note: the calculated C_j is 32.8 fF, while the fitted C_j is 46 fF.) The transit time (C_t and R_t) limited bandwidth is 58 GHz. The bandwidth simulated by TCAD (the area and load resistance are set to 80 μm² and 50 Ω, respectively) is 32 GHz.
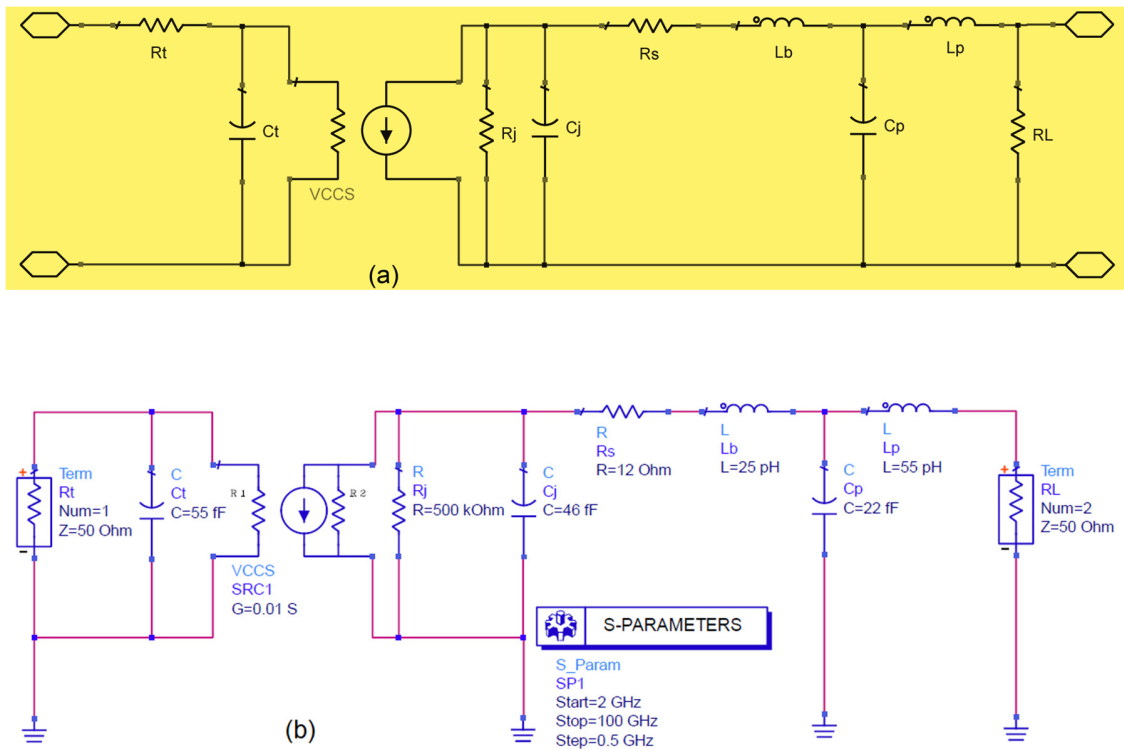
Figure 7-4 Equivalent circuit model of the waveguide photodiode (Circuit Model A): (a) circuit diagram (Note: the circuit is derived from [94]) and (b) ADS schematic diagram.
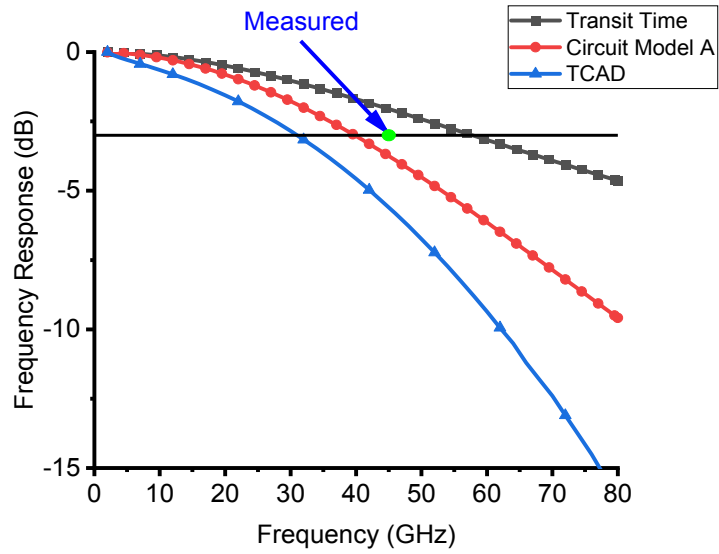
Figure 7-5 Simulated frequency response of the waveguide photodiode using Circuit Model A (Note: measured data obtained from [94]).
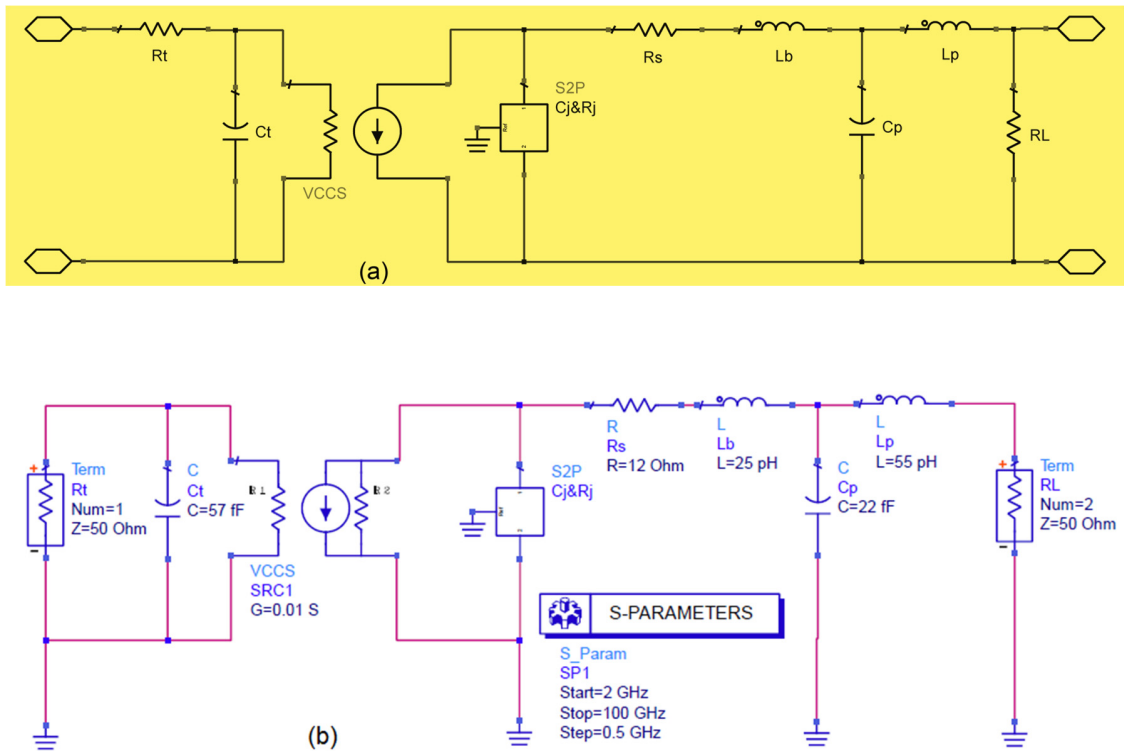
Figure 7-6 Equivalent circuit model of the waveguide photodiode (Circuit Model B): (a) circuit diagram (Note: the circuit is derived from [94]) and (b) ADS schematic diagram.

The S-parameters of the semiconductor device contain information about the device's electrical behavior and can be calculated using Silvaco Atlas [122]. Based on the equivalent circuit model given in Figure 7-4, a unique equivalent circuit model (Circuit Model B) is proposed and is given in Figure 7-6. The main differences between Circuit Model A and B are the parameters (R_t, C_t, C_j, and R_j), which are used to represent the photodiode. In Circuit Model A, R_t, C_t, C_j, and R_j are obtained using data fitting. In Circuit Model B, R_t, C_t, C_j, and R_j are calculated using Silvaco Atlas TCAD simulation. The C_j and R_j are extracted from TCAD simulation and then imported into ADS as an S2P component ($C_j\&R_j$). The extracted C_j and R_j are given in Figures 7-7 and 7-8. Both C_j and R_j are frequency dependent, and this phenomenon is discussed in Section 7.3.3. The junction resistance is approximately 200 kΩ (at 1 GHz), which is close to the fitted value of 500 kΩ in [94]. The junction capacitance is approximately 32 fF (at 1 GHz), which is close to the value calculated using the parallel capacitor formula.
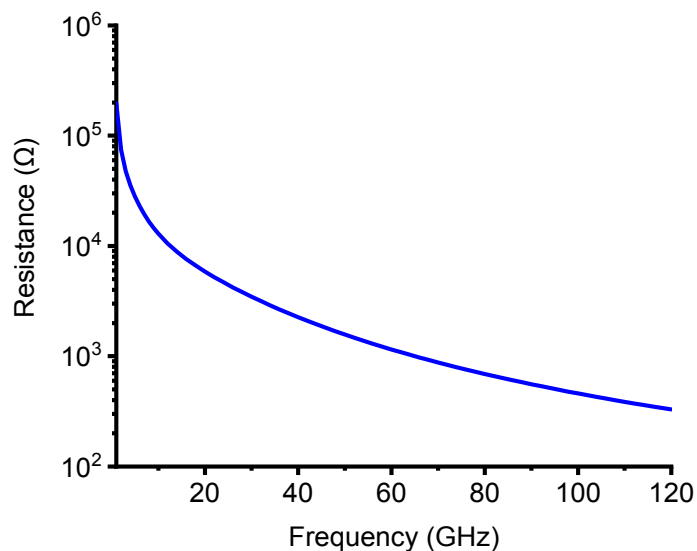
Figure 7-7 Extracted R_j of waveguide photodiode from TCAD simulation.
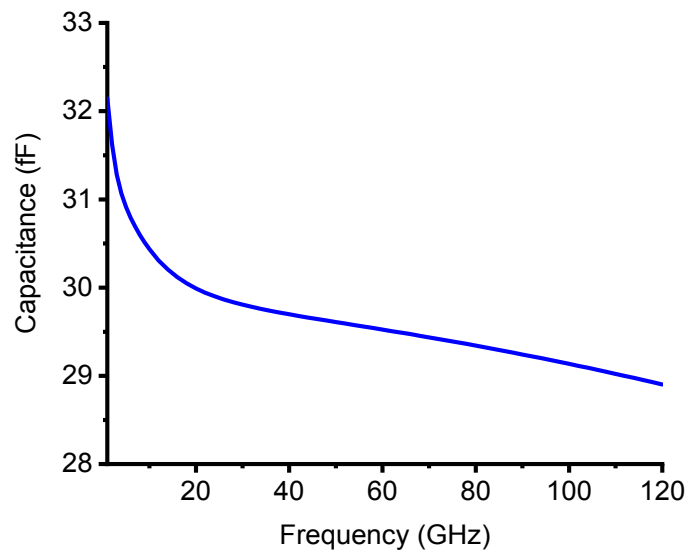
Figure 7-8 Extracted C_j of waveguide photodiode from TCAD simulation.
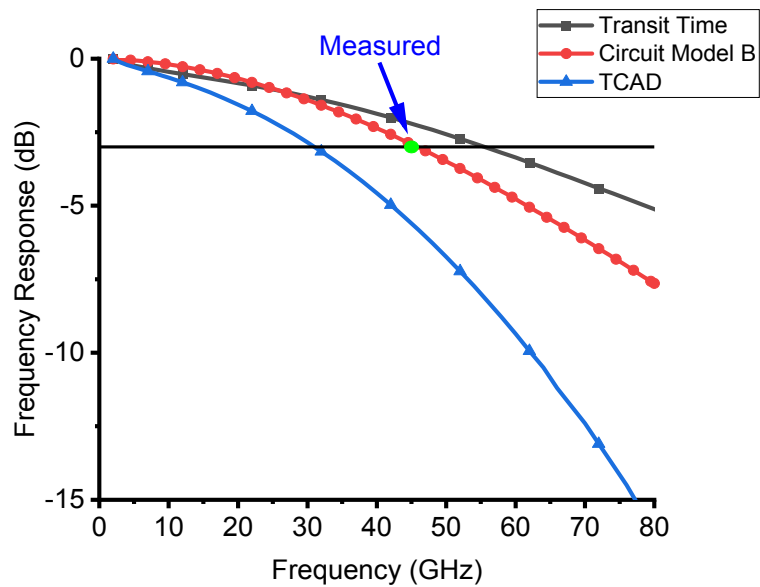
Figure 7-9 Simulated frequency response of the waveguide photodiode using Circuit Model B (Note: measured data obtained from [94]).

As shown in Figure 7-9, the simulated frequency response achieves a bandwidth of 46 GHz, which agrees well with the measured bandwidth of 45 GHz (bias voltage is 3 V)

[94]. In Circuit Model B, the transit time (R_t and C_t) is calculated by setting the load RESISTANCE to 0 in Silvaco Atlas. The bandwidth simulated by Silvaco Atlas TCAD is only 32 GHz, which is much lower than the measured bandwidth of 45 GHz [94]. As shown in Figures 7-5 and 7-9, the frequency responses simulated by the equivalent circuit model (Circuit Model A and B) demonstrate higher accuracy than the results simulated by TCAD only. This is mainly due to the influence of the CPW Pad. In the TCAD simulation, only the photodiode itself has been considered (Figure 6-4). In the equivalent circuit model (Circuit Model A and B), both the photodiode and the CPW Pad have been considered (Figure 7-3). Thus, the simulated frequency response using the equivalent circuit model is more accurate than the TCAD simulation only when compared with measurement.

7.3.2 Equivalent circuit model of the MUTC-PD
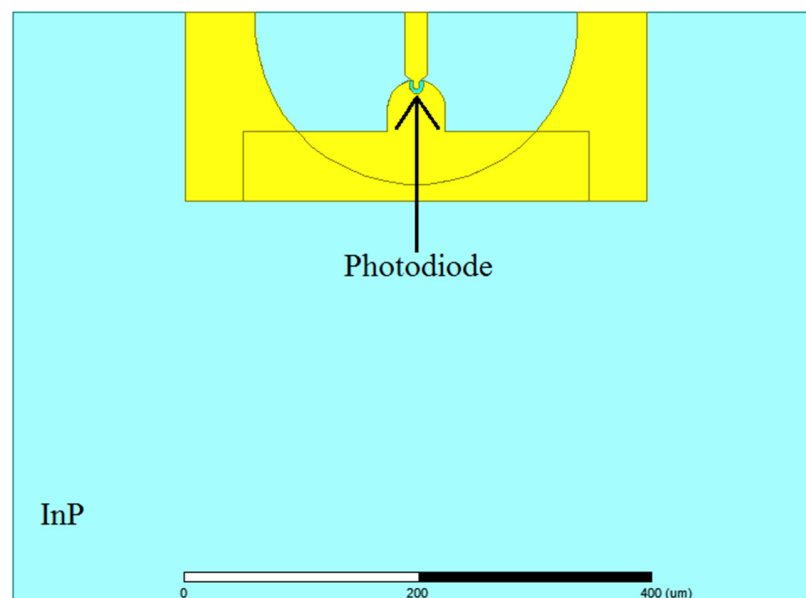
Figure 7-10 The PD die of the MUTC-PD before flip-chip bonding.

The PD die and the CPW Pad on the AlN substrate of the MUTC-PD [78] before flip-chip bonding are shown in Figures 7-10 and 7-11. The diameter of the photodiode is 5 μm. The CPW Pad is deposited on the AlN substrate, which has a thickness of 400 μm. The CPW Pad consists of a narrow section and a wide section. The narrow section has a characteristic impedance of 96 Ω and is connected to the photodiode. The wide section has a characteristic impedance of 50 Ω and is connected to the microwave probe for measurement. The detailed discussion about the fabrication of the MUTC-PD can be found in [78].
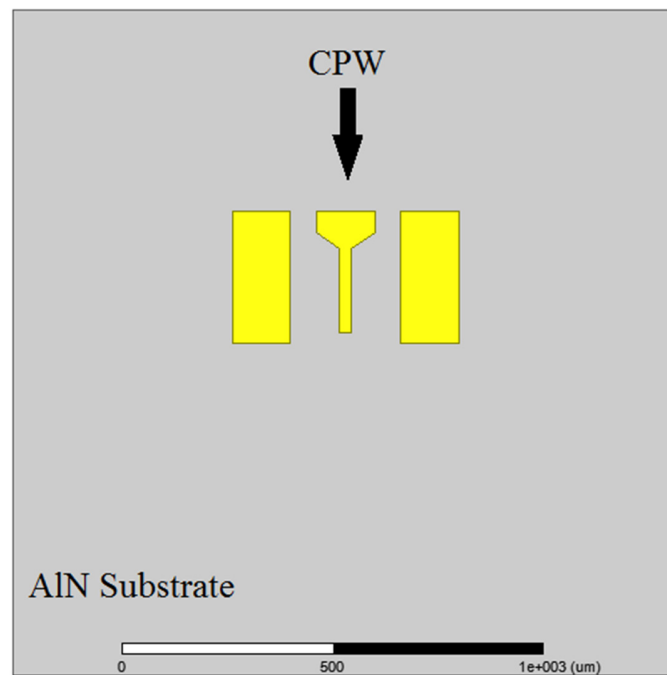
Figure 7-11 The CPW Pad of the MUTC-PD before flip-chip bonding.

The top view and 3D view of the MUTC-PD after flip-chip bonding are given in Figures 7-12 and 7-13. The photodiode with 5 μm diameter is connected to the feed line of the CPW Pad through an air bridge. The blue material represents InP, and the grey material represents AlN.
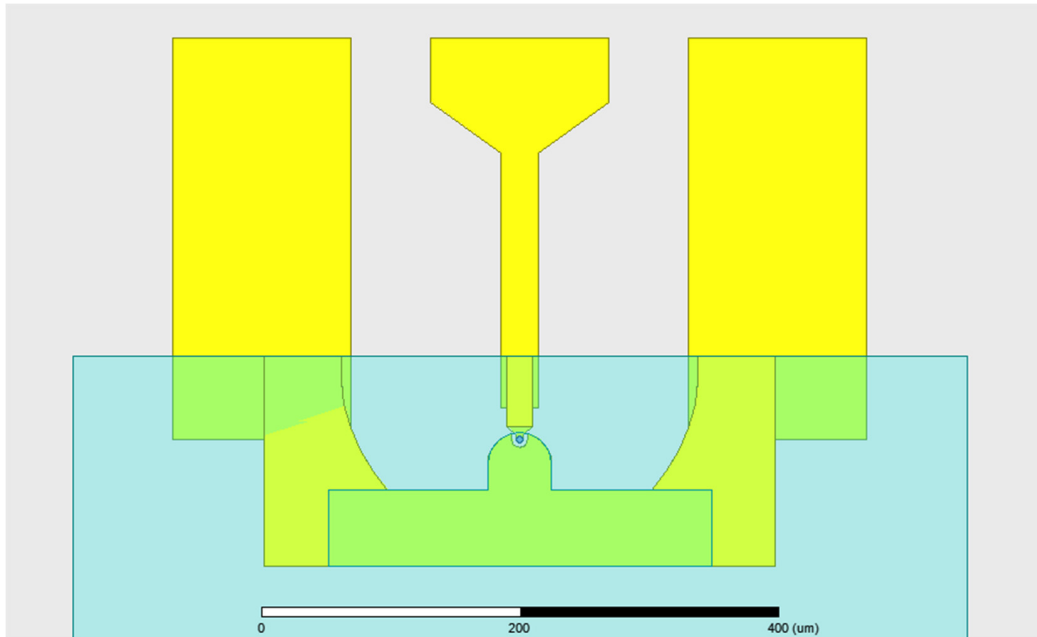
Figure 7-12 Top view of the MUTC-PD after flip-chip bonding.
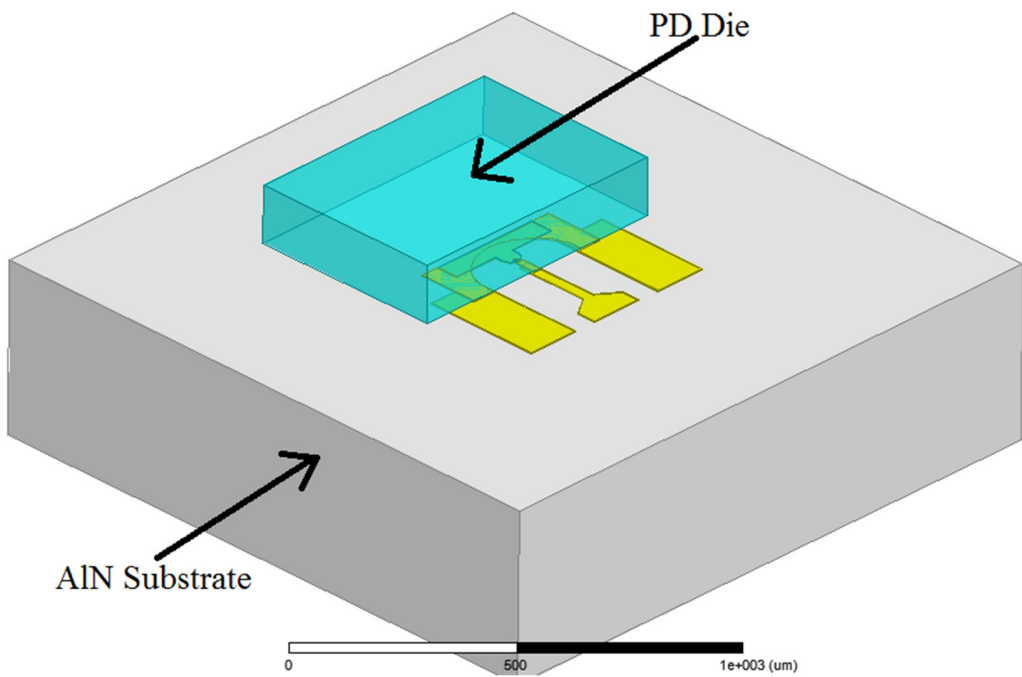
Figure 7-13 3D view of the MUTC-PD after flip-chip bonding.
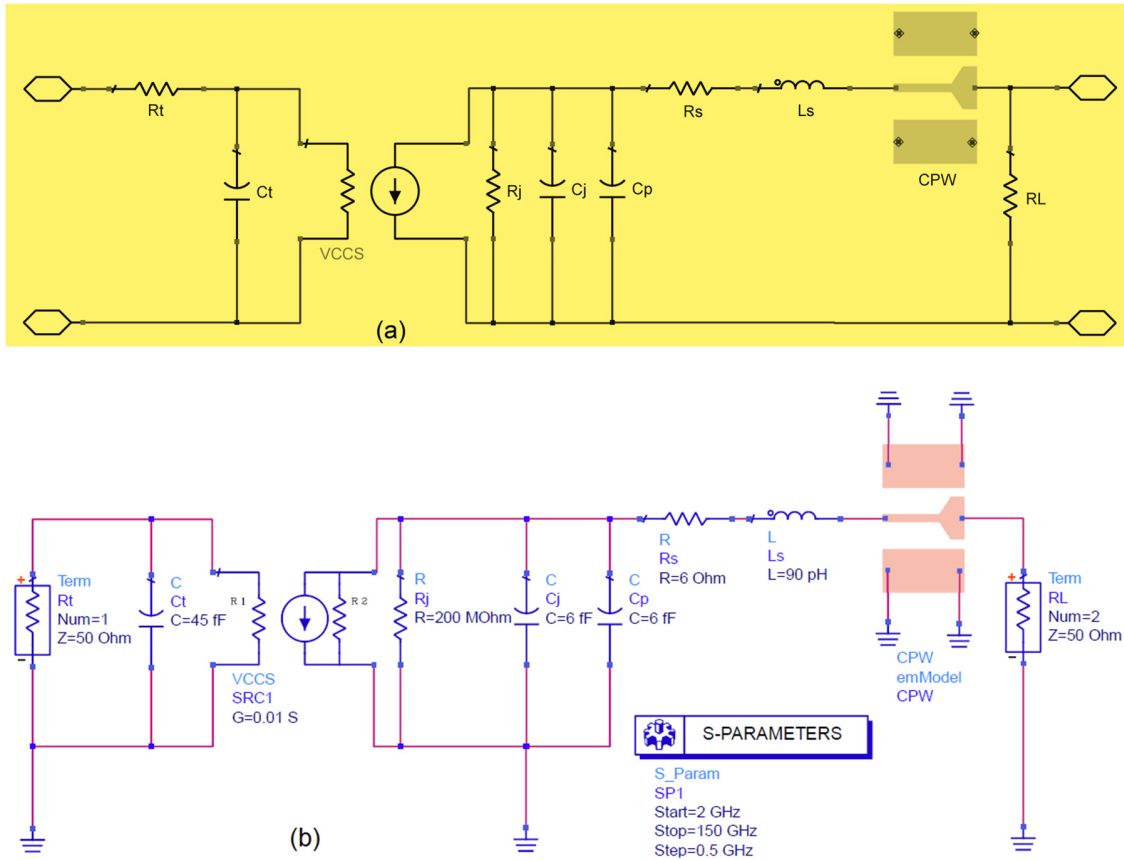
Figure 7-14 Equivalent circuit model of the MUTC-PD with a diameter of 5 μm (Circuit Model A): (a) circuit diagram and (b) ADS schematic diagram.

The equivalent circuit model (Circuit Model A) of the MUTC-PD with a diameter of 5 μm after flip-chip bonding is given in Figure 7-14. C_p represents the parasitic capacitance, and L_s represents the series inductance induced by the air bridge and the thin metal connecting the photodiode and the feed line of the CPW Pad. In order to improve the frequency response of the MUTC-PD [78], the CPW Pad has been specifically designed. The narrow section has a characteristic impedance of 96 Ω and behaves like an inductor. To include the effect of the CPW Pad, ADS EM/Circuit Co-simulation has been adopted. In conventional EM solvers, discrete components such as *R, L,* and *C* cannot be simulated directly. Hence, Co-simulation is used to integrate the CPW Pad simulated by EM solver

(Momentum/FEM simulation) with those discrete components in Schematic simulation [123]. And ADS EM/Circuit Co-simulation has demonstrated high accuracy in microwave circuit design [124]. The geometry of the CPW pad adopted in ADS EM/Circuit Co-simulation is given in Appendix D.
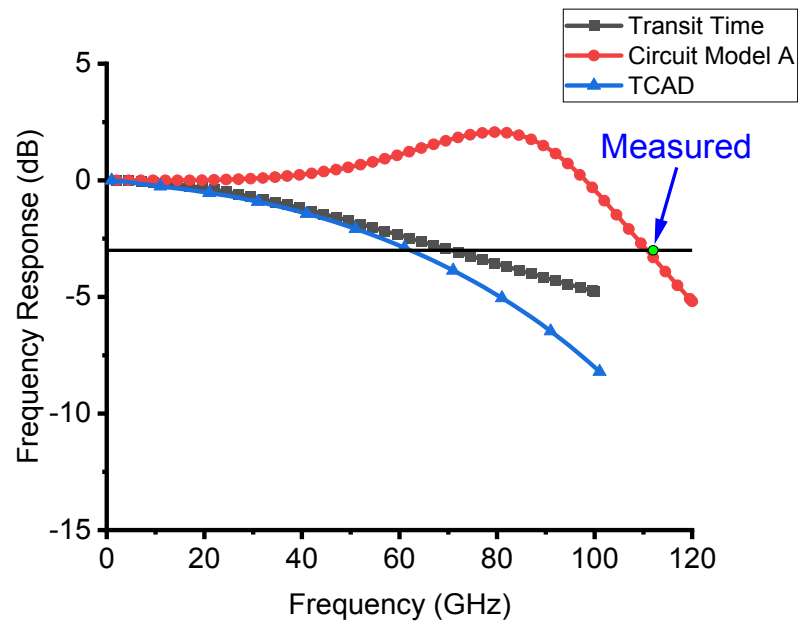
Figure 7-15 Simulated frequency response of the MUTC-PD with a diameter of 5 μm using Circuit Model A (Note: measured data obtained from [78]).

As shown in Figure 7-15, the simulated frequency response using Circuit Model A achieves a bandwidth of 111 GHz, which is close to the measured bandwidth of 112 GHz [78]. The transit time (C_t and R_t) limited bandwidth is determined by choosing appropriate values of C_t and R_t to make the simulated frequency response match the measured frequency response. And the estimated transit time limited bandwidth is 70.5 GHz. The bandwidth simulated by TCAD (the area and load resistance are set to 20 μm^2 and 50 Ω, respectively) is 63 GHz.
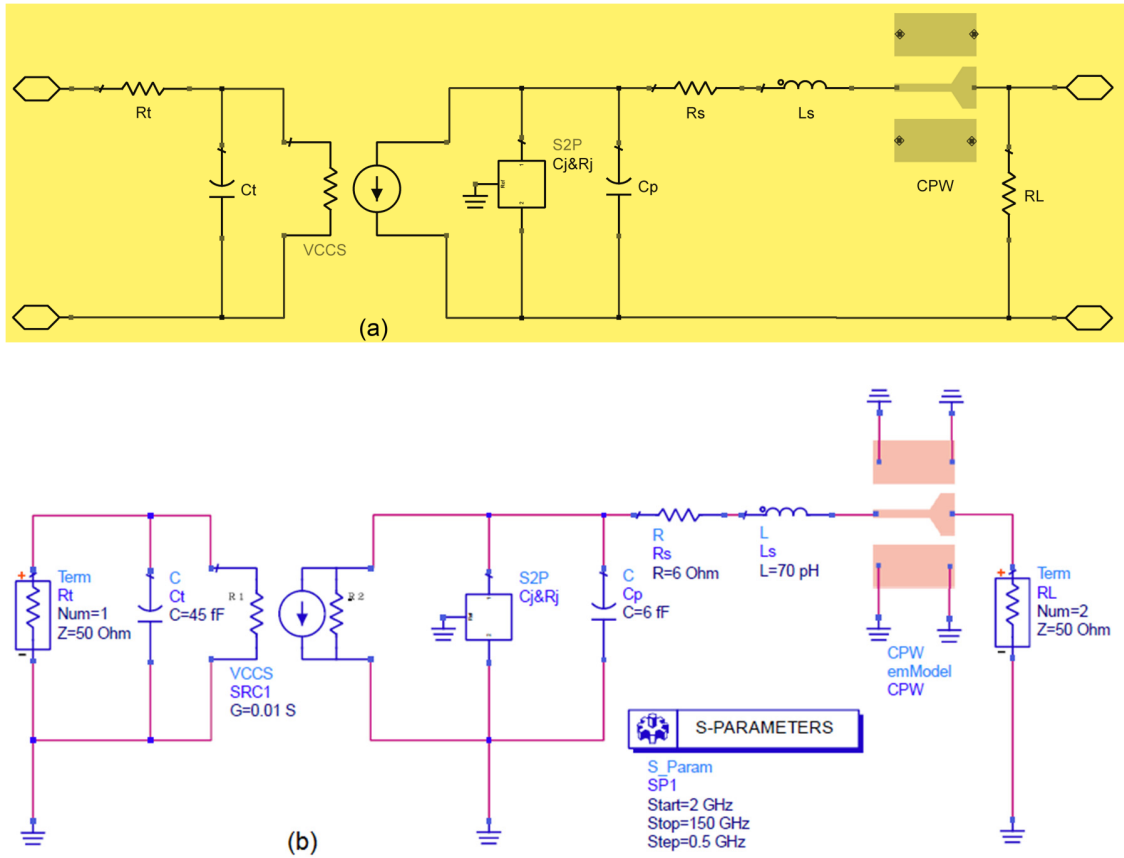
Figure 7-16 Equivalent circuit model of the MUTC-PD with a diameter of 5 μm (Circuit Model B): (a) circuit diagram and (b) ADS schematic diagram.

Based on the equivalent circuit model given in Figure 7-14, a unique equivalent circuit model (Circuit Model B) is proposed and is given in Figure 7-16. In Circuit Model B, R_t and C_t are calculated using Silvaco Atlas TCAD simulation. The C_j and R_j are extracted from TCAD simulation and then imported into ADS as an S2P component (C_j&R_j).

As shown in Figure 7-17, the simulated frequency response using Circuit Model B achieves a bandwidth of 113 GHz, which agrees well with the measured bandwidth of 112 GHz. In Circuit Model B, the transit time (R_t and C_t) is calculated by setting the load

RESISTANCE to 0 in Silvaco Atlas. The bandwidth simulated by Silvaco Atlas TCAD is only 63 GHz, which is much lower than the measured bandwidth of 112 GHz [78].
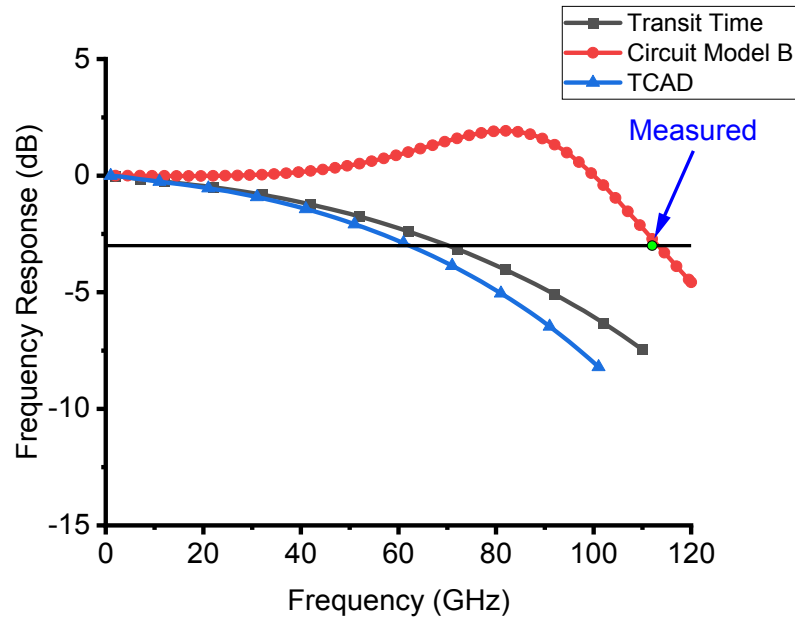
Figure 7-17 Simulated frequency response of the MUTC-PD with a diameter of 5 μm using Circuit Model B (Note: measured data obtained from [78]).

As shown in Figures 7-15 and 7-17, the frequency responses simulated by the equivalent circuit model (Circuit Model A and B) demonstrate higher reliability than the results simulated by TCAD only. This is mainly due to the external circuit (CPW Pad), which cannot be included in the TCAD simulation. It's worth mentioning that the TCAD simulation is still an important methodology for the initial design and simulation of the InGaAs/InP photodiode, even though it cannot include the influence of the external circuit connected to the photodiode. (Note: the frequency response of a photodiode is usually given by the relative response, which indicates that the response at high frequency is normalized to the response at the lowest frequency; as shown in Figures 7-15 and 7-17, the bandwidth of the flip-chip bonded MUTC-PD is higher than the transit time limited

bandwidth, which is mainly due to the specially designed CPW pad that improves the

impedance matching between the load and source at around 80 GHz.)
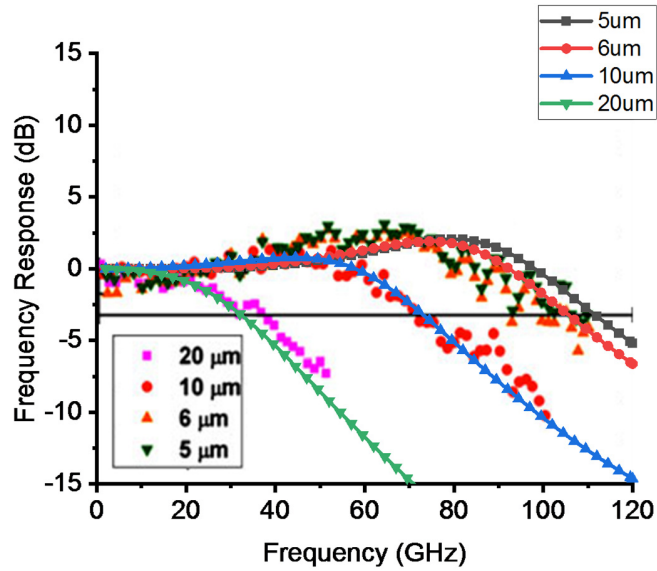
Figure 7-18 Frequency response of the MUTC-PDs with different diameters. (Scatter plot: measured data obtained from [78]; Line+Symbol plot: Simulation using Circuit Model A.)
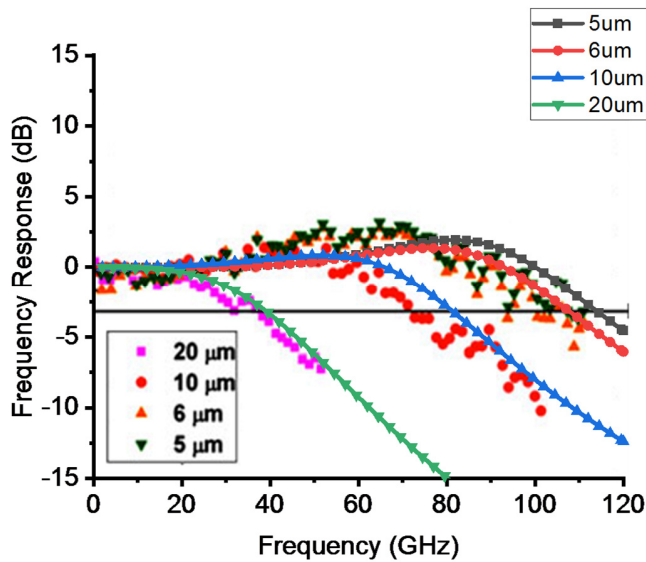
Figure 7-19 Frequency response of the MUTC-PDs with different diameters. (Scatter plot: measured data obtained from [78]; Line+Symbol plot: Simulation using Circuit Model B.)

To further verify the equivalent circuit model (Circuit Model A and B), the MUTC-PD with different diameters are analyzed. The simulated frequency response of the MUTC-PD with different diameters using Circuit Model A and B are given in Figures 7-18 and 7-19. The simulated results are superpositioned over the measured results [78] for comparison. The parameters of the equivalent circuit model vary with the diameter of the photodiode and are given in Tables 7-1 and 7-2. The extracted C_j and R_j of the MUTC-PDs (Circuit Model B) with different diameters are given in Figures 7-20 and 7-21. Both C_j and R_j are frequency dependent, and this phenomenon is discussed in Section 7.3.3. The junction resistance (diameter is 5 µm) is approximately 400 MΩ (at 0.1 GHz), which is close to the fitted value of 200 MΩ in [78]. The junction capacitance (diameter is 5 µm) is approximately 5.4 fF (at 0.1 GHz), which is close to the fitted value of 6 fF in [78].
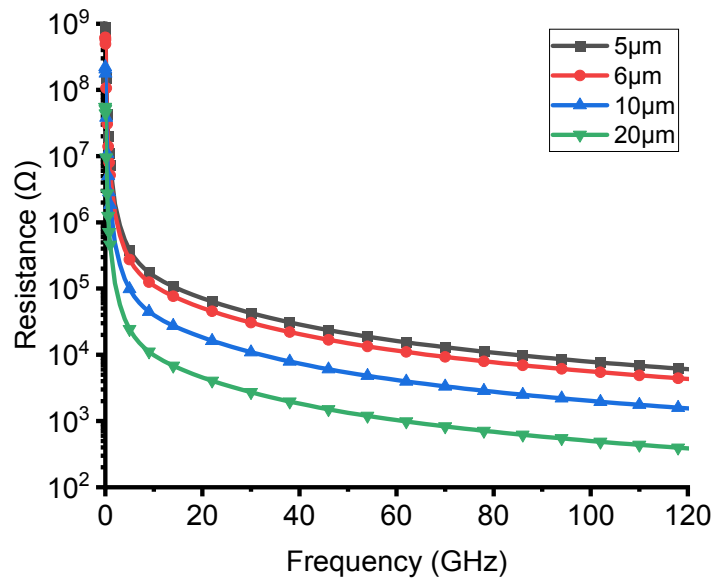
Figure 7-20 Extracted R_j of MUTC-PDs from TCAD simulation.
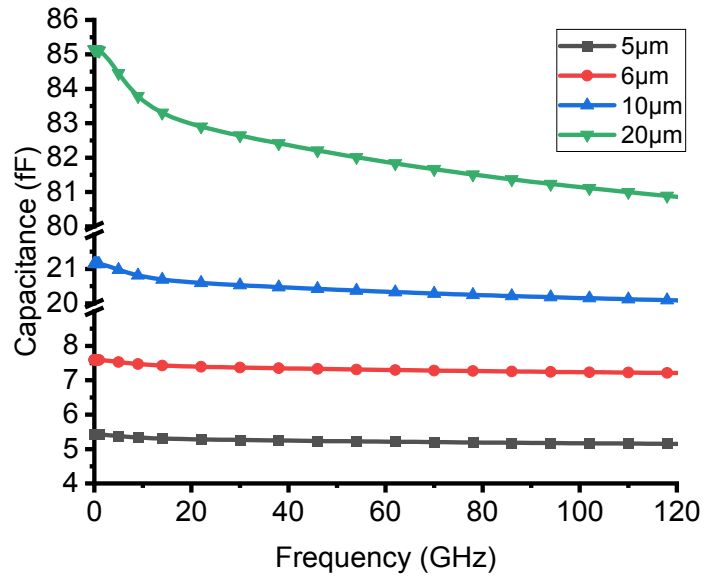
Figure 7-21 Extracted C_j of MUTC-PDs from TCAD simulation.

Table 7-1 Parameters of the equivalent circuit model (Circuit Model A) for the MUTC-PD.

Size (μm)	R_t (Ω)	C_t (fF)	R_j (Ω)	C_j (fF)	C_p (fF)	R_s (Ω)	L_s (pH)
5	50	45	200 M	6	6	6	90
6	50	45	200 M	8	6	6	86
10	50	45	200 M	27	6	6	70
20	50	45	200 M	106	6	5	65

Table 7-2 Parameters of the equivalent circuit model (Circuit Model B) for the MUTC-PD.

Size (μm)	R_t (Ω)	C_t (fF)	C_p (fF)	R_s (Ω)	L_s (pH)
5	50	45	6	6	90
6	50	45	6	6	86
10	50	45	6	6	70
20	50	45	6	5	65

Table 7-3 Simulated and measured bandwidth of the MUTC-PD.

Size (μm)	Measured (GHz)	Circuit Model A (GHz)	Circuit Model B (GHz)
5	112	111	113
6	106	105	107
10	78	72.5	80.5
20	40	31.5	38.5

The simulated bandwidth using the equivalent circuit model (Circuit Model A and B) and measured bandwidth of the MUTC-PD are given in Table 7-3. Obviously, the frequency response analysis methodology using the equivalent circuit model (Circuit Model A and B) is an accurate and reliable way to analyze the performance of the InGaAs/InP photodiode. In the following section, the equivalent circuit model (Circuit Model B) will be adopted to analyze the frequency responses of the OSJ-PD, MOSJ-PD, and EC-OSJ-WGPD.

7.3.3 Discussion

In Silvaco TCAD simulation, S-parameters, Resistance, and Capacitance of the photodiode can be extracted using small signal analysis. The extracted resistance and capacitance are shown in Figures 7-7, 7-8, 7-20, and 7-21. The resistance and capacitance are frequency dependent. This newly observed phenomenon is due to the nonlinear effect inside the photodiode, which is investigated in [116]. The resistance drops significantly from low frequency to high frequency. The capacitance drops slightly from low frequency to high frequency. This phenomenon has been successfully predicted by the TCAD simulation and is similar to the phenomenon discussed in [116].

7.4 Frequency response analysis using equivalent circuit model

7.4.1 One-sided junction photodiode
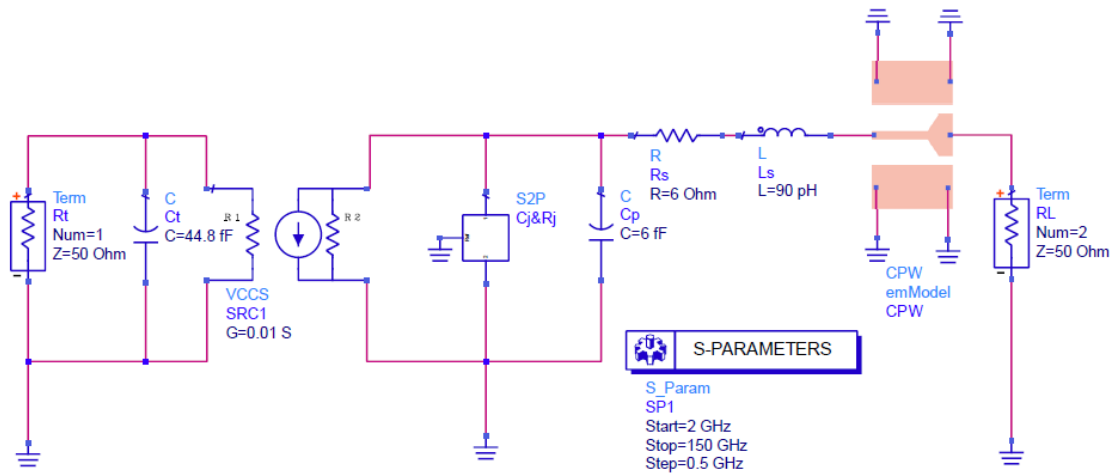
Figure 7-22 ADS schematic diagram of the OSJ-PD with a diameter of 5 μm.
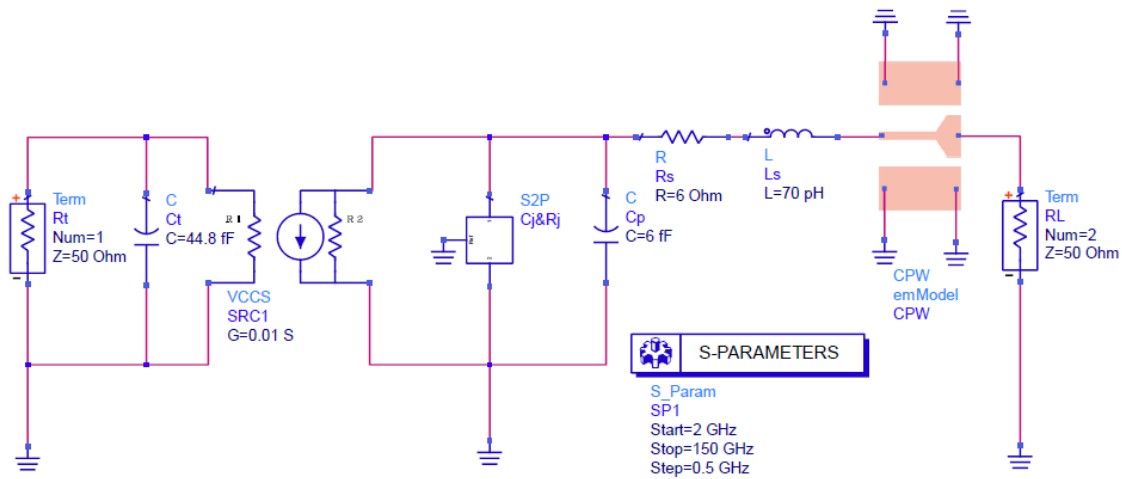
Figure 7-23 ADS schematic diagram of the OSJ-PD with a diameter of 6 μm.

The high-speed OSJ-PD with low junction capacitance has been investigated in Chapter 4 using TCAD simulation. However, the influence of the external circuit (CPW Pad) has not been included. In this section, the equivalent circuit model (Circuit Model B) is used to analyze the frequency response of the OSJ-PD. The ADS schematic diagrams

of the OSJ-PDs with diameters of 5 and 6 μm are given in Figures 7-22 and 7-23. The parameters (C_p, R_s, and L_s) of the OSJ-PD are the same as the parameters of the MUTC-PD [78] by assuming that the same external circuit is adopted. The transit time (R_t and C_t) is calculated by setting the load RESISTANCE to 0 in TCAD simulation. The extracted C_j and R_j of the OSJ-PDs with diameters of 5 and 6 μm are given in Figures 7-24 and 7-25. At low frequency (1 GHz), the R_j is approximately 10 MΩ, and it drops with the increase of frequency. The extracted values of C_j of the OSJ-PDs with diameters of 5 and 6 μm are approximately 3.6 and 5.1 fF.
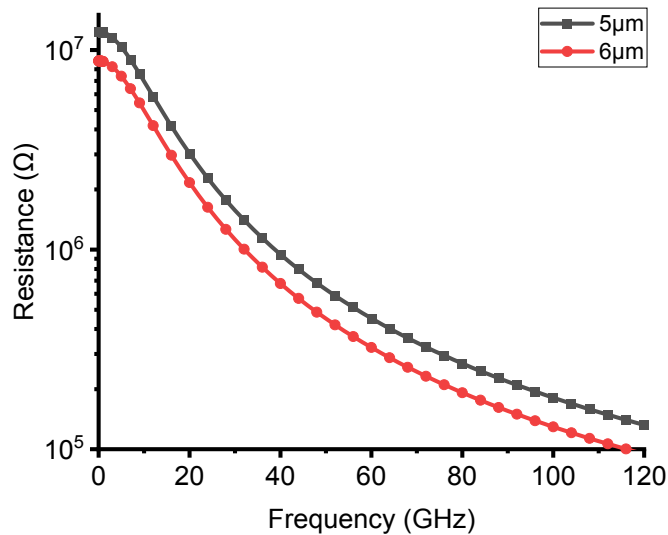
Figure 7-24 Extracted R_j of OSJ-PDs from TCAD simulation.

The simulated frequency response of the OSJ-PDs using the equivalent circuit model is given in Figure 7-26. The photodiodes with diameters of 5 and 6 μm achieve bandwidths of 119 and 114 GHz, respectively. The transit time limited bandwidth simulated by TCAD is also given in Figure 7-26. The transit time limited bandwidth is 71 GHz. Due to the tuning effect of the external circuit, the simulated frequency response is much higher than the transit time limited bandwidth. The operation mechanism is similar to the circuit model

in Figure 7-2, the current flowing through the load can be calculated by $I_L(\omega) = I_{ph}(\omega) \cdot H(\omega)$. The transfer function $H(\omega)$ of the circuit is specially designed so that the response at high frequency is increased. As a result, the overall bandwidth can be increased.
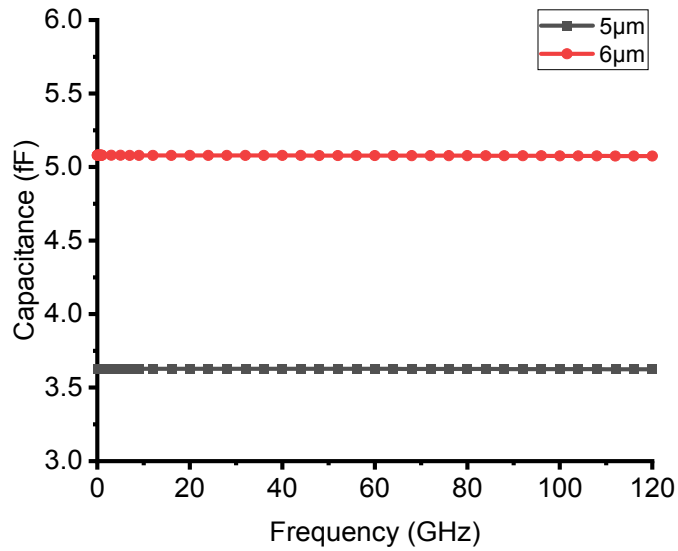
Figure 7-25 Extracted C_j of OSJ-PDs from TCAD simulation.
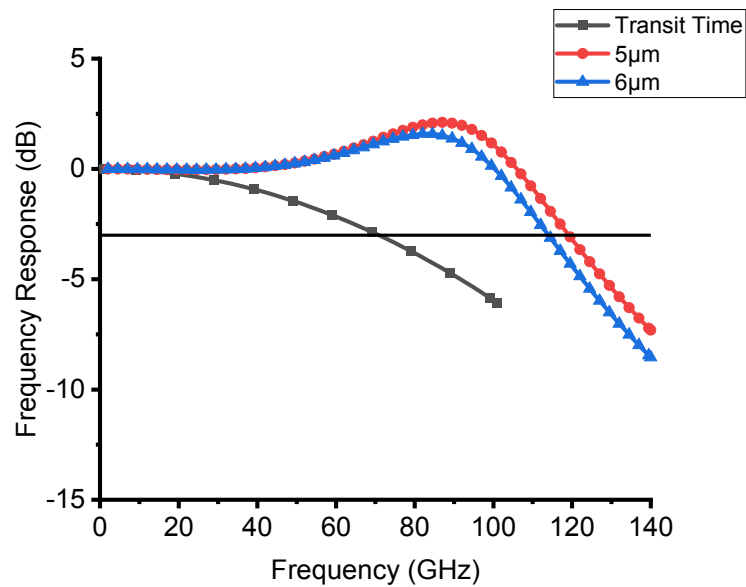
Figure 7-26 Simulated frequency response of the OSJ-PD with diameters of 5 and 6 μm.

7.4.2 Modified one-sided junction photodiode
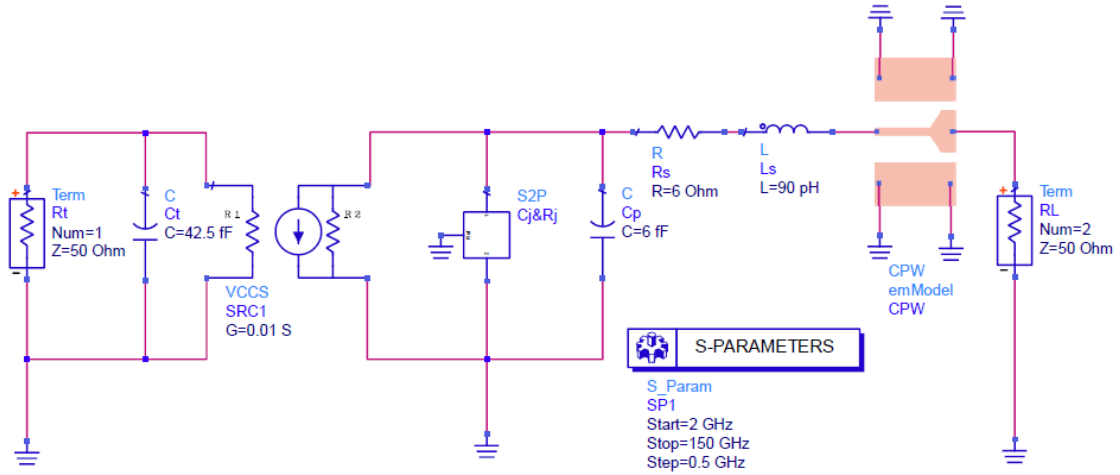
Figure 7-27 ADS schematic diagram of the MOSJ-PD with a diameter of 5 μm.
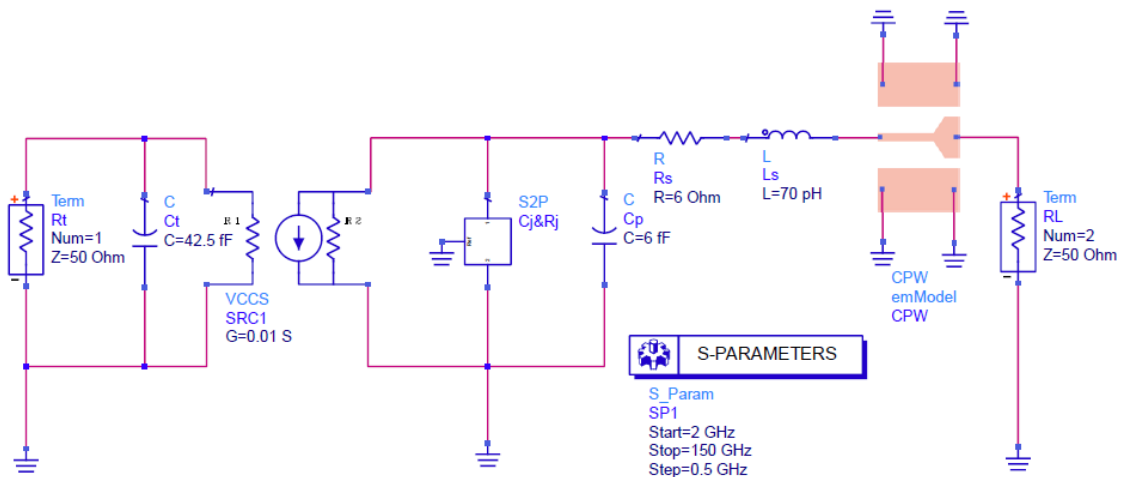
Figure 7-28 ADS schematic diagram of the MOSJ-PD with a diameter of 6 μm.

The ADS schematic diagrams of the MOSJ-PDs with diameters of 5 and 6 μm are given in Figures 7-27 and 7-28. The transit time limited bandwidth simulated by TCAD is 75 GHz. R_t and C_t with values of 50 Ω and 42.5 fF are used to represent the transit time in the equivalent circuit model. The C_j and R_j are calculated using TCAD software and then imported into ADS as an S2P component (C_j&R_j). The extracted C_j and R_j of the MOSJ-

PDs with diameters of 5 and 6 μm are given in Figures 7-29 and 7-30. At low frequency (1 GHz), the R_j is approximately 10 MΩ, and it drops with the increase of frequency. The extracted values of C_j of the MOSJ-PDs with diameters of 5 and 6 μm are approximately 3.8 and 5.3 fF.
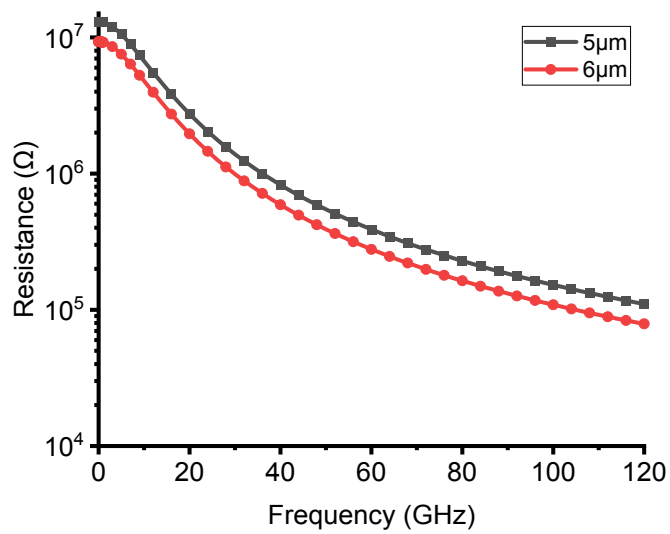
Figure 7-29 Extracted R_j of MOSJ-PDs from TCAD simulation.
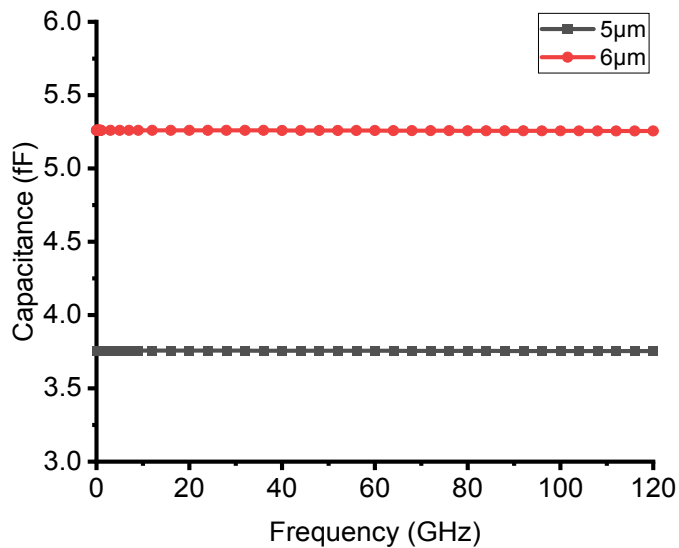
Figure 7-30 Extracted C_j of MOSJ-PDs from TCAD simulation.
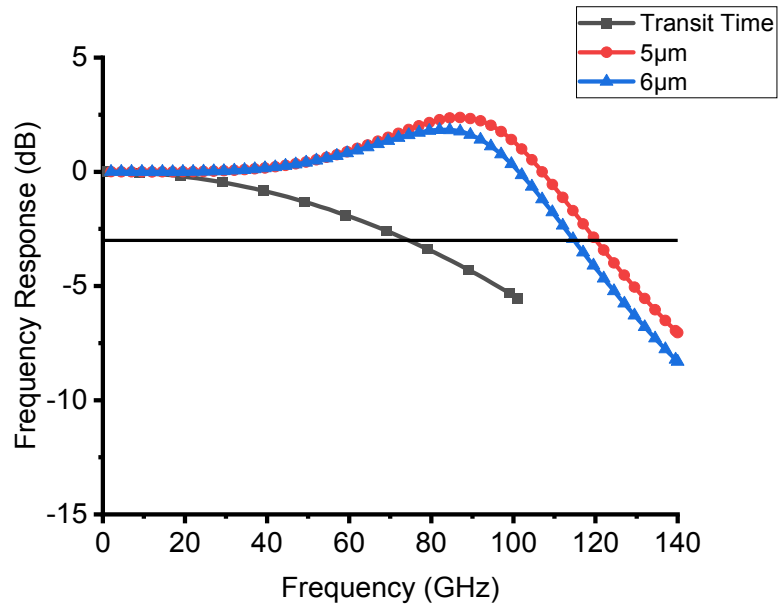
Figure 7-31 Simulated frequency response of the MOSJ-PD with diameters of 5 and 6 μm.

The simulated frequency response of the MOSJ-PDs using the equivalent circuit model is given in Figure 7-31. The photodiodes with diameters of 5 and 6 μm achieve bandwidths of 120 and 115 GHz, respectively. Even though the transit time limited bandwidth of the OSJ-PD (71 GHz) is lower than the MOSJ-PD (75 GHz), they achieve similar bandwidths. This is mainly due to the lower junction capacitance of the OSJ-PD, which compensates for the lower transit time limited bandwidth.

7.4.3 Evanescently coupled one-sided junction waveguide photodiode
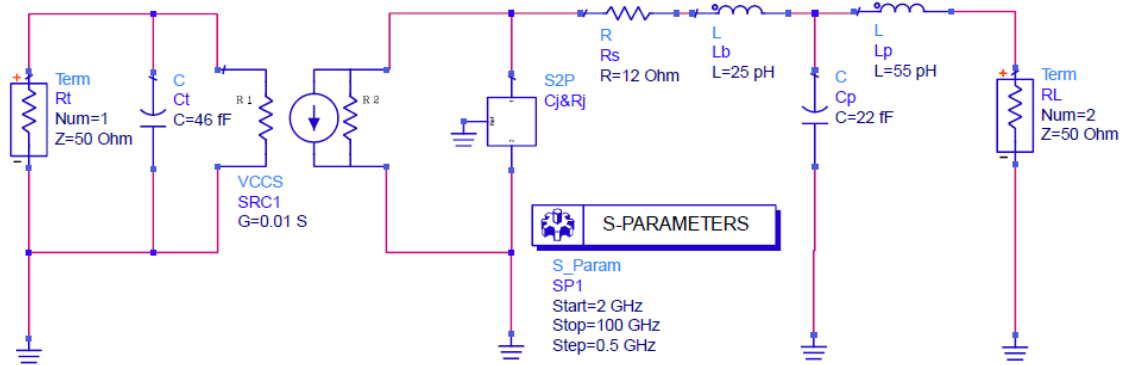
Figure 7-32 ADS schematic diagram of the EC-OSJ-WGPD.
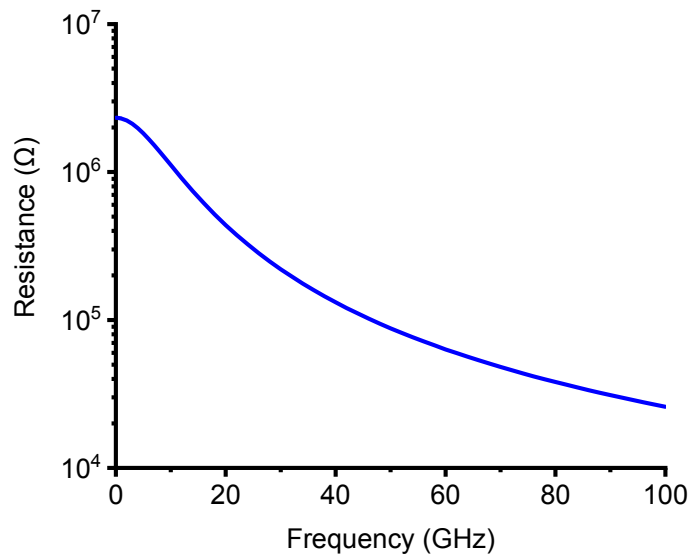
Figure 7-33 Extracted R_j of EC-OSJ-WGPD from TCAD simulation.

The comprehensive analysis of the EC-OSJ-WGPD has been provided in Chapter 6. It is assumed that the same CPW Pad (Figures 7-3 and 7-6) is adopted for the EC-OSJ-WGPD, and the corresponding equivalent circuit model is given in Figure 7-32. The parameters ($R_s, L_b, C_p, and L_p$), which represent the external circuit, are the same as [94]. The transit time ($R_t and C_t$) is calculated using TCAD simulation. The S2P component

(C_j&R_j), which represents the photodiode, is extracted using TCAD simulation. The extracted C_j and R_j of the EC-OSJ-WGPD are given in Figures 7-33 and 7-34. As shown in Figure 7-35, the simulated bandwidth of the EC-OSJ-WGPD is 65.5 GHz, and the transit time limited bandwidth is 69 GHz.
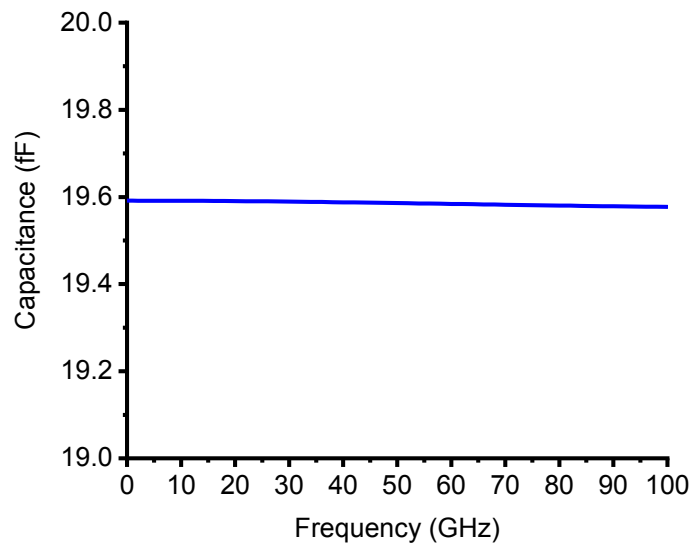
Figure 7-34 Extracted C_j of EC-OSJ-WGPD from TCAD simulation.
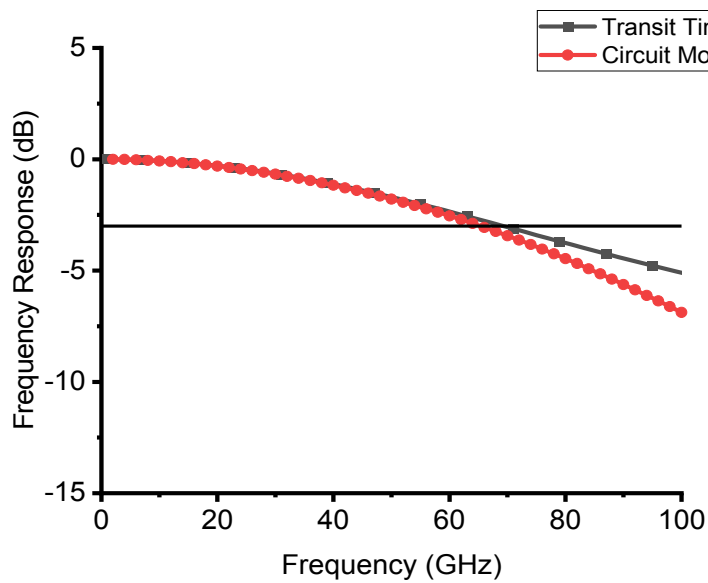
Figure 7-35 Simulated frequency response of the EC-OSJ-WGPD.

7.4.4 Discussion

Table 7-4 Simulated bandwidth of the MUTC-PD, OSJ-PD and MOSJ-PD using equivalent circuit model (Circuit Model B).

Diameter (μm)	MUTC-PD (GHz)	OSJ-PD (GHz)	MOSJ-PD (GHz)
5	113	119	120
6	107	114	115

Table 7-5 Extracted C_j of the MUTC-PD, OSJ-PD and MOSJ-PD using TCAD simulation.

Diameter (μm)	MUTC-PD (fF)	OSJ-PD (fF)	MOSJ-PD (fF)
5	5.4	3.6	3.8
6	7.6	5.1	5.3

The simulated bandwidths of the MUTC-PD, OSJ-PD, and MOSJ-PD using the equivalent circuit model are given in Table 7-4. For the photodiode with the same diameter (5 or 6 μm), the bandwidth of the OSJ-PD and MOSJ-PD is larger than the MUTC-PD's. This is mainly due to the lower junction capacitance of the OSJ-PD and MOSJ-PD. The junction capacitances of the MUTC-PD, OSJ-PD, and MOSJ-PD at low frequency are given in Table 7-5. The transit time limited bandwidths of the OSJ-PD and MOSJ-PD are 71 and 75 GHz, respectively. The depletion widths of the OSJ-PD and MOSJ-PD are approximately 640 nm (Chapter 4) and 620 nm (Chapter 5), respectively. Larger depletion width indicates lower junction capacitance. For the OSJ-PD introduced in Chapter 4, the lower junction capacitance could compensate for the lower transit time limited bandwidth. As a result, the bandwidth of the OSJ-PD is almost the same as the MOSJ-PD (the discrepancy is less than 1 GHz). The overall frequency response of the photodiode is mainly determined by the transit time, junction capacitance, and external circuit. To

achieve optimum performance, all these factors should be considered in the design of the epitaxial layer structure and the external circuit of the photodiode.

7.5 Conclusions

In this chapter, the frequency response analysis of the InGaAs/InP photodiodes using an equivalent circuit model has been introduced. Firstly, the basic and improved equivalent circuit models of the InGaAs/InP photodiodes have been discussed. Secondly, the equivalent circuit models (Circuit Model A and B) have been adopted to analyze the frequency response of the waveguide photodiode [94] and MUTC-PD [78], and good agreement between simulation and measurement has been achieved. Finally, the equivalent circuit model (Circuit Model B) has been used to simulate the frequency responses of the OSJ-PD, MOSJ-PD, and EC-OSJ-WGPD. Due to the lower junction capacitance, the OSJ-PD and MOSJ-PD can achieve higher bandwidths than the MUTC-PD. The simulated bandwidths of the OSJ-PD (5 μm) and MOSJ-PD (5 μm) are 119 and 120 GHz, which are 5.3% and 6.2% higher than the MUTC-PD (5 μm). The EC-OSJ-WGPD achieves a bandwidth of 65.5 GHz.

Chapter 8 Conclusions and Future Work

This chapter summarizes the contributions of the thesis and introduces the research works to do in the future.

8.1 Thesis contributions

The thesis has provided a theoretical and numerical study of InGaAs/InP photodiodes. The concept of one-sided junction photodiode (OSJ-PD) has been proposed for the first time in this thesis. Based on the theoretical and numerical analysis, three new photodiode structures (OSJ-PD, MOSJ-PD, and EC-OSJ-WGPD) have been proposed and investigated. A unique equivalent circuit model has been proposed to analyze the frequency response of InGaAs/InP photodiodes. The main contributions of this thesis are summarized as follows:

1. In Chapter 4, the OSJ-PD has been proposed based on the concept of InGaAs Schottky barrier photodiode and UTC-PD. Compared with the well known UTC-PD, the OSJ-PD has the advantages of simpler epitaxial layer structure and lower junction capacitance, while maintaining the characteristics of high speed and high output power. Due to the higher bias voltage, the saturation photocurrent of OSJ-PD has been high. This research work is related to the following publication:

J. Xu, X. Zhang, and A. Kishk, "Design of high speed InGaAs/InP one-sided junction photodiodes with low junction capacitance," Opt. Commun. 437, 321–329 (2019).

2. At high light intensity, due to the space charge effect, the output photocurrent saturates, and the 3-dB bandwidth has dropped. To overcome the space charge effect in

OSJ-PD, the MOSJ-PD has been proposed by inserting a lightly counter doped cliff layer into the absorption layer. As a result, the output photocurrent and 3-dB bandwidth can be improved simultaneously at a high light intensity. This work has been introduced in Chapter 5 and it is related to the following publication:

J. Xu, X. Zhang, and A. Kishk, "Design of modified InGaAs/InP one-sided junction photodiodes with improved response at high light intensity," Appl. Opt. 57(31), 9365–9374 (2018).

3. In Chapter 6, the EC-OSJ-WGPD has been proposed and analyzed. A numerical modelling procedure (multiphysics simulation) has been introduced to analyze the performance of EC-OSJ-WGPD. The multiphysics simulation can provide information inside the device, such as photogeneration rate and internal optical power distribution, which could not be experimentally measured. The designed EC-OSJ-WGPD has achieved a high responsivity of 0.98 A/W. This work is related to the following publication:

J. Xu, X. Zhang, and A. Kishk, "InGaAs/InP evanescently coupled one-sided junction waveguide photodiode design," Opt. Quant. Electron. 52, 266 (2020).

4. In Chapter 7, a unique frequency response analysis methodology using an equivalent circuit model has been introduced. The equivalent circuit model (Circuit Model B) combines the results of TCAD simulation and data fitting, and it has demonstrated high accuracy in the frequency response analysis. The OSJ-PD and MOSJ-PD with a diameter of 5 μm achieve bandwidths of 119 and 120 GHz, which are 5.3% and 6.2% higher than the well known MUTC-PD.

8.2 Future work

As discussed in previous chapters, the applications of InGaAs/InP photodiodes are very broad, and there is an urgent need for high speed and high power photodiodes. In this thesis, the main contribution is the proposal of a one-sided junction photodiode. However, the study was limited to the numerical study of the photodiodes. There is still more to explore experimentally. Possible future works include: fabricating and measuring the proposed photodiodes, integrating the high speed and high power photodiodes with antennas (photodiode emitters), adopting the photodiode emitters in radio-over-fiber wireless communication systems operating at MMW and THz frequency band, etc.

References

[1]   K. Fukuchi, T. Kasamatsu, M. Morie, R. Ohhira, T. Ito, K. Sekiya, D. Ogasahara, and T. Ono, "10.92-Tb/s (273 x 40-Gb/s) triple-band/ultra-dense WDM optical-repeatered transmission experiment," Optical Fiber Communication Conference and International Conference on Quantum Information (2001), Paper PD24, Anaheim, California.

[2]   A. J. Seeds and K. J. Williams, "Microwave Photonics," J. Lightwave Technol. 24(12), 4628–4641 (2006).

[3]   T. Nagatsuma, A. Kaino, S. Hisatake, K. Ajito, H.-J. Song, A. Wakatsuki, Y. Muramoto, N. Kukutsu, and Y. Kado, "Continuous-Wave Terahertz Spectroscopy System Based on Photodiodes, " PIERS ONLINE 6(4), 390‐394 (2010).

[4]   M. Tonouchi, "Cutting-edge terahertz technology," Nat. Photonics 1(2), 97–105 (2007).

[5]   T. Nagatsuma, "Terahertz technologies: present and future," IEICE Electron. Express 8(14), 1127–1142 (2011).

[6]   T. Ishibashi, Y. Muramoto, T. Yoshimatsu, and H. Ito, "Unitraveling-Carrier Photodiodes for Terahertz Applications," IEEE J. Sel. Top. Quantum Electron. 20(6), 79–88 (2014).

[7]   H. J. Song and T. Nagatsuma, "Present and future of Terahertz communications," IEEE Trans. Terahertz Sci. Technol.1(1), 256–263 (2011).

[8]   J.-W. Shi, C.-B. Huang and C.-L. Pan, "Millimeter-wave photonic wireless links for very high data rate communication," NPG Asia Mater. 3(4), 41–48 (2011).

[9]   S. Koenig, D. Lopez-Diaz, J. Antes, F. Boes, R. Henneberger, A. Leuther, A. Tessmann, R. Schmogrow, D. Hillerkuss, R. Palmer, T. Zwick, C. Koos, W. Freude, O. Ambacher, J. Leuthold, and I. Kallfass, "Wireless sub-THz communication system with high data rate," Nat. Photonics 7(12), 977–981 (2013).

[10]   T. Nagatsuma, H. Ito, and T. Ishibashi, "High-power RF photodiodes and their applications," Laser Photonics Rev. 3(1-2), 123-137 (2009).

[11]   C.-L. Pan, C. W. Chow, C. H. Yeh, C. B. Huang, and J. W. Shi, "Recent advances in millimeter-wave photonic wireless links for very high data rate

communication," 2011 Asia Communications and Photonics Conference and Exhibition (ACP), Shanghai, 2011, pp. 1-6.

[12] V. J. Urick, F. Bucholtz, J. D. McKinney, P. S. Devgan, A. L. Campillo, J. L. Dexter, and K. J. Williams, "Long-haul analog photonics," J. Lightwave Technol. 29(8), 1182–1205 (2011).

[13] K. Li, X. Xie, Q. Li, Y. Shen, M. E. Woodsen, Z. Yang, A. Beling, and J. C. Campbell, "High-power photodiode integrated with coplanar patch antenna for 60-GHz applications," IEEE Photonics Technol. Lett. 27(6), 650-653 (2015).

[14] E. Rouvalis, C. C. Renaud, and A. J. Seeds, "Ultra-fast photodiodes for terahertz generation," https://www.researchgate.net/publication/228879969_Ultra-Fast_Photodiodes_for_Terahertz_Generation.

[15] H. Ito, T. Furuta, F. Nakajima, K. Yoshino, and T. Ishibashi, "Photonic generation of continuous THz wave using uni-traveling-carrier photodiode," J. Lightwave Technol. 23(12), 4016-4021 (2005).

[16] E. Rouvalis, C. C., Renaud, D. G. Moodie, M. J. Robertson, and A. J. Seeds, "Continuous wave terahertz generation from ultra-fast InP-based photodiodes," IEEE Trans. Microwave Theory Tech. 60(3), 509-517 (2012).

[17] A. Beling, J. C. Campbell, K. Li, Q. Li, M. E. Woodson, X. Xie, and Z. Yang, "High-power photodiodes for analog applications," IEICE Trans. Electron. E98.C(8), 764-768 (2015).

[18] T. Nagatsuma, "Photonic measurement technologies for high-speed electronics," Meas. Sci. Technol. 13(11), 1655-1663 (2002).

[19] T. Minotani, A. Hirata, and T. Nagatsuma, "A broadband 120-GHz Schottky-diode receiver for 10-Gbit/s wireless links," IEICE Trans. Electron. E86-C(8), 1501-1505 (2003).

[20] T. Nagatsuma and H. Ito, "High-Power RF Uni-Traveling-Carrier Photodiodes (UTC-PDs) and Their Applications," in Advances in Photodiodes (InTech, 2011).

[21] G. Chattopadhyay, "Technology capabilities and performance of low power terahertz sources," IEEE Trans. THz Sci. Technol., vol. 1, no. 1, pp. 33-53, Sep. 2011.

[22] G. Ghione, Semiconductor Devices for High-Speed Optoelectronics (Cambridge University Press, 2009).

[23] S. M. Sze and K. K. Ng, Physics of Semiconductor Devices (Wiley-Interscience, 2007).

[24] F. F. Masouleh and N. Das, "Application of Metal-Semiconductor-Metal Photodetector in High-Speed Optical Communication Systems," in Advances in Optical Communication (InTech, 2014).

[25] D. A. Neamen, Semiconductor Physics and Devices: Basic Principles (McGraw-Hill, 2012).

[26] M. Bass, V. N. Mahajan, and E. W. Van Stryland, Handbook of Optics. Volume II, Design, Fabrication and Testing, Sources and Detectors, Radiometry and Photometry (McGraw-Hill, 2010).

[27] R. S. Tucker, A. J. Taylor, C. A. Burrus, G. Eisenstein, and J. M. Wiesenfeld, "Coaxially mounted 67 GHz bandwidth InGaAs PIN photodiode," Electron. Lett. 22(17), 917 (1986).

[28] D. G. Parker, "The theory, fabrication and assessment of ultra high speed photodiodes," GEC J. Res. 6, 106-117 (1988).

[29] Tien-Pei Lee, C. Burrus, and A. Dentai, "InGaAs/InP p-i-n photodiodes for lightwave communications at the 0.95-1.65 μm wavelength," IEEE J. Quantum Electron. 17(2), 232–238 (1981).

[30] M. Makiuchi, M. Norimatsu, C. Sakurai, K. Kondo, N. Yamamoto, and M. Yano, "Flip-chip planar GaInAs/InP p-i-n photodiodes-fabrication and characteristics," J. Light. Technol. 13(11), 2270–2275 (1995).

[31] K. Li, E. Rezek, and H. D. Law, "InGaAs pin photodiode fabricated on semi-insulating InP substrate for monolithic integration," Electron. Lett. 20(5), 196 (1984).

[32] K. Kato, S. Hata, K. Kawano, A. Kozen, "Design of Ultrawide-Band, High-Sensitivity p-i-n Protodetectors," IEICE Trans. Electron. E76–C(2), 214–221 (1993).

[33] T. Ishibashi, N. Shimizu, S. Kodama, H. Ito, T. Nagatsuma, and T. Furuta, "Uni-traveling-carrier photodiodes," OSA Ultrafast Electronics and Optoelectronics Topical Meeting (1997), Paper UC3, Incline Village, Nevada.

[34] ATLAS Users Manual, Silvaco International, Santa Clara, 2016.

[35] S. Adachi, Physical Properties of III–V Semiconductor Compounds: InP, InAs, GaAs, GaP, InGaAs and InGaAsP, 1 edition, Wiley Interscience, New York, 1992.

[36] J.-P. Weber, "Optimization of the carrier-induced effective index change in InGaAsP waveguides-application to tunable Bragg filters," IEEE J. Quantum Electron. 30(8), 1801–1816 (1994).

[37]   S. Seifert and P. Runge, "Revised refractive index and absorption of $In_{1-x}Ga_xAs_yP_{1-y}$ lattice-matched to InP in transparent and absorption IR-region," Opt. Mater. Express 6(2), 629 (2016).

[38]   H. Ito, S. Kodama, Y. Muramoto, T. Furuta, T. Nagatsuma, T. Ishibashi, High-speed and high-output InP-InGaAs unitraveling-carrier photodiodes, IEEE J. Sel. Top. Quantum Electron. 10 (2004) 709–727.

[39]   H. Ito, T. Furuta, Y. Hirota, T. Ishibashi, A. Hirata, T. Nagatsuma, H. Matsuo, T. Noguchi, M. Ishiguro, Photonic millimeter-wave emission at 300 GHz using an antenna-integrated uni-travelling-carrier photodiode, Electron. Lett. 38 (2002) 989–990.

[40]   Z. Li, H. Pan, H. Chen, A. Beling, J.C. Campbell, High-Saturation-Current Modified Uni-Traveling-Carrier Photodiode with Cliff Layer, IEEE J. Quantum Electron. 46 (2010) 626–632.

[41]   J.W. Shi, F.M. Kuo, M.Z. Chou, A linear cascade near-ballistic uni-traveling-carrier photodiodes with extremely high saturation-current bandwidth product (6825mA-GHz, 75mA/91GHz) under a 50Ω load, Optical Fiber Communication, 2010: pp. 1–3.

[42]   Y.S. Wu, J.W. Shi, Dynamic Analysis of High-Power and High-Speed Near-Ballistic Unitraveling Carrier Photodiodes at W-Band, IEEE Photonics Technol. Lett. 20 (2008) 1160–1162.

[43]   J.W. Shi, F.M. Kuo, C.J. Wu, C.L. Chang, C.Y. Liu, C.Y. Chen, J.I. Chyi, Extremely High Saturation Current-Bandwidth Product Performance of a Near-Ballistic Uni-Traveling-Carrier Photodiode With a Flip-Chip Bonding Structure, IEEE J. Quantum Electron. 46 (2010) 80–86.

[44]   N. Shimizu, N. Watanabe, T. Furuta, T. Ishibashi, InP-InGaAs uni-traveling-carrier photodiode with improved 3-dB bandwidth of over 150 GHz, IEEE Photonics Technol. Lett. 10 (1998) 412–414.

[45]   J.M. Wun, C.H. Lai, N.W. Chen, J.E. Bowers, J.W. Shi, Flip-Chip Bonding Packaged THz Photodiode With Broadband High-Power Performance, IEEE Photonics Technol. Lett. 26 (2014) 2462–2464.

[46]   H. Ito, T. Furuta, S. Kodama, T. Ishibashi, InP/InGaAs uni-travelling-carrier photodiode with 310 GHz bandwidth, Electron. Lett. 36 (2000) 1809–1810.

[47]   J.-W. Shi, C.-L. Pan, C.-B. Huang, J.-M. Wun, H.-Y. Liu, Y.-L. Zeng, High-Power THz-Wave Generation by Using Ultra-Fast (315 GHz) Uni-Traveling Carrier Photodiode with Novel Collector Design and Photonic Femtosecond

Pulse Generator, Optical Fiber Communication Conference (2015), Paper M3C.6, Optical Society of America, 2015: p. M3C.6.

[48]   V. Rymanov, A. Stöhr, S. Dülme, T. Tekin, Triple transit region photodiodes (TTR-PDs) providing high millimeter wave output power, Opt. Express. 22 (2014) 7550–7558.

[49]   A. Davidson, K. L. Dessau, Photodiode-based detector operates at 60 GHz. http://assets.newport.com/webDocuments-EN/images/Photodiode-Based_Detector.PDF, Undated (accessed Feb. 2018).

[50]   S.-P. Han, H. Ko, J.-W. Park, N. Kim, Y.-J. Yoon, J.-H. Shin, D.Y. Kim, D.H. Lee, K.H. Park, InGaAs Schottky barrier diode array detector for a real-time compact terahertz line scanner, Opt. Express. 21 (2013) 25874–25882.

[51]   S.S. Li, Development of a high speed InGaAs/InP Schottky barrier photodetector for millimeter-wave fiber optical links. https://apps.dtic.mil/dtic/tr/fulltext/u2/a188594.pdf, 1987, (accessed Oct. 2018).

[52]   N. Emeis, H. Schumacher, H. Beneking, High-speed GaInAs Schottky photodetector, Electron. Lett. 21 (1985) 180–181.

[53]   J.-H. Kim, S.S. Li, L. Figueroa, T.F. Carruthers, R.S. Wagner, High-speed $Ga_{0.47}In_{0.53}As$/InP infra-red Schottky-barrier photodiodes, Electron. Lett. 24 (1988) 1067–1068.

[54]   L. He, M.J. Costello, K.Y. Cheng, D.E. Wohlert, Enhanced Schottky barrier on InGaAs for high performance photodetector application, J. Vac. Sci. Technol., A. 16 (1998) 1646–1649.

[55]   H.J. Lee, W.A. Anderson, H. Hardtdegen, H. Lüth, Barrier height enhancement of Schottky diodes on n-$In_{0.53}Ga_{0.47}As$ by cryogenic processing, Appl. Phys. Lett. 63 (1993) 1939–1941.

[56]   K.C. Hwang, S.S. Li, C. Park, T.J. Anderson, Schottky barrier height enhancement of n- $In_{0.53}Ga_{0.47}As$ by a novel chemical passivation technique, J. Appl. Phys. 67 (1990) 6571–6573.

[57]   J.B.D. Soole, H. Schumacher, H.P. LeBlanc, R. Bhat, M.A. Koza, High-speed performance of OMCVD grown InAlAs/InGaAs MSM photodetectors at 1.5 μm and 1.3 μm wavelengths, IEEE Photonics Technol. Lett. 1 (1989) 250–252.

[58]   J.B.D. Soole, H. Schumacher, InGaAs metal-semiconductor-metal photodetectors for long wavelength optical communications, IEEE J. Quantum Electron. 27 (1991) 737–752.

[59] D. Kuhl, F. Hieronymi, E.H. Bottcher, T. Wolf, A. Krost, D. Bimberg, Very high-speed metal-semiconductor-metal InGaAs: Fe photodetectors with InP: Fe barrier enhancement layer grown by low pressure metalorganic chemical vapour deposition, Electron. Lett. 26 (1990) 2107–2109.

[60] R. Wang, M. Xu, P.D. Ye, R. Huang, Schottky-barrier height modulation of metal/In$_{0.53}$Ga$_{0.47}$As interfaces by insertion of atomic-layer deposited ultrathin Al$_2$O$_3$, J. Vac. Sci. Technol. B. 29 (2011) 041206.

[61] P. Kordoš, M. Marso, R. Meyer, H. Lüth, Schottky barrier height enhancement on n-In$_{0.53}$Ga$_{0.47}$As, J. Appl. Phys. 72 (1992) 2347–2355.

[62] C.Y. Chen, A.Y. Cho, K.Y. Cheng, P.A. Garbinski, Quasi-Schottky barrier diode on n-Ga$_{0.47}$In$_{0.53}$As using a fully depleted p$^+$-Ga$_{0.47}$In$_{0.53}$As layer grown by molecular beam epitaxy, Appl. Phys. Lett. 40 (1982) 401–403.

[63] P. Kordos, M. Marso, R. Meyer, H. Luth, Schottky contacts on n-In$_{0.53}$Ga$_{0.47}$As with enhanced barriers by counter-doped interfacial layers, IEEE Trans. Electron Devices. 39 (1992) 1970–1972.

[64] C. Hu, Modern Semiconductor Devices for Integrated Circuits, Prentice Hall, 2010.

[65] S. Srivastava, K.P. Roenker, Numerical modeling study of the InP/InGaAs uni-travelling carrier photodiode, Solid-State Electron. 48 (2004) 461–470.

[66] T. Ishibashi, T. Furuta, H. Fushimi, S. Kodama, H. Ito, T. Nagatsuma, N. Shimizu, Y. Miyamoto, InP/InGaAs Uni-Traveling-Carrier Photodiodes, IEICE Trans. Electron. E83–C (2000) 938–949.

[67] J.W. Parks, A.W. Smith, K.F. Brennan, L.E. Tarof, Theoretical study of device sensitivity and gain saturation of separate absorption, grading, charge, and multiplication InP/InGaAs avalanche photodiodes, IEEE Trans. Electron Devices. 43 (1996) 2113–2121.

[68] S. Datta, S. Shi, K.P. Roenker, M.M. Cahay, W.E. Stanchina, Simulation and design of InAlAs/InGaAs PNP heterojunction bipolar transistors, IEEE Trans. Electron Devices. 45 (1998) 1634–1643.

[69] S. Srivastava, Simulation study of InP-based uni-traveling carrier photodiode (Master's Thesis), University of Cincinnati, 2003.

[70] P.A. Balaraman, Design, simulation and modeling of InP/GaAsSb/InP double heterojunction bipolar transistors (Master's Thesis), University of Cincinnati, 2003.

[71] Y.R. Shrestha, Numerical simulation of GaAsSb/InP uni-traveling carrier photodiode (Master's Thesis), University of Cincinnati, 2005.

[72]   New semiconductor materials, characteristics and properties, http://www.ioffe.rssi.ru/SVA/NSM/ (accessed Feb. 2018).

[73]   R.K. Ahrenkiel, R. Ellingson, S. Johnston, M. Wanlass, Recombination lifetime of $In_{0.53}Ga_{0.47}As$ as a function of doping density, Appl. Phys. Lett. 72 (1998) 3470–3472.

[74]   E. Rouvalis, F. N. Baynes, X. Xie, K. Li, Q. Zhou, F. Quinlan, T. M. Fortier, S. A. Diddams, A. G. Steffan, A. Beling, and J. C. Campbell, "High-Power and High-Linearity Photodetector Modules for Microwave Photonic Applications," J. Lightwave Technol. 32(20), 3810–3816 (2014).

[75]   Xiaowei Li, Ning Li, Xiaoguang Zheng, S. Demiguel, J. C. Campbell, D. A. Tulchinsky, and K. J. Williams, "High-saturation-current InP-InGaAs photodiode with partially depleted absorber," IEEE Photonics Technol. Lett. 15(9), 1276–1278 (2003).

[76]   M. Chtioui, A. Enard, D. Carpentier, S. Bernard, B. Rousseau, F. Lelarge, F. Pommereau, and M. Achouche, "High-performance uni-traveling-carrier photodiodes with a new collector design," IEEE Photonics Technol. Lett. 20(13), 1163–1165 (2008).

[77]   M. Chtioui, F. Lelarge, A. Enard, F. Pommereau, D. Carpentier, A. Marceaux, F. van Dijk, and M. Achouche, "High responsivity and high power utc and mutc gainas-inp photodiodes," IEEE Photonics Technol. Lett. 24(4), 318–320 (2012).

[78]   Q. Li, K. Li, Y. Fu, X. Xie, Z. Yang, A. Beling, and J. C. Campbell, "High-power flip-chip bonded photodiode with 110 GHz bandwidth," J. Lightwave Technol. 34(9), 2139–2144 (2016).

[79]   Y. Hu, B. S. Marks, C. R. Menyuk, V. J. Urick, and K. J. Williams, "Modeling sources of nonlinearity in a simple p-i-n photodetector," J. Lightwave Technol. 32(20), 3710–3720 (2014).

[80]   C. Gardes, J. Justice, F. Gity, H. Yang, and B. Corbett, "Numerical simulations with energy balance model for unitraveling-carrier photodiode," IEEE International Conference on Nanotechnology (2015), Rome, Italy

[81]   S. M. Mahmudur Rahman, Hans Hjelmgren, Josip Vukusic, Jan Stake, Peter A. Andrekson, and Herbert Zirath, "Hydrodynamic simulations of unitraveling-carrier photodiodes," IEEE J. Quantum Electron. 43(11), 1088–1094 (2007).

[82]   Q. Zhou, A. S. Cross, A. Beling, Y. Fu, Z. Lu, and J. C. Campbell, "High-power V-band InGaAs/InP photodiodes," IEEE Photonics Technol. Lett. 25(10), 907–909 (2013).

[83]   A. Beling, Q. Zhou, J. H. Sinsky, A. S. Cross, A. Gnauck, L. Buhl, and J. C. Campbell, "30 GHz fully packaged modified uni-traveling carrier photodiodes for high-power applications," IEEE Avionics Fiber Optics and Photonics Conf. (2013), San Diego, CA

[84]   Y. Muramoto and T. Ishibashi, "InP/InGaAs pin photodiode structure maximising bandwidth and efficiency," Electron. Lett. 39(24), 1749 (2003).

[85]   K. Kato, S. Hata, K. Kawano, J. Yoshida, and A. Kozen, "A High-Efficiency 50 GHz InGaAs Multimode Waveguide Photodetector," IEEE J. Quantum Electron. 28(12), 2728–2735 (1992).

[86]   V. Magnin, L. Giraudet, J. Harari, J. Decobert, P. Pagnot, E. Boucherez, and D. Decoster, "Design, optimization, and fabrication of side-illuminated p-i-n photodetectors with high responsivity and high alignment tolerance for 1.3- and 1.55-μm wavelength use," J. Light. Technol. 20(3), 477–488 (2002).

[87]   J. W. Park, "High-responsivity and high-speed waveguide photodiode with a thin absorption region," IEEE Photonics Technol. Lett. 22(13), 975–977 (2010).

[88]   H. G. Bach, A. Beling, G. G. Mekonnen, R. Kunkel, D. Schmidt, W. Ebert, A. Seeger, M. Stollberg, and W. Schlaak, "InP-based waveguide-integrated photodetector with 100-GHz bandwidth," IEEE J. Sel. Top. Quantum Electron. 10(4), 668–672 (2004).

[89]   J. Harari, F. Journet, O. Rabii, G. Jin, J. P. Vilcot, and D. Decoster, "Modeling of Waveguide PIN Photodetectors Under Very High Optical Power," IEEE Trans. Microw. Theory Tech. 43(9), 2304–2310 (1995).

[90]   J. W. Park, H. S. Ko, E. D. Sim, and Y. S. Baek, "Optimization of high responsivity waveguide photodiode with a thin absorption layer," Appl. Phys. Lett. 90(9), 091101 (2007).

[91]   J.-W. Park, "Waveguide Photodiode (WGPD) with a Thin Absorption Layer," in Advances in Optical and Photonic Devices (InTech, 2012).

[92]   S. Demiguel, X. Li, N. Li, H. Chen, J. C. Campbell, J. Wei, and A. Anselm, "Analysis of partially depleted absorber waveguide photodiodes," J. Light. Technol. 23(8), 2505–2512 (2005).

[93]   S. Q. Liu, X. H. Yang, Y. Liu, B. Li, and Q. Han, "Design and fabrication of a high-performance evanescently coupled waveguide photodetector," Chinese Phys. B 22(10), 108503 (2013).

[94]   S. Demiguel, L. Giraudet, L. Joulaud, J. Decobert, F. Blache, V. Coupe, F. Jorge, E. Boucherez, M. Achouche, and F. Devaux, "Evanescently coupled photodiodes integrating a double-stage taper for 40-Gb/s applications-compared performance with side-illuminated photodiodes," J. Light. Technol. 20(12), 2004–2014 (2002).

[95]   M. Achouche, V. Magnin, J. Harari, F. Lelarge, E. Derouin, C. Jany, D. Carpentier, F. Blache, and D. Decoster, "High Performance Evanescent Edge Coupled Waveguide Unitraveling-Carrier Photodiodes for >40-Gb/s Optical Receivers," IEEE Photonics Technol. Lett. 16(2), 584–586 (2004).

[96]   Y. S. Wu, J. W. Shi, J. Y. Wu, F. H. Huang, Y. J. Chan, Y. L. Huang, and R. Xuan, "High-performance evanescently edge coupled photodiodes with partially p-doped photoabsorption layer at 1.55-μm wavelength," IEEE Photonics Technol. Lett. 17(4), 878–880 (2005).

[97]   L. Giraudet, J. Harari, V. Magnin, P. Pagnod, E. Boucherez, J. Decobert, J. Bonnet-Gamard, D. Carpentier, C. Jany, F. Blache, and D. Decoster, "High speed evanescently coupled PIN photodiodes for hybridisation on silicon platform optimised with genetic algorithm," Electron. Lett. 37(15), 973–975 (2001).

[98]   N. Michel, V. Magnin, J. Harari, A. Marceaux, O. Parillaud, D. Decoster, and N. Vodjdani, "High-power evanescently-coupled waveguide photodiodes," IEE Proceedings of Optoelectron. 153(4), 199–204 (2006).

[99]   J.-W. Shi, Y.-S. Wu, F.-H. Huang, and Y.-J. Chan, "High-responsivity, high-speed, and high-saturation-power performances of evanescently coupled photodiodes with partially p-doped photo-absorption layer," in IEDM Technical Digest. IEEE International Electron Devices Meeting, 2004. (IEEE, 2005), pp. 351–354.

[100]   J. W. Shi, Y. S. Wu, C. Y. Wu, P. H. Chiu, and C. C. Hong, "High-speed, high-responsivity, and high-power performance of near-ballistic uni-traveling-carrier photodiode at 1.55-μm wavelength," IEEE Photonics Technol. Lett. 17(9), 1929–1931 (2005).

[101]   A. Beling, H. Bach, and D. Schmidt, "InP-Based Waveguide Integrated Photodetectors for High-Speed Optical Communication Systems," https://www.researchgate.net/publication/228512250.

[102] M. Achouche, S. Demiguel, E. Derouin, D. Carpentier, F. Barthe, F. Blache, V. Magnin, J. Harari, D. Decoster, "New all 2-inch manufacturable high performance evanescent coupled waveguide photodiodes with etched mirrors for 40 Gb/s optical receivers", Proc. Optical Fiber Communications (OFC, 2003), pp. 23-24, 2003.

[103] L. Giraudet, "Optical design of evanescently coupled, waveguide-fed photodiodes for ultrawide-band applications," IEEE Photonics Technol. Lett. 11(1), 111–113 (1999).

[104] S. Demiguel, N. Li, X. Li, X. Zheng, J. Kim, J. C. Campbell, H. Lu, and A. Anselm, "Very High-Responsivity Evanescently Coupled Photodiodes Integrating a Short Planar Multimode Waveguide for High-Speed Applications," IEEE Photonics Technol. Lett. 15(12), 1761–1763 (2003).

[105] A. Alping, "Waveguide pin photodetectors: theoretical analysis and design criteria," IEE Proceedings J - Optoelectronics 136(3), 177–182 (1989).

[106] H. Jiang, D.-S. Shin, T.-S. Liao, P. Mages, A. R. Clawson, P. K. L. Yu, T. A. Vang, and D. C. Scott, "Waveguide photodiodes for high-speed detection," in Terahertz and Gigahertz Electronics and Photonics II, R. J. Hwu and K. Wu, eds. (International Society for Optics and Photonics, 2003), 4111, pp. 259–266.

[107] G. Zhou, P. Runge, S. Keyvaninia, S. Seifert, W. Ebert, S. Mutschall, A. Seeger, Q. Li, and A. Beling, "High-Power InP-Based Waveguide Integrated Modified Uni-Traveling-Carrier Photodiodes," J. Light. Technol. 35(4), 717-721 (2017).

[108] Q. Li, K. Sun, K. Li, Q. Yu, P. Runge, W. Ebert, A. Beling, and J. C. Campbell, "High-Power Evanescently Coupled Waveguide MUTC Photodiode With >105-GHz Bandwidth," J. Light. Technol. 35(21), 4752-4757 (2017).

[109] S. Sun, S. Liang, X. Xie, J. Xu, L. Guo, H. Zhu, and W. Wang, "Zero-bias 32 Gb/s evanescently coupled InGaAs/InP UTC-PDs," Opt. Laser Technol. 101, 457–461 (2018).

[110] J. Xu, X. Zhang, and A. Kishk, "Design of high speed InGaAs/InP one-sided junction photodiodes with low junction capacitance," Opt. Commun. 437, 321–329 (2019).

[111] J. Xu, X. Zhang, and A. Kishk, "Design of modified InGaAs/InP one-sided junction photodiodes with improved response at high light intensity," Appl. Opt. 57(31), 9365–9374 (2018).

[112] J. Xu, X. Zhang, and A. Kishk, "Numerical study of the evanescently coupled one-sided junction waveguide photodiode," Proceedings of the 19th International Conference on Numerical Simulation of Optoelectronic Devices (2019), Ottawa, Canada.

[113] J. Xu, X. Zhang, and A. Kishk, "InGaAs/InP evanescently coupled one-sided junction waveguide photodiode design," Opt. Quant. Electron. 52, 266 (2020).

[114] J. W. Shi, F. M. Kuo, and E. J. Bowers, "Design and Analysis of Ultra-High-Speed Near-Ballistic Uni-Traveling-Carrier Photodiodes Under a 50-Ω Load for High-Power Performance," IEEE Photonics Technol. Lett. 24(7), 533–535 (2012).

[115] Y. Wey, K. Giboney, J. Bowers, M. Rodwell, P. Silvestre, P. Thiagarajan, and G. Robinson, "110-GHz GalnAs/InP Double Heterostructure p-i-n Photodetectors," J. Light. Technol. 13(7), 1490–1499 (1995).

[116] M. Natrella, C.-P. Liu, C. Graham, F. van Dijk, H. Liu, C. C. Renaud, and A. J. Seeds, "Accurate equivalent circuit model for millimetre-wave UTC photodiodes," Optics Express, 24(5), 4698–4713 (2016).

[117] G. Zhou, and P. Runge, " Nonlinearities of high-speed p-i-n photodiodes and MUTC-PD photodiode," IEEE Trans. Microw. Theory Tech. 65(6), 2063–2072 (2017).

[118] Naseem, Zohauddin Ahmad, Rui-Lin Chao, Hsiang-Szu Chang, C.-J. Ni, H.-S. Chen, Jack Jia-Sheng Huang, Emin Chou, Yu-Heng Jan, and Jin-Wei Shi, "The enhancement in speed and responsivity of uni-traveling carrier photodiodes with $GaAs_{0.5}Sb_{0.5}/In_{0.53}Ga_{0.47}As$ type-II hybrid absorbers," Optics Express, vol. 27, no. 11, pp. 15495-15504, May 2019.

[119] J.-M. Wun, H.-Y. Liu, C.-H. Lai, Y.-S. Chen, S.-D. Yang, C.-L. Pan, J. E. Bowers, C.-B. Huang, and J.-W. Shi, "Photonic high-power 160-GHz signal generation by using ultrafast photodiode and a high-repetition-rate femtosecond optical pulse train generator," IEEE J. Sel. Top. Quantum Electron. 20, 3803507 (2014).

[120] J. M. Wun, Y. W. Wang, and J. W. Shi, "Ultrafast uni-traveling carrier photodiodes with $GaAs_{0.5}Sb_{0.5}/In_{0.53}Ga_{0.47}As$ type-II hybrid absorbers for high-power operation at THz frequencies," IEEE J. Sel. Top. Quantum Electron. 24, 1–7 (2018).

[121] K. Kato, S. Hata, K. Kawano, and A. Kozen, "Design of ultrawideband, high-sensitivity p-i-n photodetectors," IEICE Trans. Electron, vol. E76-C, pp. 214–221, Feb. 1993.

[122] K.N.Z. Ariffin, PHYSICAL MODELLING OF TUNNEL DIODES FOR TERAHERTZ FREQUENCY APPLICATIONS (Doctoral Dissertation), The University of Manchester, 2019.

[123] Planar Electromagnetic (EM) Simulation in ADS, https://www.keysight.com/us/en/assets/7018-05192/technical-overviews/5992-1479.pdf (accessed Nov. 2019).

[124] S. Kassim and F. Malek, "The Emerging Role of EM Simulation in IEEE 802.16e Mobile WiMAX Power Amplifier Design," 2011 Second International Conference on Intelligent Systems, Modelling and Simulation, Kuala Lumpur, 2011, pp. 404-409.

[125] I.J. Bahl, Lumped Elements for RF and Microwave Circuits, Artech House, Boston, 2003, pp. 171-172.
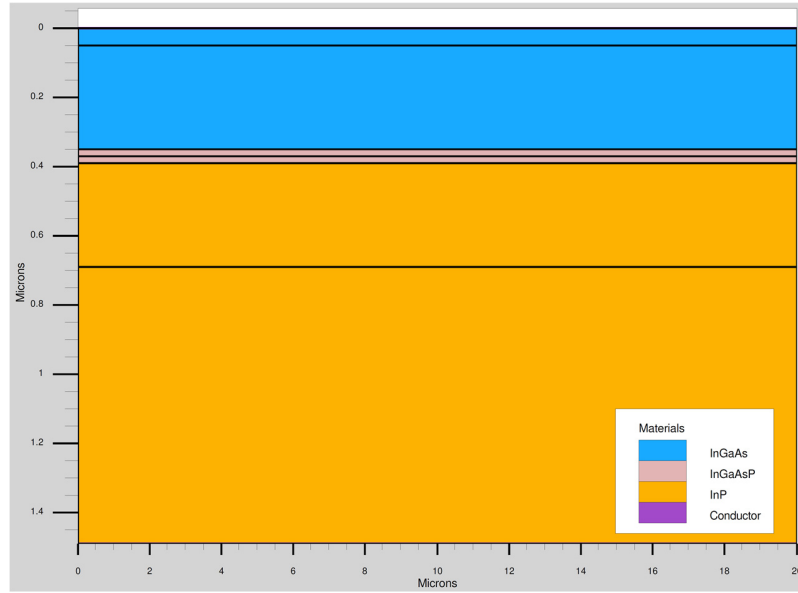
Appendix A

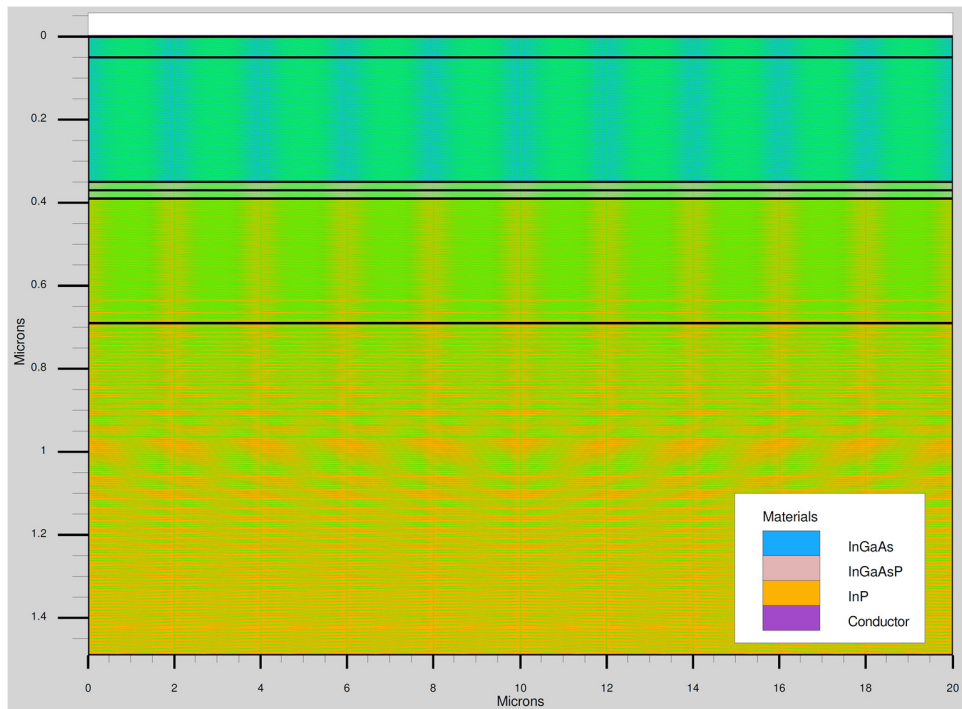*Figure A-1 Epitaxial layer structure of the OSJ-PD in Silvaco Atlas (Area is 20 μm²).*

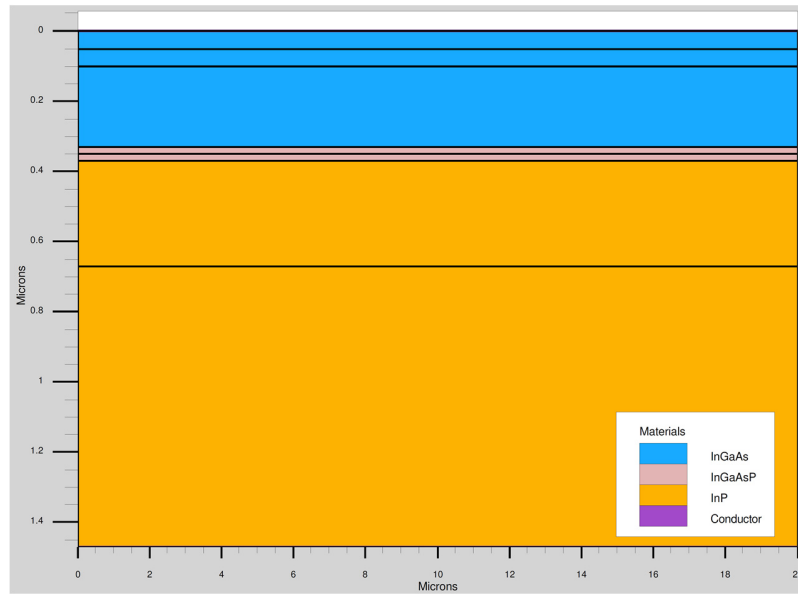*Figure A-2 Mesh grid of the OSJ-PD in Silvaco Atlas (Area is 20 μm²).*

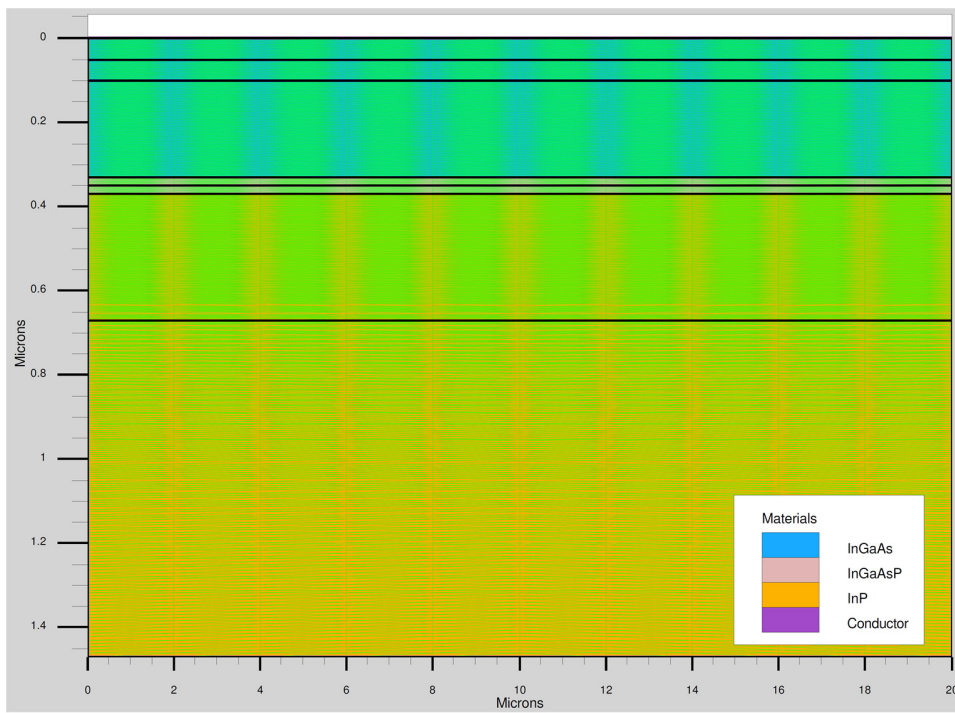*Figure A-3 Epitaxial layer structure of the MOSJ-PD in Silvaco Atlas (Area is 20 μm^2).*

Figure A-4 Mesh grid of the MOSJ-PD in Silvaco Atlas (Area is 20 μm^2).

Appendix B

Table B-1 Material parameters used in the TCAD simulation.

Parameter	InP	InGaAs
Electron mobility, μ_n	5400 cm^2/Vs	12000 cm^2/Vs
Hole mobility, μ_p	200 cm^2/Vs	300 cm^2/Vs
Valence band density of states, N_V	1.1×10^{19} cm^{-3}	7.7×10^{18} cm^{-3}
Conduction band density of states, N_C	5.7×10^{17} cm^{-3}	2.1×10^{17} cm^{-3}
Electron saturation velocity	2.6×10^7 cm/s	2.5×10^7 cm/s
Hole saturation velocity	5×10^6 cm/s	5×10^6 cm/s
Electron and hole life time (MOSJ-PD)	2×10^{-9} s	1×10^{-7} s
Electron and hole life time (MUTC-PD)	1×10^{-9} s	1×10^{-9} s
Electron Auger coefficient	3.7×10^{-31} cm^6/s	3.2×10^{-28} cm^6/s
Hole Auger coefficient	8.7×10^{-30} cm^6/s	3.2×10^{-28} cm^6/s
Real refractive index (1550 nm)	3.165	3.595
Imaginary refractive index (1550 nm)	0	0.075

Table B-2 Mobility model parameters used in the TCAD simulation.

| Mobility parameter	Parameter description	InP	InGaAs
MU1N.CAUGH	Minimum mobility at high doping	300 cm^2/Vs	3372 cm^2/Vs
MU2N.CAUGH	Maximum mobility at low doping	4917 cm^2/Vs	11599 cm^2/Vs
MU1P.CAUGH	Minimum mobility at high doping	20 cm^2/Vs	75 cm^2/Vs
MU2P.CAUGH	Maximum mobility at low doping	151 cm^2/Vs	331 cm^2/Vs
ALPHAN.CAUGH	Fitting parameter	0	0
ALPHAP.CAUGH	Fitting parameter	0	0
BETAN.CAUGH	Fitting parameter	-2.3	-2.3
BETAP.CAUGH	Fitting parameter	-2.2	-2.2
GAMMAN.CAUGH	Fitting parameter	-3.8	-3.8
GAMMAP.CAUGH	Fitting parameter	-3.7	-3.7
DELTAN.CAUGH	Fitting parameter	0.46	0.76
DELTAP.CAUGH	Fitting parameter	0.96	1.37
NCRITN.CAUGH	Critical doping above which mobility degrades	6.4×10^{17} cm^{-3}	8.9×10^{16} cm^{-3}
NCRITP.CAUGH	Critical doping above which mobility degrades	7.4×10^{17} cm^{-3}	1×10^{18} cm^{-3}

Appendix C
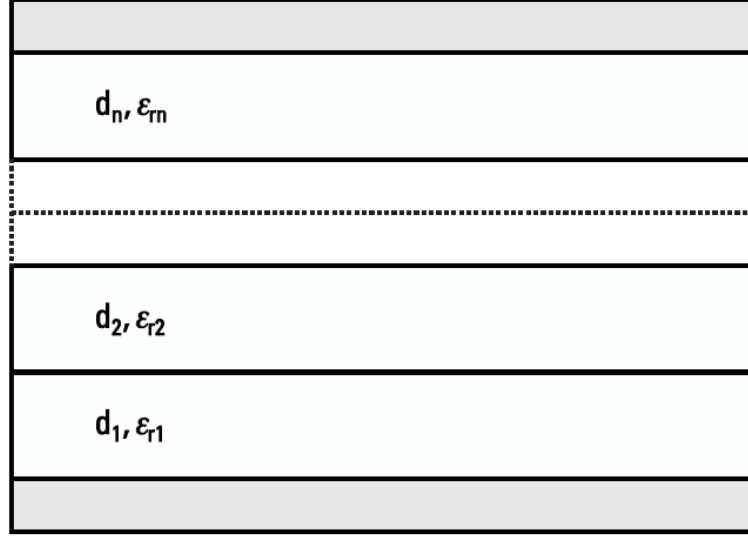
Figure C-1 Multilayer dielectric capacitor structure [125].

Since the photodiode has multiple dielectric layers, its junction capacitance should be calculated as a multilayer dielectric capacitor. As shown in Figure C-1, the multilayer dielectric capacitor consists of several dielectric layers with relative permittivity of ε_{r1}, ε_{r2}, … ε_{rn} and thickness of d_1, d_2, …, d_n. The equivalent relative permittivity ε_{req} is given by [125],

$$\varepsilon_{req} = \left[\sum_{m=1}^{n} \frac{d_m}{d_T \varepsilon_{rm}} \right]^{-1} \tag{C.1}$$

$$d_T = d_1 + d_2 + \cdots + d_n \tag{C.2}$$

where d_m is the thickness, and ε_{rm} is the relative permittivity of the m-th dielectric layer, and d_T is the total thickness. Similar to the parallel capacitor, the multilayer dielectric capacitance can be calculated by

$$C = \frac{\varepsilon_{req} \varepsilon_0 A}{d} \tag{C.3}$$

where ε_{req}, ε_0, A, and d are the equivalent relative permittivity, the permittivity of free space,

area of the capacitor, and thickness of the capacitor, respectively.
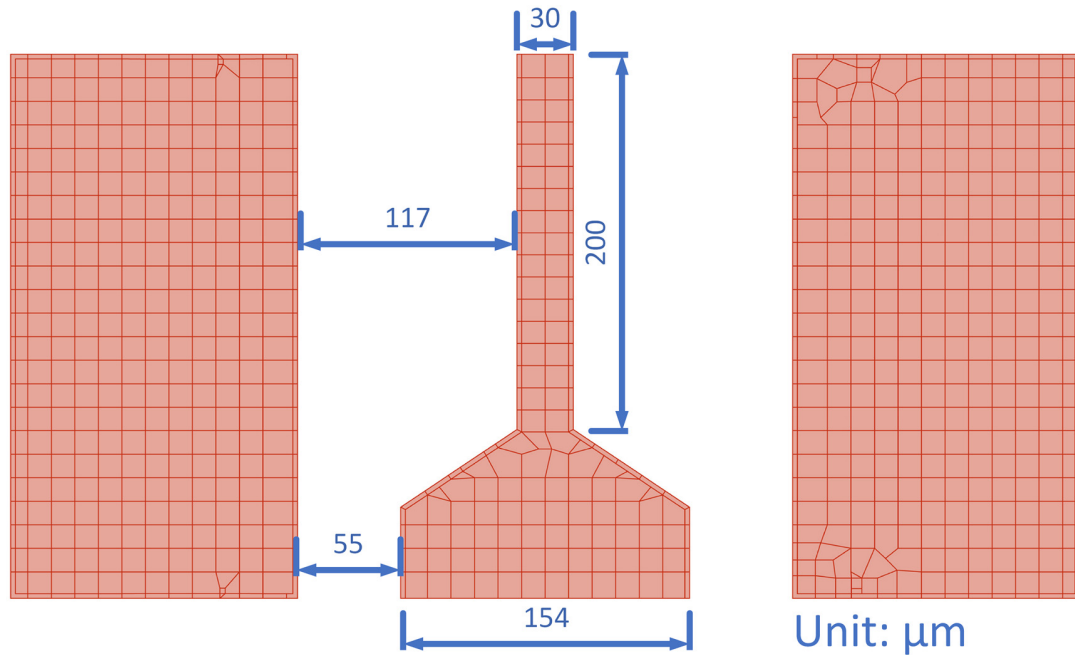
Appendix D

Figure D-1 Geometry of the CPW pad adopted in ADS EM/Circuit Co-simulation.

The geometry of the CPW pad adopted in ADS EM/Circuit Co-simulation is obtained from [78] and is given in Figure D-1. The substrate is AlN with a thickness of 400 μm. The dielectric constant of AlN is ε_r=8.7 and the dielectric loss tangent is *tan δ*=0.0005. The wider section has a characteristic impedance of 50 Ω and the narrower section has a characteristic impedance of 96 Ω. The narrower section transmission line with a length of 200 μm behaves like a quarter-wave impedance transformer, which improves the impedance matching between the load (50 Ω) and source (photodiode). Thus, the 3-dB bandwidth of the frequency response can be greatly enhanced.